

UNIVERSITE PARIS 7 - DENIS DIDEROT  
UFR DE PHYSIQUE

# THESE

présentée pour obtenir le grade de  
**Docteur en Sciences de l'Université Denis Diderot**

Precise measurement of the Absolute Yield of the Fluorescence of Nitrogen in  
the Air. Effects on the Detection of the Cosmic rays of Ultra-high Energy

Gwenaëlle Lefeuvre

Dirigée par Philippe Gorodetzky

Soutenue publiquement le 5 juillet 2006

## JURY

M. Thomas Patzak, Président  
M. Fernando Arqueros, Rapporteur  
M. Marcos Dracos, Rapporteur  
M. Philippe Gorodetzky, Directeur de thèse  
M. Pascal Lavoute, Invité  
M. Fabrice Piquemal, Invité

*(Long English version)*

This thesis has been translated by P. Gorodetzky using the automatic Google translator, which can be found at:

[http://translate.google.com/translate\\_t](http://translate.google.com/translate_t)

The figures and tables have not been translated (screen copies).  
Please be clement, or, send me an e-mail at

[philippe.gorodetzky@cern.ch](mailto:philippe.gorodetzky@cern.ch)



# Contents

<b>I Introduction</b>	7
<b>1 Detection of the Cosmic rays of Ultra-high Energy</b>	8
1.1 The spectrum of the cosmic rays	8
1.2 Development of an atmospheric shower	12
1.3 Methods of detection	15
1.4 The challenges of fluorescence	17
1.5 Conclusion	18
<b>2 Fluorescence of Nitrogen</b>	19
2.1 Theory of the emission of fluorescence	19
2.2 Objectives of fluorescence measurements	23
2.3 Conclusion	29
<b>3 Method Adopted in the Measurement of Fluorescence Yield</b>	30
3.1 Aim of the measurements	30
3.2 Geometry of the bench and detection of electrons	30
3.3 Detection of the photons	31
3.4 Calibration of the photomultipliers	31
3.5 Conclusion	32
<b>II Measurements</b>	33
<b>4 The bench</b>	34
4.1 Production of Fluorescence	34
4.1.1 The source	34
4.1.2 Detection and counting of the electrons	37
4.1.3 Definition of the volume of Fluorescence	38
4.2 Optical elements	40
4.2.1 Trajectories of the photons	40
4.2.2 Efficiency of the detection of the photons	45
4.3 Interactions of the electrons of the source	46
4.3.1 Emission of secondary electrons	46
4.3.2 Deviation of the primary electron	48
4.3.3 Diffusion in the lead shielding	49
4.3.4 Diffusion in the scintillator	51
4.3.5 Conclusion	51
4.4 Gas Control	52
4.5 Data acquisition	53

4.6 Adjustment of the PMT photons	54
<b>5 Calibration of Bench</b>	56
5.1 Probes of pressure and temperature	56
5.2 Centering of the lens	57
5.3 Grating spectrometer	58
<b>6 Measurement of Efficiencies of the Photomultipliers</b>	63
6.1 Principle of Measurement	63
6.1.1 The Photomultiplier	63
6.1.2 Use in the fluorescence bench	66
6.1.3 Conclusion	71
6.2 Cartographies of the Photocathodes of Photomultipliers	72
6.2.1 Description	72
6.2.2 Determination of the center of the photocathode.	75
6.2.3 Cartography with high gain	77
6.2.4 Conclusion	78
6.3 Absolute yield in a Point of the Photocathode	81
6.3.1 Operation of the integrating spheres	81
6.3.2 Efficiency with high gain	84
6.3.3 Conclusion: consequence for the measurement of fluorescence yield	93
<b>III Results</b>	94
<b>7 Results of Measurements of Fluorescence yield and Implications</b>	95
7.1 Measurements	95
7.2 Extraction of the signal	96
7.3 Yield integrated from 300 to 430 nm	97
7.3.1 Air Measurements at atmospheric pressure	97
7.3.2 Normalization of the results	99
7.3.3 Ratio of the yields in nitrogen and the air at atmospheric pressure	103
7.4 Results of spectral measurements	104
7.5 Conclusion	107
<b>8 Conclusion and Prospects</b>	109
<b>IV Appendices</b>	113
<b>A Data acquisition</b>	114
A.1 DAQ Electronics	114
A.2 LabVIEW Interface	117

<b>B The Single Mode Photoelectron</b>	123
B.1 Spectrum of single photoelectron	123
B.2 Adjustment of the PMT-photons	124
B.2.1 Adjustment of the luminous level	125
B.2.2 Adjustment of the threshold of the discriminator	126
<b>C Absolute calibration of the Bas PMT Gain</b>	127
C.1 Cartography	127
C.2 Absolute efficiency in a point of photocathode	128
C.3 Conclusion	138
<b>D Photographs of assemblies</b>	140

First part

Introduction

# Chapter 1

## Detection of the Cosmic rays of Ultra-high Energy

This chapter describes the context in which this study is placed. It shows the stakes that represent the control of Fluorescence in three points:

- the physics of the cosmic rays of ultra-high energy, because specificities of spectrum of the cosmic rays raise fundamental questions which do not have still found answer.
- questions caused by their detection: original particles interacting in the atmosphere produce atmospheric showers, is it possible to detect the particles who reach the ground and/or the most numerous particles?
- uncertainties which still weigh on the more reliable method of detection.

### 1.1 The spectrum of the cosmic rays

*Since one very moved back period of the history of the world, particles of an extraordinary energy, of a capacity of penetration exceeding what one could at one time imagine, fall on our ground. They arrive to us at like a hail, which would be continuous, of a constancy relentless, an imperturbable hail, which does not worry hour, neither of the season, neither of the position of the sun or the moon, nor even of that of Milky Way, a hail which wraps all, which crosses all, which crosses our body, since our birth, at the rate of a few million corpuscles per day, without making large damage in general, but causing, very seldom besides, of the atomic phenomena abrupt and complex. [Leprince-Ringuet45]*

The physics of the cosmic rays is a recent discipline, since its birth is generally accepted as being the measurement of flux of ionizing particles by Victor Hess, in 1912.

Among the abundant literature which exists on the cosmic rays ([Sokolsky04], [Gaisser90], [NaganoWatson00], [BoratavSigl04] ), Leprince-Ringuet, which was likely to assist with the stammering of this discipline, is one of those which speak about it with the most amazement, without still imagining the diversity and the originality of the spectrum in energy of these particles cosmic. This spectrum is the door of entry towards it field and towards the many questions and polemic which it causes since its stammering. It is represented on figure 1.1.

The primary cosmic rays are mainly nuclei. The spectrum is relatively well represented by a law of power:  $dN/dE = E^{-\alpha}$ , with  $\alpha=3$ , although light deviations with this law which one can observe on figure 1.1 have heavy consequences.

Results of the experiments balloons or satellites, able to measure directly the flux of particles until approximately  $10^{14}$  eV, indicate that the great majority of these cosmic rays are protons: 86%. The remainder is divided between the nuclei (11%, of helium to Fe), the electrons (2%), and photons. Results of the experiments balloons or satellites, able to measure directly the flux of particles until approximately  $10^{14}$  eV, indicate that the great majority of these cosmic rays are protons: 86%. The remainder is divided between the nuclei (11%, of helium to Fe), the electrons (2%), and photons. With lowest energies ( $E < 10$  GeV, or  $10^{10}$  eV), these particles come from the solar system. Their flux is strongly correlated with the rate of the eruptions and the solar cycle, and their composition is in agreement with the chemical composition of the solar system. Until approximately  $10^{17}$  eV, the cosmic rays are originating in the galaxy. They acquired their energy after being accelerated by shock waves produced by the explosions of supernovas.

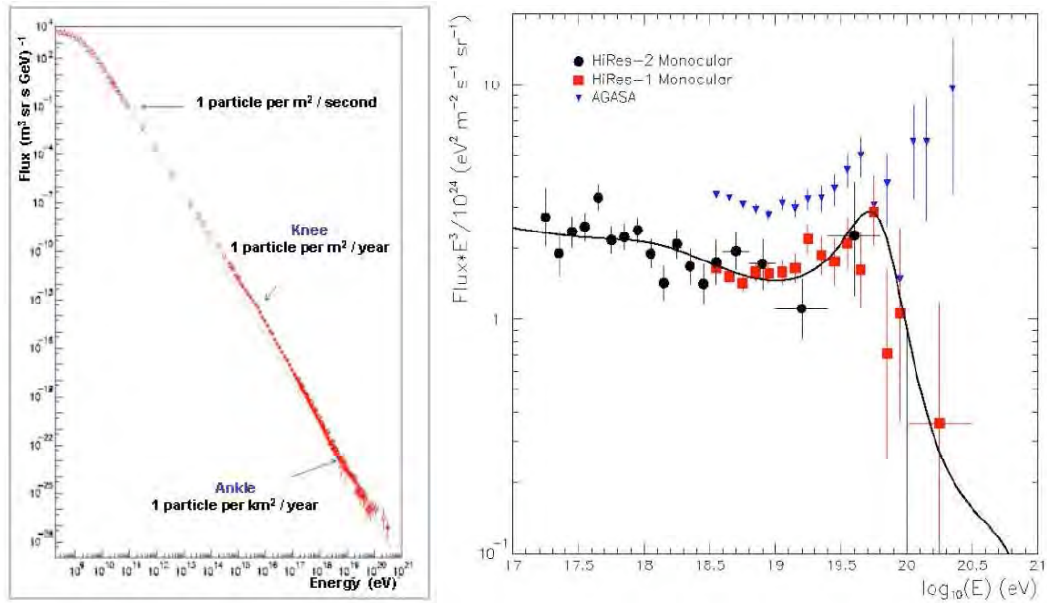
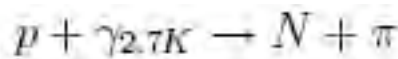


Fig.1.1 On the left, the spectrum of the cosmic rays in function of their kinetic energy. On the right, the part of ultra-high energies, multiplied by  $E^3$  to amplify variations spectrum. The full line corresponds to a calculation supposing a distribution of uniform sources.

The named transition “knee” (“Knee” on figure 1.1, at approximately  $10^{15}$  eV) marks a heaviness of the spectrum: the galactic magnetic field is too weak to contain the particles and they can escape, lightest before heaviest. One extragalactic component takes little by little the top, either towards  $10^{17}$  eV, or with “ankle”, with  $10^{18}$  eV. The transition towards extra particles galactic is not yet well understood.

The composition of the cosmic rays still remains mysterious because it becomes impossible to detect them directly. Until approximately  $10^{18}$  eV, mechanisms of acceleration of Fermi type are still efficient (explosions of supernovas, gamma ray bursts, jets of the radio-galaxy). On the other hand, it is still difficult to understand those which make possible to produce the ultra high energy cosmic rays (RCUHE), beyond  $10^{18}$  eV. *“Many surprises are still reserved to us, because they are very great energies that one explores, and new effects are discovered each time that one climbs a new level”*. [Leprince-Ringuet45]. This affirmation is always valid nowadays, because the answers generated new questions, towards higher energies. Among others, the polemic around the results with ultra-high energy ( $10^{20}$  eV): the theory of Greisen, Zatsepin and Kuzmin expects that the protons, that one supposed to compose the major part of the RCUHE, interact with the diffuse background cosmological ([Greisen64, ZatsepinKuzmin66]) and lose approximately 15% of their energy with each interaction via the reaction



If such is the case, then the RCUHE of more than  $10^{20}$  eV cannot come of more than of 50 Mpc. However, our close galactic vicinity does not contain any known astrophysical object sufficiently violent to produce particles at such energies.

Since the experiments of Leprince-Ringuet, many experiments measured the flux of cosmic rays precisely until the ankle (Volcano Ranch, Yakutsk, AGASA, HiRes ). From  $10^{20}$  eV, it does not arrive more than approximately 1 particle by  $\text{km}^2$  and per century. Obtaining statistics sufficient to be able to conclude the GZK cut existence needs an observation of long duration on areas several hundreds of  $\text{km}^2$ .

Two recent experiments wanted to give a final answer to this question, HiRes and AGASA. Their methods of detection, conceptually different, are detailed in the following part. Their conclusions, which are not in agreement, are represented on the graph of right-hand side of figure 1.1, and caused a polemic and an experimental challenge. It must be however noted that AGASA detects the electrons on top of the muons, which can cause an over-estimate of the energy of the primary particle. Bahcall and Waxman ([BahcallWaxman03]) also have assumed that a difference of calibration between both experiments could be at the origin of this apparent dissension.

Cosmic rays of energy higher than  $10^{20}$  eV were indeed detected, and the major stake is the measurement of their flux. If it is higher than what is predicted by the GZK model, it could announce the existence of new hyper-massive particles, called, for the lack of a better name, particles X. Their mass should thus be higher than  $10^{20}$  eV so that they emit RCUHE while disintegrating and their density and lifetime must correspond to the observed flux. Strong uncertainties exist nevertheless on these models Top-Down (in opposition to the models of acceleration known as Bottom-Up), because the flux of cosmic rays should mainly be composed of protons, photons and of neutrinos, and not of nuclei. Provided that one is able to distinguish the showers initiated by photons from those initiated by nuclei, this constraint is very strong.

The Pierre AUGER Observatory proposed a detector called hybrid, made up at the same time of detectors on the ground (like AGASA), of type water Cerenkov, and of telescopes for the fluorescence (like HiRes). This experiment, currently in course of construction and at the beginning of the data acquisition, has not made possible yet to close the discussion between HiRes and AGASA, since its uncertainty on the rebuilt energy of the RCUHE goes from 30% to 50% for energies from 3 to 100 EeV [Sommers04]. A general diagram of the hybrid detection of AUGER is presented on figure 1.2 (left).

Experiment EUSO, suggested in 2000, offers another experimental possibility. This time, it is a detector which would observe since space the shower tracks made by the RCUHE in the atmosphere (see the diagram of right-hand side of figure 1.2). The space detection presents in effect a double advantage: it makes it possible to cover a volume of atmosphere much more important than all experiments on the ground; the photons which reach the detector do not undergo as many diffusions as if the detector was installed on Earth since the atmosphere is less and less dense towards high altitudes. Detector EUSO (Extreme Universe Space Observatory) is a telescope equipped with PMMA Fresnel lenses, and whose focal surface is equipped with 36 pixels (5 mm) photomultiplier tubes working in single photoelectron mode. Acquisition is based on the counting of the photoelectrons, and the trigger is very much reduced to its simplest expression in order to save the power. A LIDAR is envisaged to detect the presence of clouds.

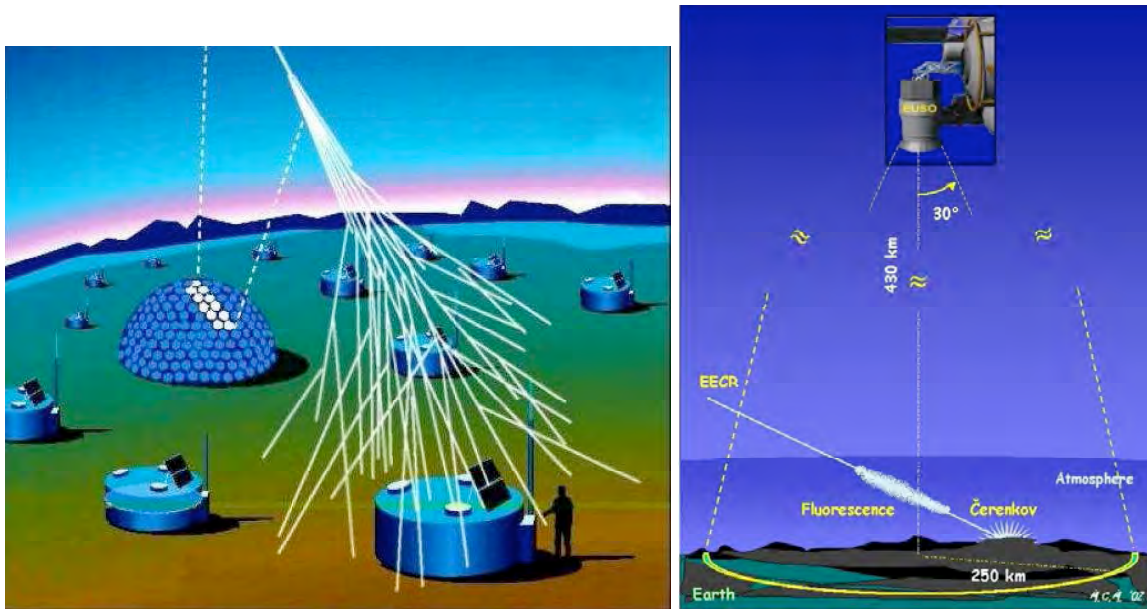


Fig.1.2 Presentation of the AUGER experiments (on the left) and EUSO (on the right), and of the way they detect the atmospheric showers. ([aug, eus])

Project EUSO is currently reorganized in Japan and in the United States under the name JEM-EUSO. Several technological modifications would allow to improve the performances of the future instrument, namely:

- use of CYTOP (plastic being used as cladding with plastic optical fibers, having a high index and a weak dispersion) in the place of the PMMA for the Fresnel lens, increasing the sensitivity of approximately 50 %;
- increase in a factor 2 of the surface of the pupil of entry;
- the use of DAQ electronics on board. Provided with its own trigger (search for patterns in the signals detected by the PMT), it can lower the threshold of detection to approximately  $10^{18.5}$  eV; the use of the Čerenkov effect rather than of a LIDAR (heavy and power consuming) to determine the possible presence and the altitude of the clouds. One recent study (Takahashi in [icr]) showed the possibility to rebuild correctly 95% of simulated showers, generated with and without clouds.

Contrary to AUGER, an experiment like EUSO uses only one method, that of fluorescence. But, as the following describes it, experimental uncertainties are fewer and more easily controllable. If the existence of cosmic rays of energy higher than the GZK cut is confirmed, the future of physics of the cosmic rays is without any doubt in space.

To deduce from the cosmic rays astrophysical informations and to hope to bring an answer to the questions raised previously, it is necessary to understand the data collected by the detectors. This only task is already very difficult: beyond approximately  $10^{14}$  eV, one cannot detect directly the cosmic rays, but only products of their chain reactions with the nuclei of the atmosphere: the atmospheric shower. The challenge for the experimenters, and the methods of detection to be used are better understood after having studied the development of a shower in atmosphere.

## 1.2 Development of an atmospheric shower

The RCUHE which penetrate in the atmosphere undergo collisions with its nuclei, initiating the atmospheric showers. As the density of the air is very weak in the highest layers of the atmosphere (around 40 km of altitude), the altitude of the first interaction is prone to very strong variations of a shower to another. For this reason, we speak only of average behavior.

### Anatomy of a shower

One distinguishes usually three components in one shower: hadronic, muonic and electromagnetic [Gaisser90]. Figure 1.3 gives a schematic idea. *The hadronic component* makes the core of a shower initiated by a proton or a nucleus. The hadron interactions produce mainly pions and kaons.

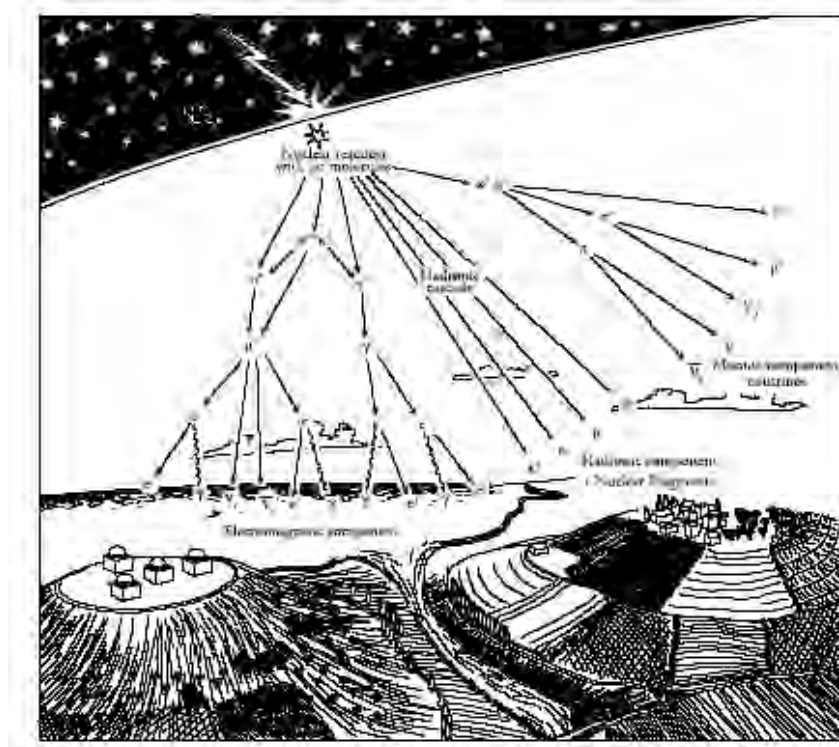
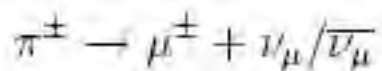


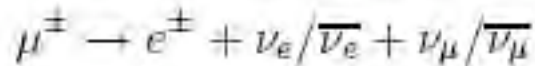
Fig. 1.3 Schematic representation of the development of an atmospheric shower. The lifetime of the charged kaons and pions, respectively 12 ns and 26 ns and a weak interaction length (approximately  $100 \text{ g.cm}^{-2}$ , [Gaisser90]) allows them to interact again. When the charged pions do not have enough energy for new reactions, they disintegrate and feed the muon part of the shower via the reactions



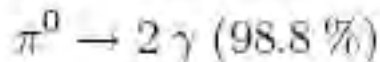
Although the protons are dominating, a shower can also be initiated by a nucleus of  $A$  nucleons. In this case, a simple but efficient model considers the cascade like the superposition of  $A$  non-identical cascades initiated by a single nucleon of energy  $E_{\text{shower}}/A$ .

To determine if a nucleus or a proton were detected once it interacted is difficult. If the number of emitted particles is crucial in this detection, the energy of each nucleon of the nucleus ( $E_{shower}/A$ ) is fundamental to interpret physically the results.

*The muonic component* interacts very little with the atmosphere. The number of muons grows with the pions and kaons disintegrations until reaching it flattens out. Muons lose mainly their energy by ionization, but, unless their initial energy is lower than a few GeV, their lifetime allows a large majority of them to reach the ground ( $\tau = 2.2 \mu s$ ). They almost do not radiate: the bremsstrahlung cross section varies like the inverse of the square of mass particle. As the muon is 200 times heavier than the electron, it radiates 40000 times less. The muons which disintegrate feed the electromagnetic component of the shower via



*The electromagnetic component* is thus that which quickly counts the most particles : electrons, positrons and photons. In the case of a hadron shower, it is initiated by the quasi-immediate disintegration of the neutral pions ( $\tau = 8.4 \times 10^{-17} s$ ):



Each gamma whose energy exceeds 1.022 MeV, a pair  $e^+/e^-$  is produced, which radiates new photons by bremsstrahlung. The average energy of the electrons being 80 MeV, that of gamma will be approximately 40 MeV. In theory, the distinction between the showers initiated by high-energy particles and those initiated by photons is simple, since in the second case, the shower is thus almost purely electromagnetic. However, if the photon interacts first of all with a nucleus (photoproduction of pions), the shower created will be hadronic. This phenomenon is not very probable: approximately 1 photon out of 3000. Others effects come to disturb the development of an electromagnetic shower with ultra-high energy (LPM effect, interaction with the terrestrial magnetic field).

As long as the available energy is sufficient, the creation of particles continues and shower size increases. It can reach up to  $10^{10}$  particles to the maximum for a RCUHE of  $10^{19}$  eV. But for each process implied (collisions, disintegrations, radiation), there exists an energy threshold below which production of particles becomes impossible. The size of the shower decreases then as its components are attenuated in the atmosphere, or disintegrate. Thus, the hadrons never reach ground. The electrons lose their energy by radiation until they have reached the critical energy of 80 MeV. Lower, the losses by ionization are higher than losses by radiation: they are quickly stopped and absorbed. There are almost no more electrons nor positrons at the sea level, and even more none if the energy of the primary particle is lower than  $10^{18}$  eV. More than 90% of the energy deposited in the atmosphere has been by the electrons and positrons.

Finally, shower to shower fluctuations can, among other things, be explained by the relative abundance of neutral pions. Some hadron reactions do not generate any  $\pi^0$ , whereas others produce them in great number [Gorodetzky04]. The study of phenomena of extreme energy, whose statistics are weak, can place us in the pions distribution tail. These fluctuations could be sufficient to be interpreted like over-estimated energies.

## Light emission

Two luminous phenomena are induced in the atmosphere by the passage of charged particles. The first is the Čerenkov radiation, which is a luminous shock wave due to the relativistic nature of the shower particles (see diagram 1.4). The Čerenkov photons form a cone around the axis of the atmospheric shower. The angle  $\theta$  of this cone is given by:

$$\cos(\theta) = \frac{1}{n(\lambda)\beta}, \quad \beta = v/c$$

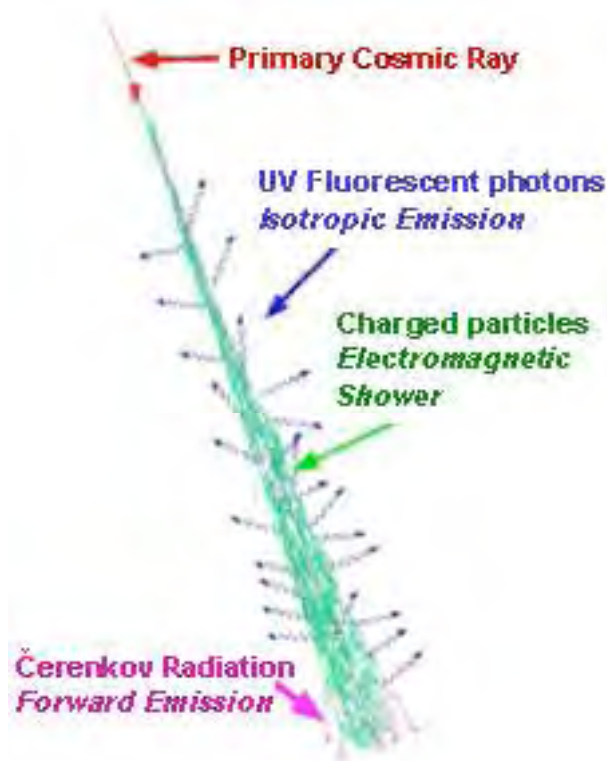


Fig. 1.4. Diagrammatic representation of the light yields caused by an atmospheric shower [eus] .

where  $n(\lambda)$  is the index of refraction of the air for a wavelength  $\lambda$ ,  $v$  is speed of light in the medium of index  $n$  and  $c$  is the speed of the light in vacuum.  $n$  increase slightly as the shower develops in the atmosphere, consequently,  $\theta$  also increases: the Čerenkov cone created by a particle with  $\beta = 1$  widens from  $1.06^\circ$  at 5 km of altitude to  $1.36^\circ$  at sea level. The proportion of Čerenkov photons which reach the detector (by reflection on the ground or the clouds) compared to the number of Čerenkov photons, emitted directly or after diffusion on the molecules present in the atmosphere, varies strongly with the geometry of the shower, and can exceed 50% if the detector is near the axis of the shower [Nerling05].

The second phenomenon relates to the charged particles (mainly electrons), relativists or not, who excite the molecules of the atmosphere. Among those,  $N_2$  de-excites itself by emitting isotropically photons in the close ultraviolet: the light of fluorescence. The phenomenon of fluorescence is the object of this work: it is explained in detail in the following chapter.

Two possibilities are thus offered to the experimenters to study the showers initiated by the RCUHE:

- to detect the muons which reach the ground. For that, one measures the signal in a scintillator or a Cerenkov detector;
- to detect the photons of fluorescence emitted on the passage of the atmospheric cascade. One uses for that fluorescence telescopes whose pixels, generally photomultiplier tubes, are sensitive to emitted UV photons.

The following part examines the instrumental solutions reserves for the study of the RCUHE.

## 1.3 Methods of detection

Two techniques currently coexist. One consists in sampling the shower at a given time of its development, when it reaches the ground. The other observes its integrity all along its visible course. These two techniques are not at all equivalent and do not present the same difficulties of reconstruction. This part attempts to show why, although the sampling is a promising method, the “calorimetric” or rather global measurement, is, for the time being, more reliable.

### **Sampling of the shower**

Sampling is mainly for the muons. The shower front, when it arrives at the ground, can extend on several square kilometers. Rather than a single detector, gratings of small detectors have been built (experiments Volcano Ranch, Haverah Park, Yakutsk, AGASA, AUGER). Those can be muon detectors (Volcano Ranch, Yakutsk), scintillator plates coupled to photomultipliers (AGASA) or water Cerenkov detectors (AUGER). Scintillators are sensitive to muons and electrons. Electrons will be detected because these experiments are generally installed at high altitude, where the electrons are still numerous. On the other hand, water Cerenkov detectors will detect especially the muons.

The muons which cross these detectors deposit there some energy, yielding thus one contour of the shower at one and one only moment of its development,. For this reason, they are generally installed at high altitude, so that they detect the shower shortly after its maximum, where one obtains more informations: the altitude of the shower maximum and its lateral extension are connected to the energy and the nature of the primary particle.

To deduce energy from the cosmic ray from the signals deposited in each detector, first of all the position of the shower foot has to be found, i.e. the intersection of the shower axis with the ground. For that, a function describing the lateral distribution of the particles has to be extrapolated, parameterized by the effectively measured signals, towards the center of the shower (see for example the equation (8) of [NaganoWatson00]).

Then, one interpolates the density of particles to a distance to the foot of shower to deduce the total energy. This distance, fixed once and for all and related to the geometry of the grating, is determined by simulations. Its value is for example 1000 m for the experiment AUGER [Watson05]. It corresponds to distance for which the lateral distribution function presents the less fluctuations. A correction is necessary to take into account the slope of the shower. Both the determination of the center and the extrapolation of the signal introduce systematic uncertainties which can reach 20% each ([Yoshida04, Sommers04]).

The energy of the primary particle is deduced by applying a relation from conversion between the density at 1000 m and energy. This relation depends strongly on the models of hadronic interactions, on the of the primary particle mass, and of the grating itself. Indeed, the knowledge of the hadron reactions cross sections is essential. However, data on the cross sections currently available come from reactions studied in the accelerators. The range of covered energy is completely different, since the accelerators do not exceed yet 2 TeV in centre of mass. The collision of a proton of  $10^{20}$  eV on a nucleon at rest in a nucleus of the atmosphere corresponds to  $\sqrt{s} = 450$  TeV. Extrapolations are thus necessary but also, to a certain extent, necessarily hazardous. The systematic error at the energy reconstruction in the AUGER experiment, for example, increases still today from 30% to  $3 \cdot 10^{18}$  eV to 50% at  $10^{20}$  eV [Sommers04].

### **“Calorimetric” measurement**

The detection of fluorescence emitted by the shower is on the contrary a measurement “calorimetric” of the longitudinal development. In principle, this method is more direct to reach the energy of the primary particle and its nature. Indeed, the production of fluorescence is proportional to the energy loss of the electrons and thus to their number (see the following chapter). The calorimeter, the atmosphere, is extremely efficient because without sampling: the detector sees the image of the shower all along its development like a full disc going towards the ground at the speed of the light. The diameter of this disc increases with time. The observation of fluorescence is a direct measurement of the local energy deposit, and thus of the size of the shower.

Approximately 0.5% of the energy carried by the charged particles is converted into fluorescence. A fraction of these photons can reach fluorescence telescopes located at a few kilometers of the shower (experiment Fly' s Eyes, today HiRes, and AUGER). They detect the photons whose wavelength lies between 300 and 400 Nm, because it is in this range that fluorescence is emitted. Each pixel of the focal plane of these telescopes observes a fixed portion of the atmosphere. The shower is seen like a trace moving in straight line with speed  $c$ . The number of deposited photons varies with the number of produced photons and shows this way “the history” of the shower in the atmosphere. The energy threshold of this method is, for AUGER,  $10^{17}$  eV, and for EUSO, of  $5 \cdot 10^{18}$  eV (according to the of data acquisition system selected [Crawford]).

The electromagnetic component of a shower is at the origin of the production of fluorescence photons, since it is especially the electrons which interact with nitrogen molecules. The role of the models of hadronic interactions is limited to the determination of the energy known as missing energy: the fraction of the total energy transferred to the neutrinos and the muons rather than to the electromagnetic cascades. Simulations evaluate this fraction to 7.5%, with an error of approximately 2.5%. These numbers take into

account the variation due to the difference between the showers initiated by a proton or an iron nucleus ([Sommers04]). In other words, if the detection by fluorescence was infinitely precise (and if the ratio between charged and neutral pions is kept constant, for example 2), the uncertainty on the shower energy would be 2.5%. However, one is still far from this result, since the quoted error goes from 30 to 50%. This work precisely carries on an attempt at improvement of this precision.

## 1.4 The challenges of fluorescence

Detection on the ground imposes to have hadronic models to be able, knowing the number and the energy of the detected particles, to estimate the energy of the primary cosmic ray. But the hadron cross sections are extrapolated because they are not yet accessible to accelerator measurements.

The detection of fluorescence is not subjected to this problem. Among the emitted photons, the detected fraction depends on observables which all are measurable. Contrary to lateral distribution function, the signal of received fluorescence at a given moment is simple and is not parameterized. Its expression allows to list the causes of uncertainties [NaganoWatson00]:

$$N_{pe} = N_e(E) Y(E) A Q \frac{\Delta L}{4\pi r^2} e^{-r/r_{ext}}$$

where

- $N_{pe}$  is the number of photoelectrons counted by the photodetector;
- $N_e(E)$  is the number of charged particles (especially the electrons) for a given electron energy  $E$ , integrated in approximately 1  $\mu$ s (approximately  $10^7$ );
- $Y(E)$  is the fluorescence yield (per electron and per meter) for a given one electron energy  $E$  (approximately 4);
- $A$  is the surface of collection of the mirror of the telescope (a few  $m^2$ );
- $Q$  is the efficiency of the implied photomultiplier (about 20%);
- $\Delta L$  is the portion of the trace of the shower seen by the pixel defined by the photomultiplier (about 1%);
- $r$  is the distance from the detector to the fluorescence emission place (some tens of kilometers for a detector on the ground);
- $r_{ext}$  is the light extinction length. It is caused by the diffusions and absorptions in the atmosphere (approximately 20 km on the level sea).

The principal causes of error thus lie in the estimates of  $N_e$ ,  $Y$ ,  $Q$ , and  $r_{ext}$ . That of  $N_e$  does not depend on the fraction of not detected energy (for example carried by neutrinos). The length of extinction  $r_{ext}$  is the object of many campaigns of measurements [Keilhauer04]. It is one of the more difficult quantities to be specified in reason of the variations in the short and long term of the atmosphere (temperature, moisture, composition chemical ). The results are delicate to exploit, and are not yet well integrated with the analysis of the showers, but progress [Keilhauer+05] is fast.

## 1.5 Conclusion

The measurement of the fluorescence of nitrogen excited by the particles of an atmospheric shower is finally the most direct method and more reliable currently to estimate the energy of the primary cosmic rays.

Only the duty cycle is a good argument in favor of the detection of the shower front on the ground: the gratings of detectors can work 24h a day, while the fluorescence telescopes are limited to the nights without clouds and the moon (10% from the ground when one looks at the sky, source of background. A detector like EUSO, turned towards ground, could have a useful cycle of 25%).

At present, reconstructions made by one and other method do not lead to the same energy. The sampling of the shower systematically yields an energy higher from 30 to 50% from that which results from the analysis of fluorescence. The AUGER experiment thus did not succeed yet to really explain the dissensions between AGASA and HiRes, and for the moment calibrates the results of the surface detector with those of the fluorescence telescopes [Sommers04]. A better control of the factors who condition the detection of fluorescence is thus paramount.

Uncertainties on the four quantities  $N_e$ ,  $Y$ ,  $Q$ , and  $r_{ext}$ , it was seen, are far from being negligible. They are currently the object of campaigns of intensive measurements. This work fits in this effort. Measurements made at the laboratory allowed to quantify in an absolute and precise way the yield of Fluorescence, but also the photomultiplier tubes efficiencies. In effect, the photodetectors efficiencies are seldom known to better than 15 to 20%. It is thus not possible to consider a measurement of fluorescence yield without one specifying the efficiencies of the used photomultipliers.

The following chapter enters in the detail of molecular de-excitations at the origin of fluorescence. It exposes the characteristics of the nitrogen spectrum, and the variations of the fluorescence yield with the environmental conditions (pressure, temperature, ).

# Chapter 2

## Fluorescence of Nitrogen

The phenomenon of fluorescence is well-known: the molecular nitrogen is studied since the Fifties because of its scintillation (and its application to the lasers), that same one who interests the cosmic rays experiments. This chapter presents the mechanisms working in the production of fluorescence. It does not have for objective to enter in the details of molecular physics. The goal assigned with this study of fluorescence is to decrease the uncertainty on the determination of the energy of the primary cosmic rays.

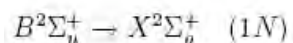
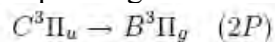
### 2.1 Theory of the emission of fluorescence

#### The Spectrum

The emission of the fluorescence photons results from the de-excitation of the molecular nitrogen of the atmosphere. A diagram of levels is shown on figure 2.1.

The large horizontal lines represent the electronic states and the small ones, their degeneracy in vibrational levels. The molecular structure of nitrogen is well-known [Millet70]. The two systems of bands concerned with fluorescence are the system 2P of the molecule  $N_2$  and 1N of the ion  $N_2^+$ . (This nomenclature comes from the discharges in tubes experiments of Crookes [Herzberg50]).

The corresponding electronic transitions are:



These notations follow the rules dictated by molecular physics. They include:

- the state of the level (ground: X or excited: A, B, C) ;
- the resulting spin S (number 2 or 3 in exponent, whose value is  $2S + 1$ );
- resulting angular momentum ( $\Sigma$  for 0,  $\Pi$  for 1);
- the symmetry of molecular orbital (sign +);
- the parity of molecular orbital (indexes u and g).

The spectrum of fluorescence is thus a spectrum of lines. It is represented on figure 2.2. This spectrum was obtained with an electron gun as a source. The average energy of the electrons is 15 keV: it is so low that diffusion is very important. The average length traveled by the electrons is thus impossible to determine, and one cannot measure the fluorescence yield. On the other hand, the very high number of electrons makes that the number of produced photons is important. It is thus possible to use a grating spectrometer whose slits are very narrow (the resolution of this spectrum is of 0.03 nm). This assembly is thus ideal to compare intensities of the lines between themselves.

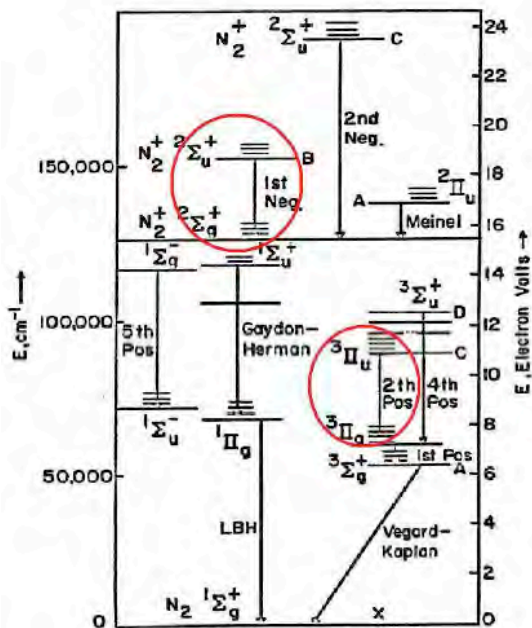


Fig.2.1 Diagram of the energy levels of molecular nitrogen. Sets of transition surrounded by red circles correspond to the de-excitations producing fluorescence, they are the 1N and 2P systems. The levels X, A, B are the electronic states, X being ground. The small levels added to the electronic states are degeneracy vibrational levels. [Bunner64]

### Mechanisms of excitation

With the passage of the shower, the nitrogen can be excited directly or indirectly [Bunner67]:

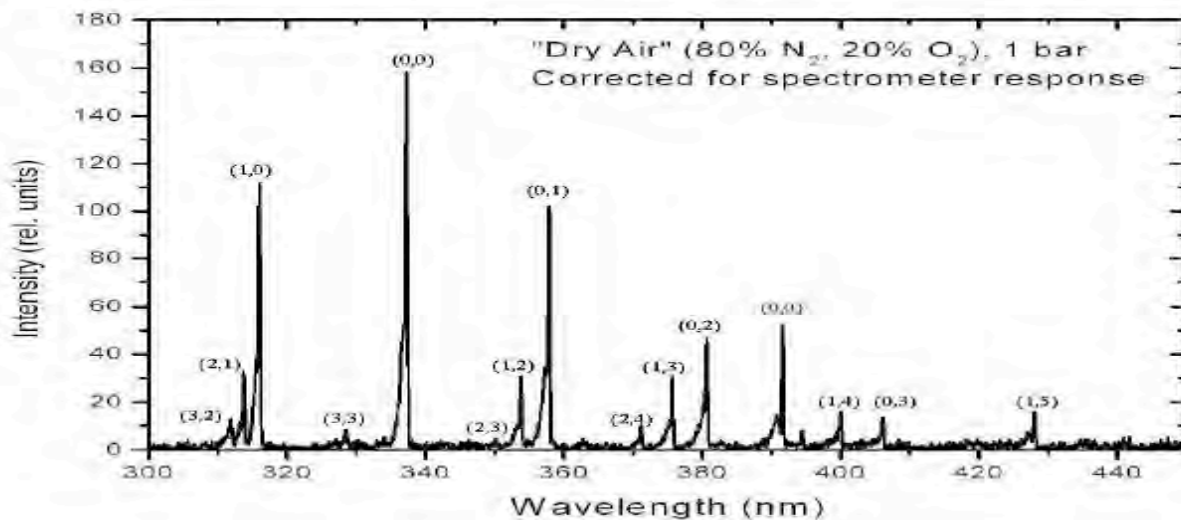
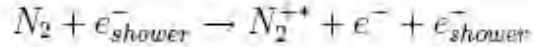
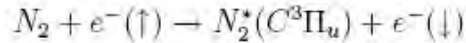


Fig.2.2 Emission spectrum of fluorescence. The pairs of numbers indicate transitions between vibrational levels, the first number being the excited level. The line (0,0) at 391.4 nm belongs to the system 1N of the ion  $N_2^+$ . (ref: Ulrich in [air])

- *the direct excitation.* A fraction of the energy deposited locally by the shower can excite or ionize nitrogen, with a probability depending on the energy of the electron and on the excited level,  $\nu$ ,  $\sigma_\nu(E)$ . Less than 16 eV are enough to ionize the molecule of nitrogen (see figure 2.1). The particles of a shower reach several MeV, this mode of excitation relates especially to the system 1N (ionized nitrogen):

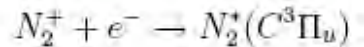


- *The indirect excitation.* Electrons of low energy (in particular  $\delta$  rays) ejected from ionized molecules, excite the nitrogen 2P system, with a change of total spin:



In addition, the electrons of the shower have about the same probability of interaction with any atomic electron. Some ionizations lead to the ejection of electrons of the layer K and the molecule, by reorganizing its electronic procession, emits an electron of an upper layer: an Auger electron. This one can in turn excite nitrogen.

On the other hand, the level  $C^3\Pi_u$  is modified very little by the recombination of ionized nitrogen with an electron ([Bunner64]):



### De-excitation modes

They are theoretically, of three kinds:

- *radiative de-excitation*, i.e. the emission of fluorescence;
- *collisional de-excitation*;
- *internal recombination*: reorganization of the electronic orbits without photon emission. There is no experimental evidence this kind of de-excitation takes place in the nitrogen molecule (Arqueros in [iwf]).

The atmosphere is not made up exclusively of nitrogen, but also of oxygen (approximately 21%), of argon (approximately 1%), and traces of water vapor of other rare gases. Argon excited by an electron transfers its energy to nitrogen, same way as in a gas scintillator. But the presence of others impurities limits the increase in fluorescence by argon to less than 1% [Bunner67].

Oxygen, very electronegative, efficiently attracts the free electrons  $10^4$  times that the nitrogen does [Bunner67]. In addition, the collisions of oxygen with ionized nitrogen cause a transfer of the positive charge on oxygen, which prevent the recombination of nitrogen with an electron. Thus, it decreases the rate of production of fluorescence. One speaks about the “quenching” of fluorescence by oxygen. This suppression is *not* proportional to the ratio of concentrations  $N_2/O_2$ . If it were the case, in air, only 4/5 of fluorescence would be measured compared to pure nitrogen.

Although all experiments having compared the yields in nitrogen and air find suppression factor of higher than 4/5, there is not yet a definitive agreement on this question. [DavidsonO'Neil64] indicates a ratio of almost 25 at a pressure of 600 mmHg, while [Kakimoto+96] and [Nagano+04] give approximately 5.5. At higher energy, the FLASH ([Belz+06]) experiment gives 6.6. We will see in chapter 7 that our measurements give a report/ratio from almost 5 at the atmospheric pressure.

Each one of these processes has a specific duration, the lifetime. They are the starting point of the use of the kinetic theory of gases, which makes possible to clarify the dependences in pressure, temperature,  $\nu$ , of the fluorescence production, and of to understand the measurements made by the community.

### Parameterization of the efficiency of Fluorescence

The efficiency of fluorescence of a line, i.e. of frequency  $\nu$ , is the probability that the nitrogen is de-excited by fluorescence in this frequency. Bunner has proposed a parameterization, which uses the kinetic theory and which is still in use [Bunner67]. It first of all expresses the total rate of de-excitations:

$$\frac{dn}{dt} = n \left( \frac{1}{\tau_{rad}} + \frac{1}{\tau_{int}} + \frac{1}{\tau_{coll}} \right)$$

where:

- $n$  is the number of excited molecules at a level  $\nu$ ,
- $\tau_{rad}$  the lifetime of this level for radiative de-excitation,
- $\tau_{int}$  that of internal de-excitation,
- and  $\tau_{coll}$  that of de-excitation by collision.

By posing  $\frac{1}{\tau_0} = \frac{1}{\tau_{rad}} + \frac{1}{\tau_{int}}$ , sum of the internal processes, one writes the fluorescence efficiency  $\Phi$  as the proportion of de-excitations by radiation:

$$\Phi = \frac{\frac{1}{\tau_{rad}}}{\frac{1}{\tau_{rad}} + \frac{1}{\tau_{int}} + \frac{1}{\tau_{coll}}}$$

that is to

$$\Phi = \frac{\tau_0}{1 + \frac{\tau_0}{\tau_{coll}}}$$

The numerator corresponds to the fluorescence efficiency in the absence of collisions. In other words, it informs about the competition between the processes of de-excitation interns with the molecule. In the denominator, the ratio  $\tau_0/\tau_{coll}$  evaluates the suppression of fluorescence by the collisions, i.e. the “quenching” due to the pressure (proximity effect). The average duration between two collisions depends on the pressure and temperature of the gas. The kinetic theory of gases makes it possible to write:

$$\tau_{coll} = \frac{\sqrt{\pi M k T}}{4 p \sigma_{NN}}$$

with:

- $M$ , the molecular mass of nitrogen,
- $k$ , the Boltzmann constant,
- $T$ , gas temperature,
- $p$ , gas pressure,
- $\sigma_{NN}$ , the cross section of collisions between two nitrogen molecules in one given state.

The internal processes represented by  $\tau_0$  take place at zero pressure. One can nevertheless define a equilibrium pressure  $p_0$  for which there are as many internal de-excitations that collisional:

$$\tau_{coll}(p_0) = \tau_0$$

that is to say

$$p_0 = \frac{\sqrt{\pi M k T}}{4 \tau_0 \sigma_{NN}}$$

The fluorescence efficiency is thus rewritten:

$$\psi = \frac{\tau_0}{\tau_{rad} \left( 1 + \frac{p}{p_0} \right)}$$

This expression brings two remarks: 25

- The expressions of  $\tau_{coll}$  and  $p_0$  are given in the simple case where the gas is pure nitrogen. In the air, other collision cross sections of intervene (presence of oxygen, water ). They are included in the preceding formulas with a weight corresponding to the volume fraction of the second molecule [Keilhauer+05].
- Each molecular level its own lifetime. Consequently, the fluorescence efficiency  $\Phi(p)$  is in fact  $\Phi_{\nu}(p)$ . There is thus as many equilibrium pressures  $p_0$  than lines in the spectrum. The experimental application of this parameterization thus requires that the efficiency is measured line by line, if one wants to determine it in function of pressure and temperature.

Several experiments measured the efficiencies of the nitrogen lines ([DavidsonO' Neil64], [Bunner67], [Kakimoto+96]). Dissensions persist between the results. They are perhaps due to the differences between the experimental conditions: pressure, nature and energy of the exciting particle. [Nagano+03] and Waldenmaier in [iwf] continue currently in this direction with a strontium source and of optical filters to separate the lines.

Finally, it is important to recall that if the individual study of the lines is necessary to improve the comprehension of the mechanisms of the emission of fluorescence, the physics of the cosmic rays needs measurements integrated from 300 to 430 nm.

## 2.2 Objectives of fluorescence measurements

The current studies aim at quantify the variables related to the production of fluorescence. The important quantity for the cosmic rays physics is not as much the fluorescence

efficiency  $\Phi$  as it is the number of photons created per unit of length traveled by an electron.

### Relation with the energy loss of the shower

The energy deposited by an electron and by unit of length in a given medium is

$$\rho \frac{dE}{dX}$$

The number of photons of frequency  $\nu$  which one can produce with this energy is, taking into account the efficiency of the line considered:

$$Y_\nu (\text{photons}/e/cm) = \phi_\nu \frac{\rho}{h\nu} \frac{dE}{dx}$$

The fluorescence production rate in the whole spectral range (300 to 430 nm) is thus:

$$Y = \sum_\nu Y_\nu$$

Measurements of the relation between  $Y$  and  $dE/dx$  are made at low energy with a radioactive source, and at high energy in accelerators ([Belz+06], [Arciprete+05]). Up to now, all the experimental results have confirmed the proportionality between the energy of the charged particles and the production rate of fluorescence. The graph of figure 2.3 shows the results of the experiment AIRFLY in nitrogen. This experiment use the same broad filter (M-UG6 of Schott) than the Auger experiment to select the spectrum of fluorescence.

The graph of figure 2.4 shows the results obtained in the air with different energies. The deposited quantity of energy is smaller than the energy lost by the electrons because part of it is emitted as radiation and not used for the excitation of the medium. The systematic uncertainties on this graph are still important:

- 13% for the result of [Nagano+04],
- 10% for those of [Kakimoto+96] (this value is under estimated, the following publication by the same authors giving 14% [Nagano+03])
- 16.6% for those of [Belz+06],
- This graph requires two details to be explained:
- The results, which come from three experiments, all are not normalized to the same conditions of temperature and pressure. The value of [Nagano+04] is given for 1000 hPa and 20°C; that of [Kakimoto+96], for 1013 hPa (1 atm) without mention of

temperature; and those of [Belz+06], for 1013 hPa and 29°C. But, a variation of approximately 5°C induces a variation of 1% on the fluorescence yield. It is thus important to take into account the normalizations of each one when comparing the results.

- The systematic errors result in the three cases of the bad knowledge of the photodetectors. They are estimated at 10% in [Nagano+04] and at 10.5% in [Belz+06] and [Kakimoto+96]. One thus understands that a measurement of fluorescence yield cannot be substantially improved without diminishing the systematics due to the photodetectors. For this reason we have given a great importance to measure the absolute efficiency of our two detectors of photons of fluorescence.

### Dependence as a function of the pressure and of the temperature

The electrons of the shower move in an environment which varies a lot as altitude decrease (see the curves of the variations of pressure, temperature and density as a function of altitude on figure 2.5). [Nagano+03] describes the variation of the production rate of fluorescence  $Y$  with altitude in the following way:

$$Y_\nu(z) = \frac{A_\nu \rho(z)}{1 + B_\nu \rho(z) \sqrt{T(z)}}$$

with

$$A_\nu = \frac{(dE/dX) (\tau_0 / \tau_{rad})}{h\nu}$$

and

$$B_\nu = \frac{4\sigma_{NN}\tau_0 R_{N_2}}{\sqrt{\pi M k}}$$

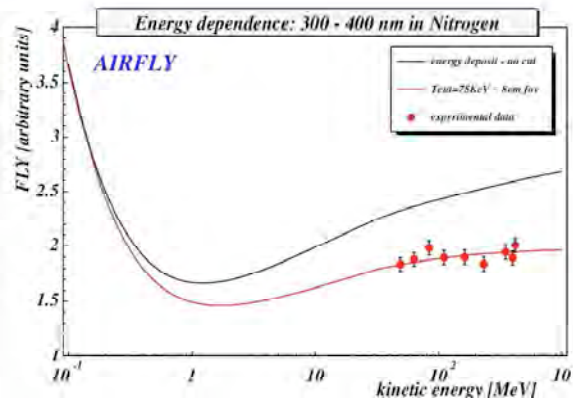


FIG.2.3 Variation of the fluorescence yield in nitrogen at high energy in the AIRFLY experiment.

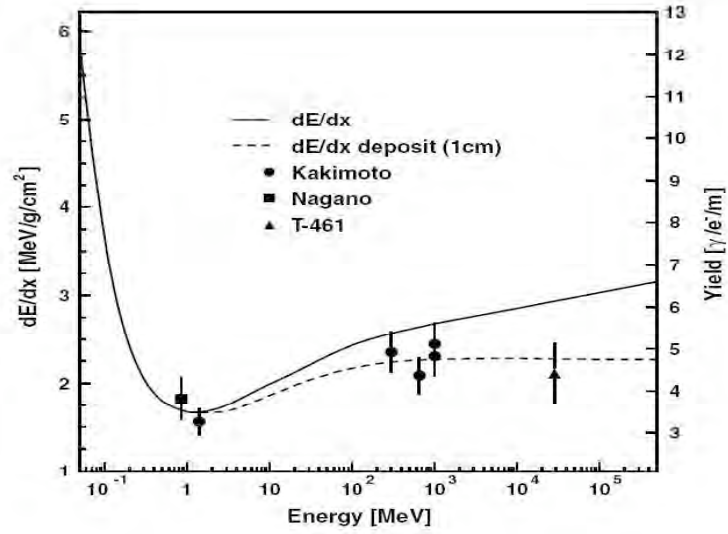


FIG.2.4 Results of measurements of the fluorescence yield in air versus the electron energy deposit, between 300 and 400 nm [Belz+06].

$\lambda$ (nm)	$A_\nu$ $\text{m}^2.\text{kg}^{-1}$	$B_\nu$ $\text{m}^3.\text{kg}^{-1}.\text{K}^{-1/2}$	$Y_\nu$ photons/m
316	$20.5 \pm 1.3$	$2.14 \pm 0.18$	$0.549 \pm 0.057$
329	$3.91 \pm 0.35$	$1.22 \pm 0.14$	$0.180 \pm 0.026$
337	$45.6 \pm 1.2$	$2.56 \pm 0.10$	$1.021 \pm 0.060$
354	$3.68 \pm 0.39$	$1.60 \pm 0.21$	$0.130 \pm 0.022$
358	$37.8 \pm 2.3$	$2.72 \pm 0.22$	$0.799 \pm 0.080$
376	$6.07 \pm 0.57$	$1.44 \pm 0.17$	$0.238 \pm 0.036$
381	$12.7 \pm 1.4$	$2.53 \pm 0.35$	$0.287 \pm 0.050$
391	$50.8 \pm 2.1$	$9.80 \pm 0.51$	$0.302 \pm 0.020$
394	$2.25 \pm 0.78$	$2.03 \pm 0.79$	$0.063 \pm 0.033$
400	$4.58 \pm 0.44$	$2.03 \pm 0.23$	$0.129 \pm 0.019$
406	$8.18 \pm 0.82$	$3.99 \pm 0.52$	$0.118 \pm 0.019$
414	$1.83 \pm 0.26$	$2.55 \pm 0.45$	$0.041 \pm 0.009$
420	$4.90 \pm 1.1$	$6.8 \pm 1.7$	$0.042 \pm 0.015$
427	$0.40 \pm 0.18$	$0.68 \pm 0.38$	$0.032 \pm 0.023$
428	$26.5 \pm 2.4$	$12.70 \pm 1.9$	$0.121 \pm 0.022$

FIG. 2.1 Summary of the results of measurements of [NaganoWatson00], in the air, with 1013 hPa and 20°C.

Just like the expression of the efficiency of the fluorescence process ,the yield (in photons per meter) is parameterized by the wavelength. There thus exists a couple of parameters

( $A_v$ ,  $B_v$ ) for each line. Those are derived from yield measurements made by varying the gas pressure. Table 2.1 gives the values of  $A_v$  and  $B_v$  deduced from the measurements by [Nagano+04], as well as the fluorescence yield. These measurements were made with a Strontium source in air, at 1013 hPa and 20°C. The total yield from 300 to 430 nm is  $4.05 \pm 0.14$  photons per meter. This model will be used in chapter 7 for the normalization of the results.

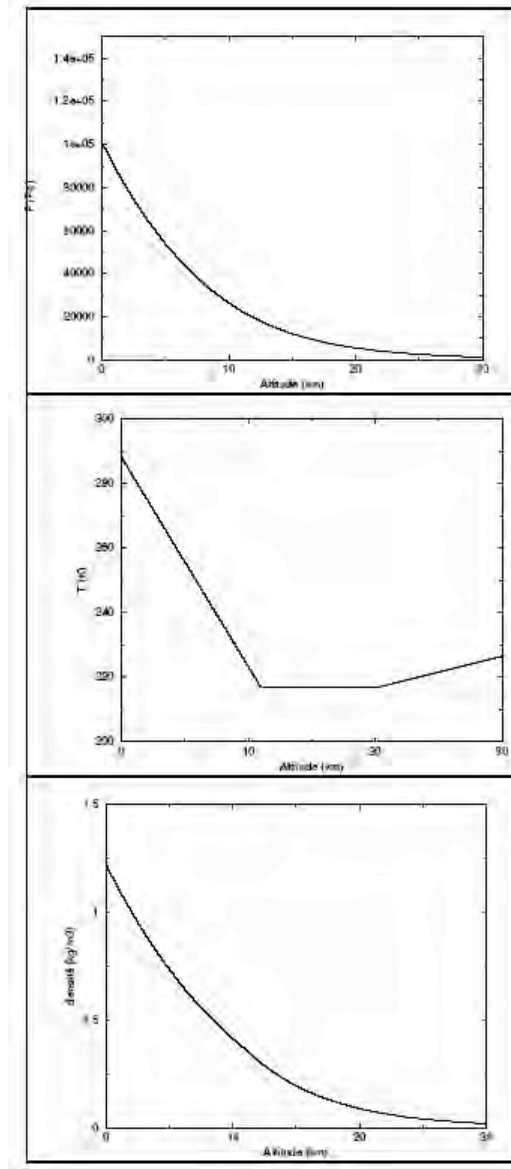


FIG.2.5 Variation of the pressure, temperature and density in function of altitude

As for the preceding paragraph, this simple model can be refined by taking account the chemical composition of the atmosphere and of the different behavior of the 1N and 2P systems. There still, one will refer to [Keilhauer+05]. The graph of figure 2.6 shows the awaited variations of  $Y$  as a function of altitude for the principal parameterizations used. The result of the most recent measurement and its variation ([Nagano+04]) are represented

by black triangles. The value shown in this graph with altitude 0 is 3.7 photons per meter, and not 4.05 as indicated higher, because only the lines from 300 to 400 nm were counted.

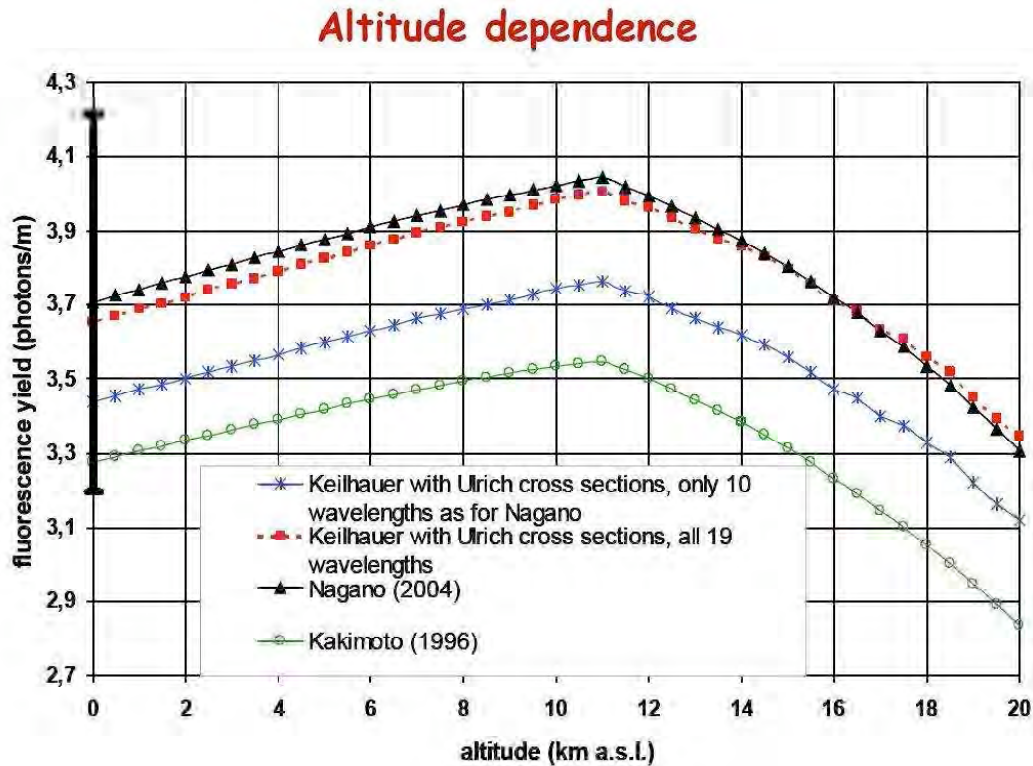


FIG.2.6 Variation of the fluorescence production rate with altitude. Values at sea level are the results of experiments, normalized to the US standard atmosphere conditions. The variations result from different models. On the Nagano value an error bar of 13% is indicated. This value is 3.7 photons per meter and not 4.05 as indicated in the text because it includes only the lines between 300 and 400 nm [Keilhauer+05].

The comparison of figures 2.5 and 2.6 show that the variations of  $Y(z)$  follow primarily those of the temperature  $T(z)$ , which is not monotonous. The inversion of temperature observed around 11 km corresponds to the change of slope of  $Y$  to the same altitude.

Each curve of figure 2.6 corresponds to one particular parameterization or to a different number of wavelength. These parameterizations are however very similar, because the variations which they produce are almost identical. This is due to the existence of a single basic model, the one described above. The only refinements brought here relate primarily to the composition of the medium and to the values of the cross sections of the collisions between the different molecules. The relative errors that the different authors who measured the pressure dependence for each line are very small. On the other hand, their absolute error is always about 10 to 15%.

## Absolute scale

Figure 2.6 shows clearly that the absolute scale of the fluorescence yield is not fixed. The black error bar added on the value of [Nagano+04] represents an uncertainty of 15% on the fluorescence yield. It shows well that for the moment, all the measured values are compatible. An error of 5% or less on the same result would make the two lowest values less credible.

Measurements are not all made in the same conditions of pressure, of temperature or energy. Thus, for each  $Y$ , the electron energy value (corresponding to a  $dE/dx$ ) has to be specified. The pressure, temperature and density selected for the normalization of this work are those of the US Standard atmospheric model at sea level [uss]. They are indicated in table 2.2.

Pression	Température	Densité
1013.30 hPa	288.15 K	1.225 kg.m <sup>-3</sup>

Tab.2.2 Pressure, temperature and density at sea level in the 1976 US standard model.

## 2.3 Conclusion

The theory of fluorescence is well known and rather well understood. Now, the application to cosmic rays involves a development of the experiments on molecular nitrogen excited by electrons. Certain parameters must be better controlled to fulfill the requirements of the physics of cosmic rays, especially the variation of the fluorescence yield with the electron energy. But the knowledge of the absolute value of the yield in air to better than 10% is essential.

The low value of the detectors efficiency makes delicate the precise determination of the absolute scale of fluorescence production. Errors associated with the fluorescence yield are still 13% at least. Without a measurement of the yield of the photomultipliers used in measurement, made at the laboratory, it would not have been possible to improve the precision on  $Y$ . The following chapters describe these two steps: determination of the production of fluorescence, and measurement of the detectors efficiency. They show in detail the method employed to decrease this error and the results obtained.

# Chapter 3

## Method Adopted in the Measurement of Fluorescence Yield

This chapter explains how, on the basis of pre-necessary physics of the cosmic rays and of the emission of fluorescence, we designed and carried out the assembly with which we measured and decreased uncertainty on the fluorescence yield.

### 3.1 Aim of the measurement

As we have it in the preceding chapter, the shower develops during its descent in the atmosphere. The important quantity for cosmic rays experiments is thus the variation of the fluorescence yield versus altitude. These variations are very similar from one model to another. But its absolute yield (in photons per meter) at a given altitude is known only with an error of 10 to 15%. Current experiments ([Nagano+04], [iwf]) do not manage yet to decrease this uncertainty. They measure the absolute yield of the individual lines versus pressure by means of narrow filters.

It is important to keep in mind the goal of our measurement: it is it which imposes to us the precautions which we took, and the calibrations which we have made. Our objective is to reach an accuracy of 5% for the measurement of the absolute yield.

We use a  $\beta$  source to measure:

- on the one hand, the fluorescence yield integrated from 300 to 430 Nm. This already was made by other experiments, but the systematic error is always higher than 10%;
- on the other hand, the continuous spectrum of fluorescence, by means of a grating optical spectrometer, which has never been done with a source, i.e. with energies around one MeV.

### 3.2 Geometry of the bench and detection of the electrons

The average length traversed by an electron in the field of view of a photon-PMT is one of the key sizes of measurement. For this reason, the geometry of the assembly must be

perfectly controlled: if the volume of gas in which the produced fluorescence can be detected is precisely defined, the average range of the electrons is also defined.

Two precautions were taken concerning the electrons. First of all, the solid angle of the source with respect to the PMT-electrons is defined by a plastic scintillator shaped as a truncated cone. In addition, a simulation was carried out to study the importance of different effects which can disturb the electrons trajectory.

Finally, the source having a very high activity, it is essential to have acquisition electronics sufficiently fast to stand counting rates about a MHz. We will see that among these pulses, random coincidences and pile-up (addition of two successive signals) are not at all negligible, but well controlled.

### 3.3 Detection of the photons

In one direction, the photons are detected by a PMT covered with a band pass filter [300, 430 nm]. The accuracy of the yield measurement was maximized:

- by reducing the distance between the enclosure of fluorescence and the PMT to the minimum;
- by limiting the effective detecting surface of the PMT, in order to increase the efficiency of the PMT itself.

In another direction, the fluorescence is analyzed by a grating spectrometer and detected by another PMT. The spectrometer efficiency, an old model, is not very well-known. However, it is the first time that the nitrogen spectrum excited by electrons from approximately 1 MeV will be measured. This is only possible because the source is sufficiently active, limiting the duration of a data acquisition run.

Here, the efficiency of detection is maximized in intercalating a convergent lens between the enclosure of fluorescence and the input of the spectrometer, in order:

- to increase the number of photons at the spectrometer input;
- to optimize the use of the spectrometer itself by respecting its numerical aperture.

### 3.4 Calibration of the photomultipliers

Let us recall that an electron traversing one meter in the air produces only 4 fluorescence photons on average. PMT-photons employed are conceived to work in such conditions, i.e. at a very low level of light. But the maker gives their efficiency with 15 to 20% of uncertainty. To arrive to a precision of the order of 5% for the measure of the fluorescence yield, it is necessary to reach approximately 3% on the efficiencies of the PMTs.

For this reason we proceeded ourselves to make the absolute calibration of our PMT-photons. It is important to stress that this calibration is made in same conditions as the measurement of fluorescence itself. Its settings in required two experimental steps, one relative, the other absolute. For the latter, an innovator method allowed us to reach the desired precision.

### 3.5 Conclusion

The two following chapters describe the measuring bench itself and the steps of its calibration. Chapter 6 details the absolute calibration of the photodetectors, and gathers two measurements:

- that of the efficiency of each one of our photodetectors under the conditions of use of the measurement of fluorescence,
- then only, that of the fluorescence yield itself while using these photodetectors.

Finally, chapter 7 gathers the results of the integrated and spectral measurements in nitrogen and in air.

Second part

Measurements

# Chapter 4

## The Bench

This experiment is motivated by the need for a measurement of the cross section of fluorescence with, if possible, less than 5 % uncertainty. This level of precision is very difficult to be reached. We thus sought to conceive a measuring bench in which one can exert an accurate check on all uncertainties bound with

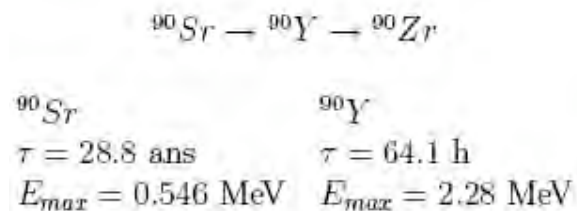
- the electrons: numbers, energy, distance covered;
- gas: purity, pressure, temperature;
- the emitted photons: solid angles, wavelength, numbers, lifetime of the excited levels;
- equipment: efficiency of photomultipliers and spectrometer.

This part details how the bench of measurements works and of its data acquisition. Fluorescence is produced by the excitation of gas nitrogen molecules by electrons generated by a radioactive source. Figure 4.1 shows a diagram of the complete bench.

### 4.1 Production of Fluorescence

#### 4.1.1 The source

The source used is  $^{90}\text{Sr}$ . The electrons are produced in majority by the  $\beta$  disintegration of the daughter element of strontium, yttrium, according to the following decay chain:



Because the mean lifetime of strontium is much longer than that of yttrium, it ensures that the yttrium activity remains constant during the three years of use in this experiment. The

activity of the source is measured at each run in order to normalize the results. The electrons must cross an aluminum foil 0.02 mm thick.

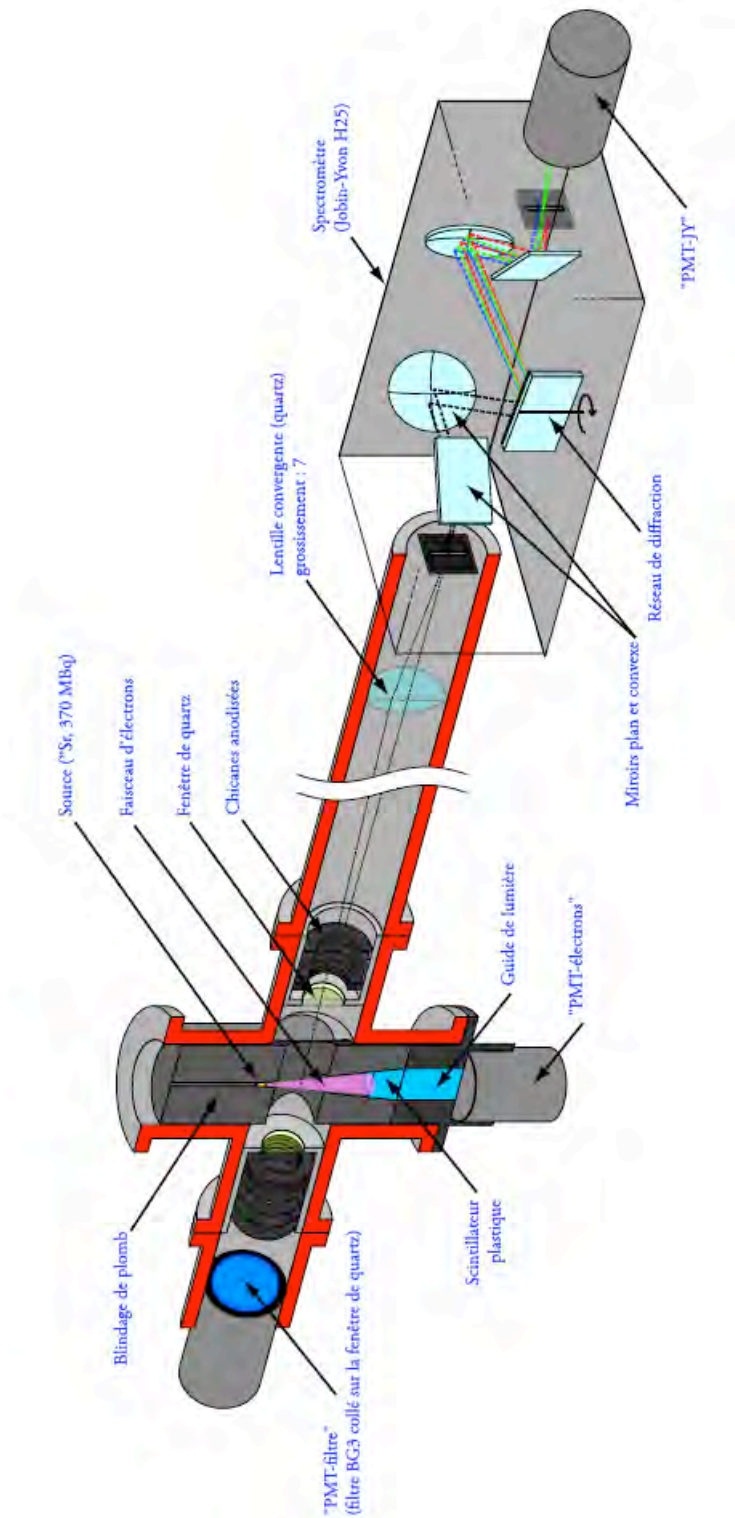


FIG.4.1 Complete diagram of the bench.

The curve of figure 4.2 shows the  $\beta$  spectra of each element. A vertical line indicates the cut of approximately 70 keV thus induced. The energy thresholds of the electrons used for the measurements are indicated by of arrows.

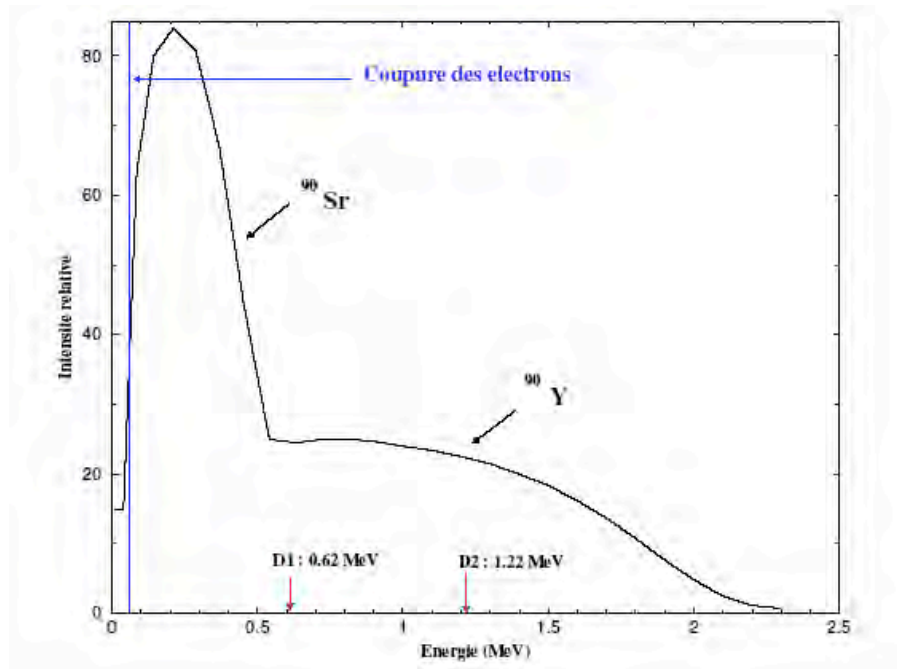


FIG.4.2 Spectrum of strontium and yttrium. Maximum energy is 2.28 MeV. [Hansen+83]

This activity is considerable: 370 MBq, it is known to within 30%. It allows to reduce the duration of each run and to minimize the statistical errors while preserving the control of the dead times. As a comparison, the sources employed in similar experiments have activities respectively 100 ([Nagano +03],) and 10 (Waldenmaier in [air]) times weaker, which implies runs of approximately 70 h. Here, about ten hours are enough. On the other hand, the electrons counting rate of, taking into account the geometry of the assembly, is considerable (see further). Contrary to quoted experiments, random coincidences and pile-up could not be neglected. The acquisition electronics will need protections against these two effects, while being able to measure them in order to account for it accurately. The counting scalers will also have to be sufficiently fast, i.e. at least twenty times faster than the highest rate.

The energy loss of an electron at our threshold (approximately 600 keV) in 10 cm of air with atmospheric pressure, is of 12 keV. This energy loss thus does not have importance on the shape of the observed spectrum.

The lifetimes of the nitrogen molecular levels emitting photons are of the order of a few tens of nanoseconds. The counting of temporal coincidences between the photons and the electrons removes part of the background noise of the PMT-photons due to X-rays (created by the interaction of the electrons of the source and surrounding materials, see part 4.1.3) and with the photocathode dark current of the photomultipliers.

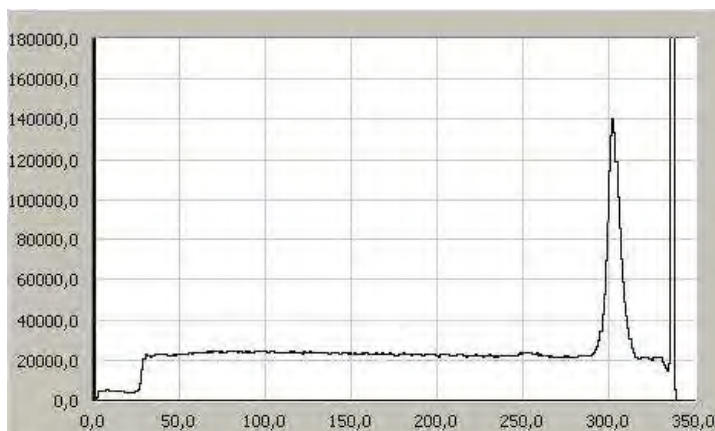


FIG.4.3 Example of TDC spectrum reversed (see text) of the integrating of fluorescence (300 to 430 nm). The triangular part is the signal itself: the exponential decay of the desexcitation of the nitrogen molecules. The flat part corresponds to random coincidences between the electrons and the photoelectrons emitted by the photocathode without a real fluorescence photon. The vertical scale is the number of events, and the horizontal scale is the TDC channel.

One can further increase the ratio Signal/Randoms by using the temporal spectrum of de-excitation of the levels. It is an exponential decay whose exponent is the lifetime of the excited level. By definition, the random coincidences with photons not coming from fluorescence have no particular characteristic: their spectrum is flat. If one considers rates of  $2 \cdot 10^6$  per second for electrons and 1000 per second for the photoelectrons in a 100 ns window, the rate of random coincidences will be  $f = 110 \cdot 10^{-9} \times 2 \cdot 10^6 \times 1000$  that is to say  $f \approx 220$  per second. These randoms are distributed on approximately six times more time that the peak of the fluorescence signal, which is quite acceptable. The figure 4.3 shows such a spectrum: the distinction is clear between the signal and the background made by the randoms.

#### 4.1.2 Detection and counting of the electrons

The electrons are counted by a photomultiplier tube (PMT) in front of which a plastic scintillator stopping the electrons has been fixed. It transforms each electron in a number of photons proportional to the energy of the electron. The scintillator is NE102 (Nuclear Enterprise) whose response corresponds to 65% of that of anthracene, the reference scintillator. A cylindrical Plexiglas light guide is inserted between the scintillator and the PMT, which ensuring airtightness for the gas (the scintillator is in the gas whereas the PMT is outside). Between this cylinder and the PMT, a second kaleidoscopic guide of hexagonal section (10 cm height, “diameter” of 3 cm) homogenizes the light for a uniform response of the detector and to improve its energy resolution.

Each electron of 1 MeV produces approximately 10 000 photons in the scintillator, that is approximately 2.000 photoelectrons. It is thus not necessary that the PMT gain be very

high. The ADC used (LRS 2249A, CAMAC) have 1024 channels, which corresponds to 256 pC. The gain of the PMT is correct if the maximum of the  $\beta$  spectrum, observed after the signal goes through a gain 10 amplifier, is around channel 200 (taking account the pedestal). This corresponds to a PMT gain of approximately  $10^4$ . The selected tube is a XP2262 of Photonis. It is equipped with an active base. In a traditional base, the current in the PMT and in the base are in parallel. If the current of the PMT increases too much because of the counting rate, that of the base decreases. Inter-dynodes voltages also decrease and the gain drops. Here, the voltage divider of the last stages of the PMT is made with transistors and diodes instead of resistances and capacities. The active elements adapt to the current of anode, which can be very high because of the great number of emitted photoelectrons. The last stages are fed separately, by a negative 800 V power supply with high current, so that the PMT remains stable up to rates of  $10^8$ .

### 4.1.3 Definition of the volume of fluorescence

Naturally, the electrons of the source are emitted isotropically. As the source is immersed in gas, fluorescence takes place around. In this case, the volume of fluorescence is the whole volume of gas to which electrons have access. But the useful volume for detection, i.e. volume where photons emitted on the way of the electrons can reach the photodetector, is badly defined. It is in effect necessary to know the distance covered by the electrons to estimate the fluorescence yield in the standard units, i.e. in a number of photons by electron per traversed meter.

Two methods can constrain the fluorescence volume. The first consists to collimate the source and to thus create parallel beam of electrons. It is the solution adopted by [Nagano+03] and Waldenmaier (in [air]). One lead tube with a thick wall is used as a collimator insofar as it absorbs the electrons which cross it and let pass only those which are emitted in its axis (see the diagram of left of figure 4.4).

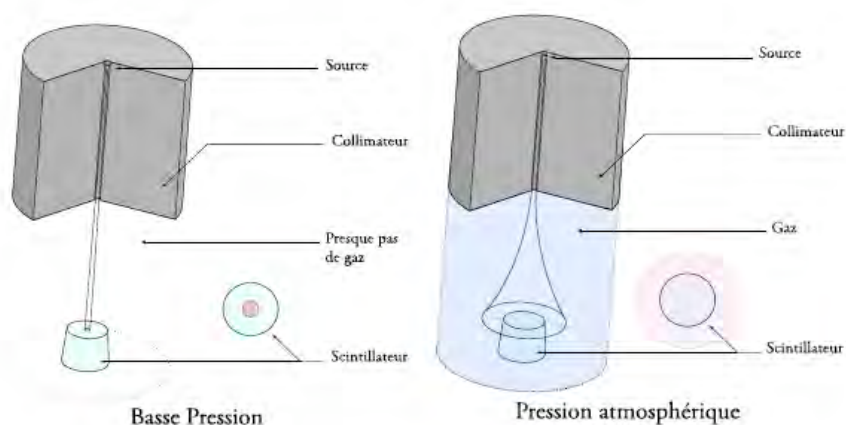


FIG.4.4 In the vacuum (left diagram), a parallel electron beam of is correctly collimated by the lead cylinder. The counting rate is thus maximum. On the other hand, at atmospheric pressure, the electrons diffusion of the in the gas widens the beam and decreases the rate of detection of the electrons.

The idea is that the linear density of electrons is constant, and that consequently, the solid angle in which the PMT detects the fluorescence is easy to calculate. But the diffusion of the electrons first on the walls of the lead tube, and second in the gas, makes reality more complex. In effect, a difficulty appears when one wants to study the dependence of fluorescence yield with the pressure of gas. With a low pressure, everything goes effectively as indicated on the diagram of right-hand side of figure 4.4. The electrons are sufficiently collimated for the of beam section, i.e. the diameter of the tube, is smaller than that of the scintillator: all electrons who take part in fluorescence arrive at the scintillator.

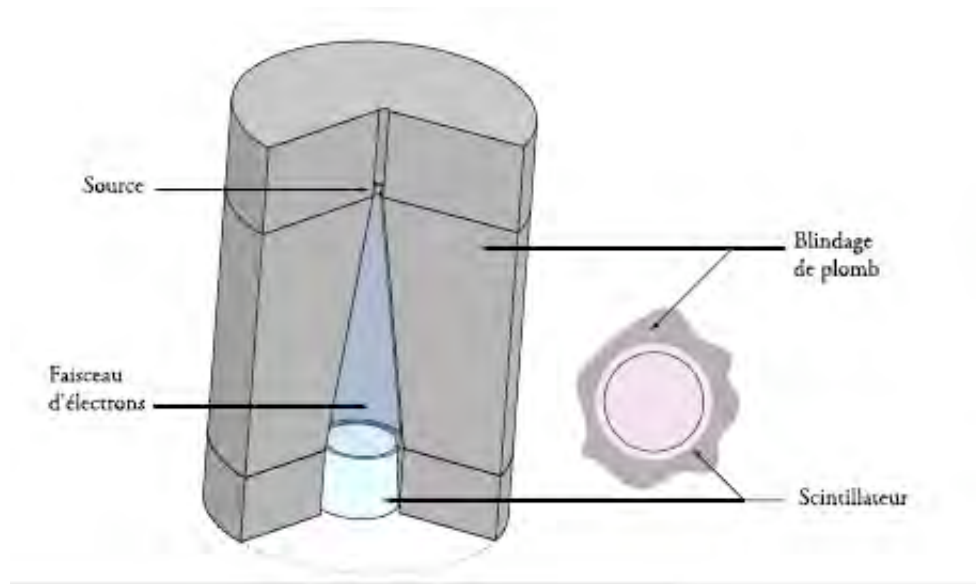


FIG.4.5 The source is not collimated, therefore the scintillator always receives the maximum electrons even when pressure varies. Here, only the absorption by gas decreases somewhat the counting rate (see text). Naturally, so that the photons are detected, a passage is made through the lead shielding (horizontal cylinder of 40 mm diameter).

On the other hand, it is not any more the case with high pressure. The electrons are more diffused in the volume of the enclosure: the beam widens, and ends by having a section more important than that of the scintillator. By losing electrons, the rate of coincidences will also decrease, and it runs will have to be longer. Moreover, this is crippling when the desired precision is large: if the detector of the electrons has a counting rate variable with the pressure, the responses, dead times and gain will also vary from one measurement to another.

The other solution follows to some extent, the opposite reasoning. Since increasing pressure widens the beam, make the beam already broader than the scintillator at low pressures. In this case, it is the scintillator itself which defines the solid angle. Thus the useful volume of fluorescence will be a truncated cone (see figure 4.5). When the pressure increases, there is on average as much diffusion towards the inside of the scintillator that towards outside. On the other hand, electrons of low energy are easily stopped. Counting

rates are practically stable. We will see in part 4.3.3 the lead cone effects, or rather the absence of effects due to the diffusions of the electrons in lead.

Finally, one has to think of protecting against the X-rays, main background noise of photons at this level of the experiment. The interaction of the electrons of the source with matter which surrounds it (bremsstrahlung) creates an important quantity of X-rays. In reaching the PMT-photons nearest, X-rays generate a background noise whose level largely exceeds that of the fluorescence signal, because they create electrons by interaction in all materials met, and thus in the PMT. Thus the matter to cross to reach a PMT must be sufficiently dense and thick for that created X-rays are absorbed. The shielding is a lead cylinder of almost 50 mm of radius around the source. It fills the gas enclosure down to the plastic scintillator. It is hollowed out of a vertical cone 30 mm in diameter, a little wider than the scintillator cone (truncated cone of 20 and 28 mm at the bases and 20 mm of height) and of a horizontal hollow cylinder 40 mm in diameter located in the middle of the cone, so that the photons arrive at the PMT.

Diagram 4.6 illustrates this part and indicates them dimensions of the various elements. Useful volume of fluorescence is a truncated cone of approximately 46 mm in height and 14 and 17 mm bases. The geometrical efficiency of the source towards the scintillator is  $1.6 \cdot 10^{-3}$ . Under these conditions, one gets approximately  $10^6$  counts per second in the PMT of the electrons. We will see later we measure in fact approximately  $2 \cdot 10^6$ . Consequences of such a counting rate are perfectly well known for all implied instruments: PMT, voltage dividers, scalars, acquisition electronics. Experiments on accelerators beams are the best example. One can already indicate that there are only a few hundreds of coincidences per second between the photons of fluorescence and the electrons. These coincidences are used as a trigger for the ADC and TDC

## 4.2 Optical elements

### 4.2.1 The photons trajectories

Fluorescence being isotropic, a good control of the solid angles is mandatory and sufficient. Among the emitted photons, some will reach one of the two detectors. Black baffles are placed on both sides of the fluorescence volume on the way of the photons to absorb those which would be reflected by the walls towards the photocathode (see figure 4.6). The tubes are PMT XP2020Q of Photonis. the letter Q, for quartz, means that this type of tube is provided with a silica window and is thus especially adapted to the measurements in the ultraviolet. As one can see it on figure 4.7, it is not the case of borosilicate, used by [Nagano+03] and by the Auger experiment. The detection of fluorescence with borosilicate is thus less efficient by approximately 20%.

Fluorescence has a very weak yield, only about 20 photons by electron and meter in nitrogen and 4 in air. Counting rates of PMT photons will be very low. They will work in single photoelectron mode, i.e. with very high gain. Their voltage divider was designed for



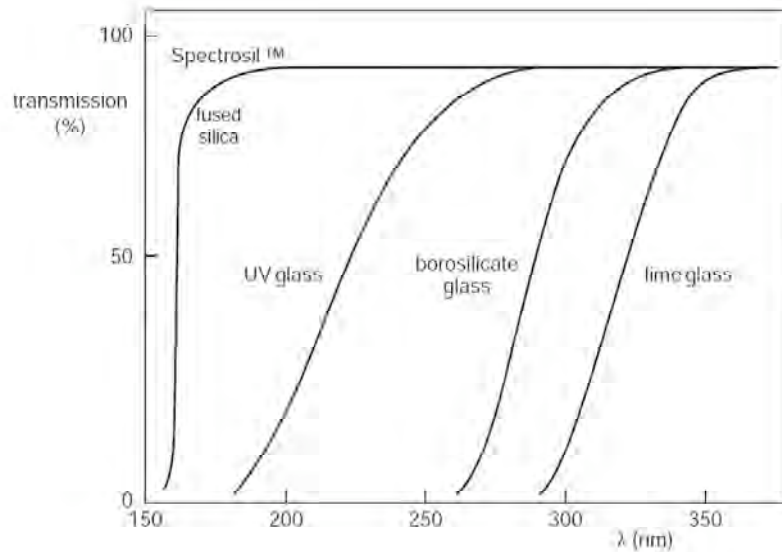
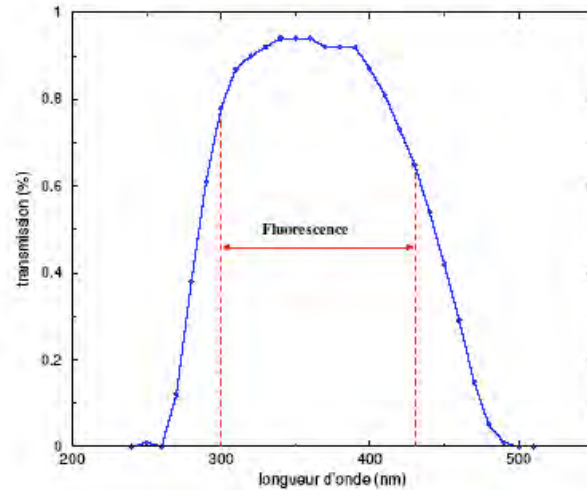


FIG.4.7 Transmission curves of most current photomultipliers windows. Most fluorescence experiments use borosilicate windows. [Pho02]

The first PMT carries BG3 filter of Schott (34 mm in diameter and 2 mm thickness), who is transparent only in the spectral interval of 300 to a little more than 400 nm (see the curve of transmission represented figure 4.8). It is glued on the photocathode with an adhesive Epotec N 301-2, which has the same refraction index than glass and than the filter. Thanks to this filter, only the fluorescence lines are detected, and one maximize the signal-to-noise ratio. PMTs of telescopes of HiRes, Auger or EUSO are equipped with these filters, or identical filters. Finally, a circular black diaphragm occults the peripheral part of the filter and window from the PMT to leave only an effective detecting surface 20 mm in diameter. This diaphragm size was determined after the analysis of the PMT efficiency versus the position of the point of impact of the photon on the photocathode. If the geometrical efficiency in the center of the cross was reduced ( $4.19 \cdot 10^{-4}$  instead of  $1.21 \cdot 10^{-3}$ ), the average PMT efficiency is better: 18.92% instead of 12.17%, and especially much better controlled (3% of uncertainty instead of 15 % at least, see chapter 6.3). Awaited counting rates, apart from the background noise of the PMT, are of approximately 900 per second in nitrogen (mainly because of the proximity of the source) and 70 per second in air.



4.8 Curve of transmission of BG3 filter glued on the photocathode of PMT-Filter. It is shown the real transmission meaning the filter thickness (2 mm) and the single diaper (loss of 4% for only one side of the filter is exposed to air) were taken into account by together with Schott's data of.

The figure 4.9 shows the geometry of this part of the slotted measuring section.

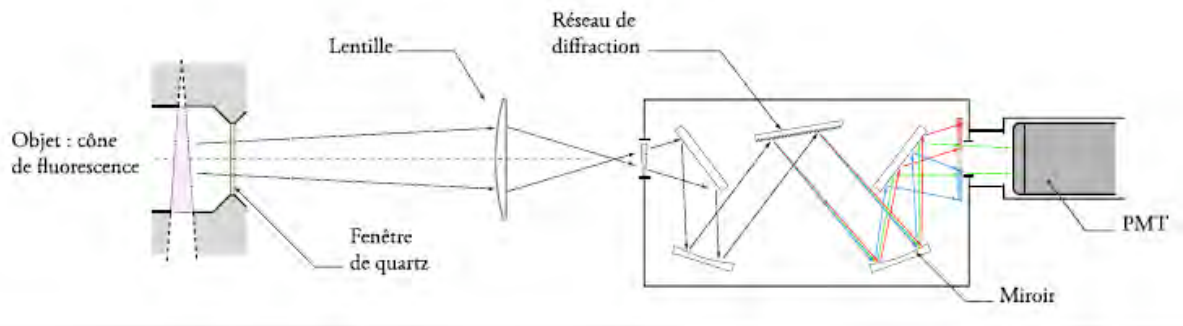


FIG.4.9 Schematic representation of the bench optics.

The other PMT is placed on the same optical axis, at the other end of the bench. Coupled with a grating spectrometer, it carries out the spectral analysis of fluorescence, like [Nagano+03] and Waldenmaier ([air]) do it with narrow filters. Use of a spectrometer has a double advantage: the spectral study is not limited to the wavelengths of the narrow filters, and to make no assumption on the proportion of fluorescence spectrum which is not detected (because outside the filters bandwidths). The resolution of a spectrometer is not necessarily much better than that of filters. Filters used in the source experiments have a width of 10 nm, against 6 nm for the spectrometer of this measurement when the entry and exit slits are opened to the maximum. But this is compensated by the possibility of a

continuous variation of the wavelength. In this work, the spectrometer is effectively used with the maximum opening of entry and exit slits in order to maximize the very weak counting rates.

The spectrometer is a H25 by Jobin-Yvon grating spectrometer, assembled as indicated on figure 4.9. Its opening is  $F/4$  with  $F = 25$  cm, which corresponds to a numerical aperture  $ON$  (for “Ouverture Numerique” in French) of

$$F/4 = \frac{1}{2 \cdot ON}$$

that is to say  $ON = 0.125$ , and a half angle  $\alpha$  such as

$$ON = N \sin \alpha$$

from where  $\alpha = 7.18^\circ$ . The entry and exit slits are adjustable, to the maximum of 2 (horizontal) x 7 (vertical) mm. The smaller this size, the better is the resolution. On the other hand, the spectrometer receives less light, and furthermore the selection in wavelength decreases still more the number of photons likely to be detected by the PMT.

In addition, the surface of the entry slit is so small compared to the fluorescence zone that the losses will be huge if the spectrometer is placed directly next to the enclosure. It is thus mandatory to proceed differently, and to find means of concentrating the photons emitted at the ends of the useful volume. A simple and rigorous solution consists in inserting a convergent lens in this optical assembly, in order to:

- make of the fluorescence zone an optical object whose image is focused in the plane of the entry slit of the spectrometer,
- to respect the numerical aperture of the spectrometer to avoid losses inside it.

These requirements were optimized with the use of a silica lens with an antireflection coating. Its focal length is  $F = 150$  mm and its useful diameter 46 mm, the largest commonly available. It is placed at 171 mm of the spectrometer entry slit. The opening of this lens is then  $7.64^\circ$ , to compare with the  $7.18^\circ$  of the spectrometer. But since the quartz window of the cross has a diameter of 36 mm, the effective opening is not any more than  $6.01^\circ$ : all the fluorescence light is included in the opening of spectrometer. The magnification of this assembly is  $1/7$ , which means that the image of the fluorescence zone is 7 times smaller than the zone itself: 2.14 x 5.14 mm. The image is thus, in its height, entirely contained in the slit. The critical parameter for the detection of the photons is thus the width of the slit. Counting rates waited for are of course even lower for this PMT than for PMT-filter : approximately 60 per second in nitrogen and 10 per second in air for the most important line at 337 nm. Here also, the given numbers are without background noise: one understands better at which point it is crucial to have a background noise as low as possible.

Finally, a spectrometer has a efficiency of the order of 50% (data of the manufacturer), of the same order of magnitude as the narrow filters used in spectral measurements ([Nagano+04]). But it is known only to within 20%, when the filters have a low relative error (less than 10%). Let us recall on this subject that our main objective is to obtain a precise value of the integrating fluorescence production between 300 and 430 nm. Differential measurement is only used to measure the relative intensities of the lines, which has never been made with a source and a grating spectrometer.

#### 4.2.2 Efficiency of the photons detection

The relatively complex geometry of the assembly requires a deep study to determine the solid angle of the fluorescence volume towards each PMT-photon. The Monte Carlo Dolbeau [Dolbeau] simulation makes this geometrical study.

This Monte Carlo simulates the electrons by drawing a random direction from the source position. Only the trajectories which intercept a disc of diameter equal to that of the scintillator are preserved. On each one of these trajectories, a random position and a direction are drawn to simulate the emission of the fluorescence photon.

The photons emitted very close to the source or to the scintillator cannot be detected. It is however possible that detected photons were emitted apart from the limits fixed by the diameter of the cylinder dug in the lead, i.e. at more than 20 mm of the optical axis (vertically), as shown in figure 4.10. To take that into account, the photons emission positions are drawn vertically up to 23 mm from the optical axis (that is 3 mm more than the cylinder radius). The rays which simulate the photons are then registered as detected photons if they reach the PMT's photocathodes.

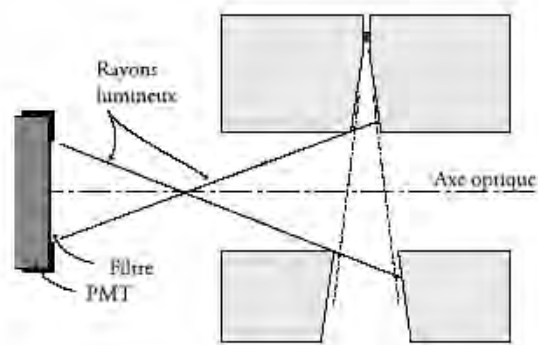


FIG.4.10 Detection of fluorescence photons emitted far from the optical axis

The geometrical efficiencies of each PMT are evaluated this way. Their values are:  $3.689 \cdot 10^{-4}$  for PMT-filter and  $7.481 \cdot 10^{-6}$  for the PMT-JY. This program also allows to evaluate the average length traversed by the electrons in the truncated cone of 46 mm high: it is 46.11 mm.

## 4.3 Interactions of the electrons of the source

Until now, we considered only rectilinear trajectories for the electrons, from the source to the scintillator. Two types of interaction can however disturb their travel, with the gas or with the lead shielding.

### 4.3.1 Emission of secondary electrons

Part of the energy lost by the electrons of the source is by ionization of the gas molecules (nitrogen or other). The ejected electrons, of low energy, who are also called secondary electrons or  $\delta$  rays. They are produced with a probability depending on the kinetic energies of the primary electron and of the  $\delta$  itself:

$$\frac{d^2N}{dTdx} = \frac{1}{2} K \left( \frac{z}{\beta} \right)^2 \frac{Z}{A} \frac{F(T)}{T^2}$$

with:

- $d^2N / dTdx$ , the number of produced  $\delta$  with a kinetic energy  $T$  per unit length ( $\text{MeV}^{-1} \cdot \text{cm}^{-1}$ ),
- $K = 4\pi N_A r_e^2 m_e c^2$  and is worth  $0.307 \text{ MeV} \cdot \text{cm}^2$ ,
- $z = 1$ , the incident particle charge (here, one electron),
- $Z = 7.4$ , average atomic number of the gas (here, dry air without argon),
- $A = 14.28 \text{ g} \cdot \text{mol}^{-1}$ , average atomic mass of the gas,
- $T$ , kinetic energy of the electron ejected (MeV)
- $F(T) = \beta^2 T^2 \left[ \frac{T_{inc}}{T(T_{inc}-T)} - \frac{1}{T_{inc}} \right]^2$  for indistinguishable particles, with  $T_{inc}$  the kinetic energy of the primary electron.

This formula is valid for  $I \ll T < T_{max}$ .  $I$  is the average excitation energy of the medium, (85.7 eV for air). When  $T$  is close to  $I$ , the electron is emitted with a kinetic energy insufficient to move away from the molecule and is captured again: the formula is valid from  $T \approx 1 \text{ keV}$ .  $T_{max}$  is the maximum energy transferable from the incident particle to the ejected  $\delta$ . It is equal to half of incident kinetic energy (interaction of two electrons).

The graph of figure 4.11 shows the variations of the function  $d^2N / dTdx$  with  $T$  for energies  $T_{inc}$  going from 0.5 to 2 MeV. One realizes two things:

- 99% of the ejected electrons have an energy lower than 5 keV (and 76% have 1 keV or less). In the following, one will thus consider only an energy range from 0 keV to 5 keV.
- the number of produced  $\delta$  is independent of  $T_{inc}$ .

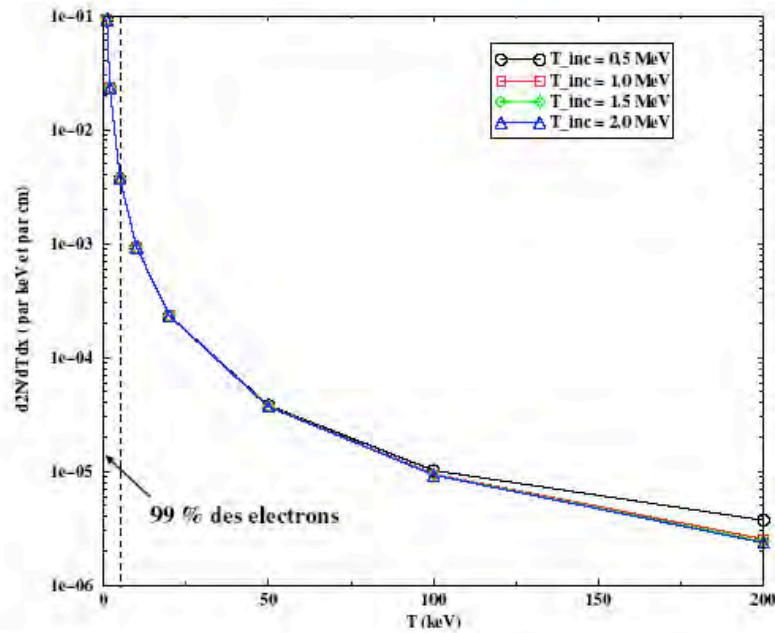


FIG.4.11 Variation of the number of secondary electrons  $N$  produced per unit of length and energy, versus their kinetic energy. Each curve is parameterized by the kinetic energy of the primary electron. At low energies, the number of these secondary electrons is independent of the energy of the electron of the source.

The range of the secondary electrons in air at atmospheric pressure is no more than 2 mm. The widening of the fluorescence volume caused by the emission of a  $\delta$  is thus too weak to modify the angle of view of the PMTs. This was checked in simulations by widening artificially the diameter of the scintillator cone. Each photon produced in the useful truncated cone (such as defined in chapter 4) is in the field of view of the detectors. In our case, the emission of secondary electrons is a negligible effect with regard to the efficiency of detection of fluorescence photons.

In the general case of a shower developing in the atmosphere, one can calculate that the  $\delta$  produced by 1 MeV electrons and at atmospheric pressure have a part in the production of Fluorescence to a total value of approximately 15%. This contribution is already high because the energy of the secondary electrons being very low, their  $dE/dx$  is very large and the probability of fluorescence is all the more important. For example, electrons of 1 keV losing approximately 70 times more energy than at 1 MeV, can produce 70 times more fluorescence photons.

With the average energy of the electrons of a shower (80 MeV) and with a lower pressure (meaning higher in the atmosphere), the  $\delta$  can be more energetic. They can traverse a distance much larger, under the combined effects of a larger range and of the lower pressure, and thus produce fluorescence photons and other  $\delta$ .

### 4.3.2 Deviation of the primary electron

The collision of an electron of the source with a electron molecular deviates the primary education electron of its trajectory. The angle of the deviation is computable according to the laws of relativist kinematics:

$$\cos \theta = \frac{T_e p_{max}}{p_e T_{max}}$$

$T_e$  and  $p_e$  indicate the kinetic energy and momentum of the secondary electron, while  $T_{max}$  and  $p_{max}$  are the maximum values of these quantities which can be transferred to the secondary electron.

As the  $\delta$  has a very low energy, the primary electron suffers a little deviation: to the maximum  $6.1^\circ$ . An electron of the source emitted in the direction of the scintillator thus has a finite probability not to reach it. In this case, it falls naturally into the “inefficiency” of the detection: if it produced a fluorescence photon, it will not be counted as such since any coincidence between electron and photon will be impossible.

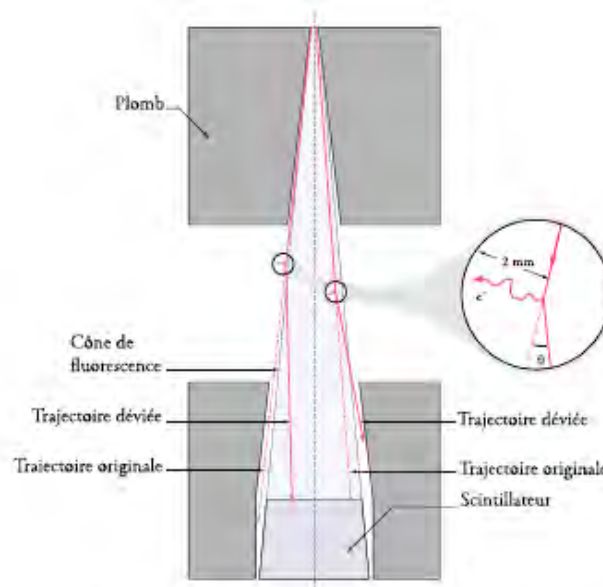


FIG.4.12 Schematic representation of the maximum deviation undergone by an electron of after having produced a  $\delta$ .

### 4.3.3 Diffusion in the lead shielding

Among the electrons whose direction does not intercept the scintillator, some can be retro-diffused by the lead shielding. Changing direction, it is possible that they reach the scintillator. This effect has two consequences:

- to increase the counting rate of the electrons, which is good;
- to modify the energy spectrum of the electrons, which it has to be understood.

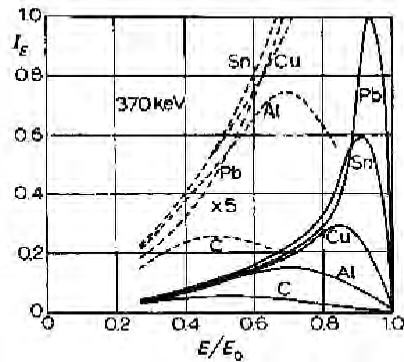


Fig.4.13 Spectrum of the energy loss of 370 keV electrons, diffused in several materials, of which lead. It is to be noted that the low energy electrons lose there approximately 10% there of their energy [Siegbahn].

The final spectrum is thus the sum of two contributions: a direct contribution, whose shape is that of the spectrum of the source, and a contribution of the retro diffusion, whose shape is unknown but which must contain more electrons of low energy. The electrons lose approximately 10% of their energy in lead (see figure 4.13).

A simulation Geant ([Lefievre]) reproduced the geometry of the lead shielding and the interactions of the source electrons. The spectrum of the source was schematized for energies from 0.5 to 2 MeV. It is in black on figure 4.14.

The spectrum of the electrons touching the scintillator is represented in red (bold). It is the sum of the spectrum of the electrons of the source touching directly the scintillator and of that of the electrons having diffused in the lead. As they lose energy in the lead, one finds more electrons of low energy. The difference of the two spectra, i.e. the contribution of retro diffusion in lead, is shown in blue dotted lines.

The real spectrum of the source contains a little more low energy electrons than the simulated one, which does not change anything with the reasoning nor with the result, since only the electrons of energy higher than 600 keV are detected. In the same way, the fact that the statistics of this simulation are not very important does not influence the fluorescence measurement, because in this range of energy, the  $dE/dx$  varies very little.

The real spectrum of the electrons emitted by the source as well as the real spectrum measured by the PMT-electrons are represented on figure 4.15, respectively in black and red. The shift towards low energies is clearly visible. The average electrons energies for each discriminator are calculated from the red spectrum. They are shown in table 4.1, as well as the corresponding  $dE/dx$ .

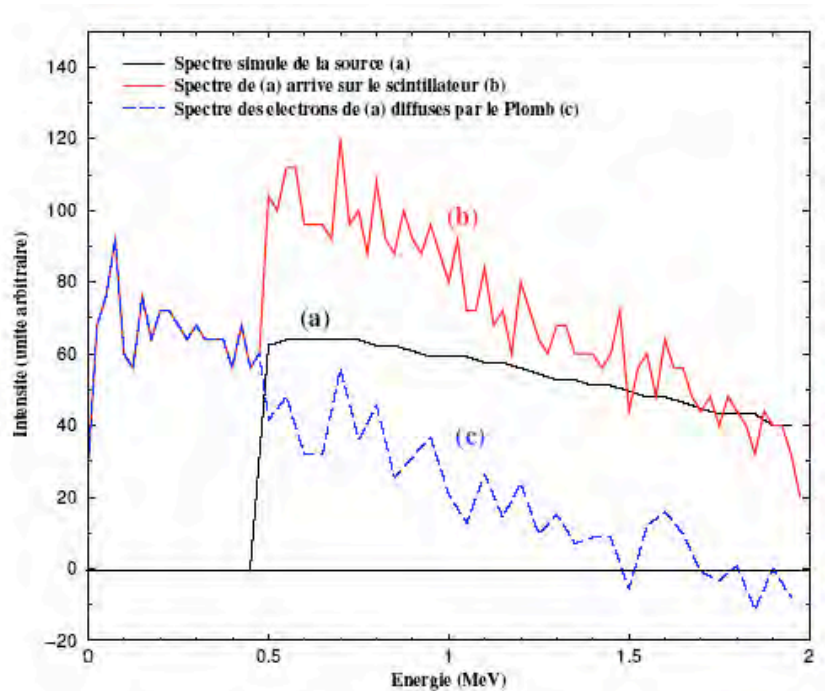


FIG.4.14 Geant simulation of the energy spectra of the electrons touching the scintillator. In black, the electrons which go directly from the source to the scintillator. The shape is thus exactly that of the simulated spectrum of the source. In red, the spectrum of the electrons which touch the scintillator, either they underwent retro diffusion in the lead or not. In blue dotted lines, the difference of the preceding spectra shows only the contribution of the diffusion in the lead shielding.

Seuil (MeV)	$E_{moyen}$ (MeV)	$dE/dX$ (Mev.cm <sup>2</sup> .g <sup>-1</sup> )
0.62	1.1	1.673
1.22	1.5	1.680

TAB.4.1 Summary of the thresholds of each discriminator, as well as average energy electrons above these thresholds and the corresponding  $dE/dx$ .

Finally, the total counting rate of the electrons increases almost by 60%. This is totally compatible with our measurements, taking into account the 30% uncertainty on the source activity (the maker, AEA Technology).

#### 4.3.4 Diffusion in the scintillator

The electrons can also leave the scintillator after they have deposited part of their energy in it. If they arrive again in the zone of fluorescence visible by PMT-photons and if they produce a Fluorescence photon there, the distance which they will have traversed will be more important than what we have taken into account up to now.

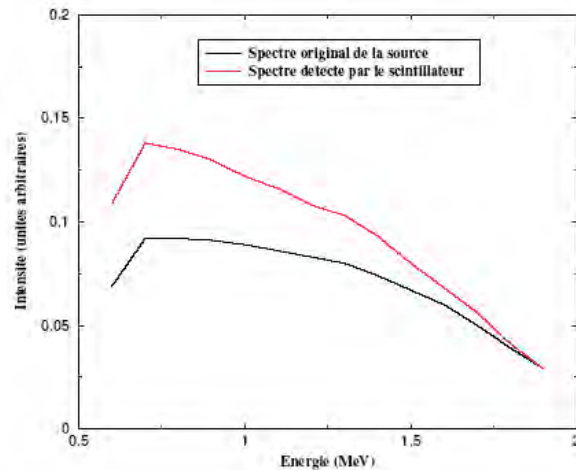


FIG.4.15 In black, the real spectrum of the electrons emitted by the source. In red, that of the electrons detected by the scintillator, after diffusion in the lead shielding. The shift towards low energies is clearly observable.

The same previous study ([Lefievre]) shows that this effect is completely negligible: on 130.000 electrons having deposited more than 600 keV in the scintillator (thus producing a signal which exceeds the threshold of the first discriminator), only one turns over in the fluorescence zone. Taking into account the fluorescence probability and the geometrical detection efficiency, by example for the PMT-filter, one arrives at a rate of  $10^{-9}$ , which is completely negligible.

For the same reasons, the probability that two photons produced by the same electron arrive in a given PMT is very low (since proportional to the square of the geometrical efficiency). If this could happen, it is far from probable that two photoelectrons would be emitted by the photocathode (the PMT are the single photoelectron mode), or if not, two photoelectrons will be counted like only one pulse because of their simultaneity. This effect will thus not be taken into account thereafter.

#### 4.3.5 Conclusion

The choice not to collimate the electrons of the source, has three advantages which allow to control well the geometry of the Fluorescence volume:

- the view angle does not vary because it is limited by the lead;

- a greater quantity of electrons reach the scintillator;
- the measurement efficiency is much better.

## 4.4 Gas control

The gas used is nitrogen or dry air (recomposed dry air of the Messer factory) whose composition is indicated in table 4.2. This industrial air does not have the same composition than the real atmosphere, since it does not contain argon nor traces of other rare gases naturally present in air. But the influence of these impurities on the fluorescence yield is very low (1% for argon) and will be neglected.

The gas is confined in an hermetic enclosure of stainless steel to avoid all pollution by degasification. A mixer, placed behind the bottles, authorizes the passage of one or the other gas or makes it possible to introduce impurities.

Composition de l'air sec (Messer)	
N <sub>2</sub>	79 %
O <sub>2</sub>	21 %
H <sub>2</sub> O	≤ 2 ppm
CO et CO <sub>2</sub>	≤ 0.5 ppm
NO <sub>x</sub>	≤ 0.1 ppm
hydrocarbures	< 0.1 ppm
Ar	absent

TAB.4.2 Composition of the reconstituted dry air used for the measurement of the Fluorescence yield

All optics, past the windows, is in free air, at room pressure and temperature. The windows allowing the photons to reach the detectors and closing the vessel are made out of quartz. Quartz is transparent to fluorescence photons. Two antireflection coatings limit the optical losses to 1% instead of the usual 8% (see the curves of transmission on figure 4.7).

Temperatures and pressures internal and external to the vessel are controlled every minute. The internal probes are placed in the enclosure once for all. They are connected to the data acquisition *via* a slow CAMAC ADC. The calibration of the probes is detailed further.

The gas circulates constantly with an adjustable flow, constant during a measurement, of about 1 L.h<sup>-1</sup> (see the gas flow chart in figure 4.16). This way, very problem linked to ageing, like ozone formation (which absorbs the ultraviolet rays) or degasification by the pipes, is eliminated. Circulation and flow are ensured by Bronkhorst flow meters (precise to better than 1%), an ultra clean pump and a pressure regulator (TESCOM N° 44-4700). The reference of this pressure regulator being the external pressure, it is necessary to measure

this external room pressure precisely. The system was thus calibrated by a precision mercury barometer (barometer of Jean Perrin, precise to a few  $10^{-2}$  Hg mm).

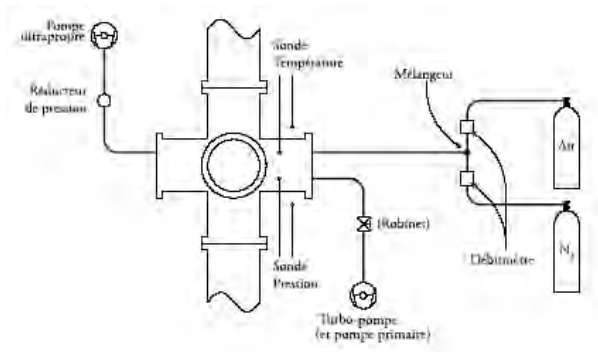


FIG.4.16 Schematics of the gas system

Before the first data acquisition, one could check that the vessel was quite tight by making vacuum (turbo pump). One reaches without difficulty a stable vacuum of  $10^{-5}$  mbar.

## 4.5 Data acquisition

The fast treatment (within a nanosecond) was carried out with NIM modules, and recordings by CAMAC and VME modules connected to a PC with a acquisition program of LabVIEW 6.1. A great part of my personal work was the writing of the data acquisition program under LabVIEW. Appendix A details how the electronic and software data acquisition works.

Figure 4.17 schematizes the acquisition steps. The principle is to retain only the photons which are in temporal coincidence with an electron.

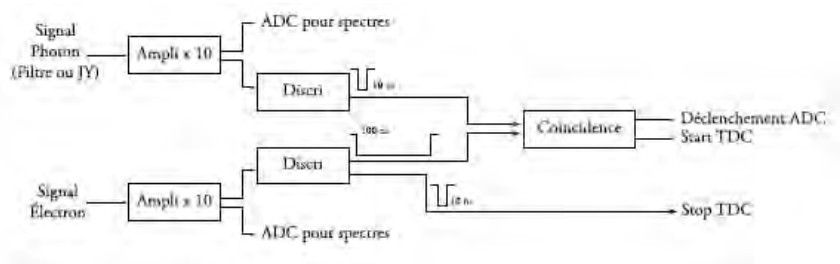


FIG.4.17 Simplified schematics of the DAQ. The complete scheme, with the delay values is in appendix. The electron signal is 100 ns wide at the coincidence input to take into account the molecular levels lifetimes: thus the photon signal is delayed. On the other hand, the TDC stop is short to avoid more dead time

The complete diagram, including the durations of the introduced delays and the discriminators thresholds, can also be consulted in appendix. The measurement itself is

made with the TDC and scalers. Those allow to correct the dead time. Each TDC spectrum is started by a coincidence between the photon signal and the electron signal. Conversion is stopped by the delayed electron signal.

Coincidence between the photon and the electron must take into account the lifetimes of the nitrogen excited levels. One thus introduces here an important dead time, to which is added the recording time of the spectra. Recorded TDC spectra are thus only images, homothetic, of the real spectra, i.e. for which the dead time is null. One corrects this effect by normalizing to the corresponding scalers, which have a very low and measured dead time: respectively 1.2% and 0.7% for the two electron signals.

The role of the ADC spectra is only to check the stability of the PMT gains during the measurements. They are not used in the analysis.

## 4.6 Adjustment of the PMT photons

When the quantity of light is very low, the photons arrive one at a time on the photocathode. The PMT works then in a discrete mode, called single photoelectron mode. Under such conditions, the adjustment of the PMT requires a specific set up. This type of functioning is described in the appendix B. Only the results of these adjustments are presented in this part.

### Gain

By definition, the gain is the ratio of the number of electrons on the anode to the number of photoelectrons emitted by the photocathode. In single photoelectron mode, it is thus directly given by the position of the peak of the single photoelectron on the ADC spectrum. The two PMT were regulated to have the same gain, which put their maximum

	PMT-filtre	PMT-JY
Canal du maximum du pic "1"	185	210
Canal du piédestal	39	33
Gain	$2.3 \cdot 10^7$	$2.8 \cdot 10^7$
Tension	2132 V	2403 V

TAB.4.3 Gain and voltage applied to each PMT. The gains are the real PMT gains. An amplifier placed at the PMT yield multiplies the gains by 10.

towards channel 200. By taking into account the position of the pedestal and that a gain 10 amplifier was intercalated, one arrives at the gains, and thus at the high voltages, given in table 4.3.

### Energy threshold

Removal of the peak “0” by means of a discriminator (see appendix B) also eliminates a small part of the true photoelectrons of the peak “1”. It is thus necessary to evaluate this detection “inefficiency” to be able to correct it in the analysis. Table 4.4 indicates the proportion of lost photoelectrons compared to the full peak “1”.

PMT-filtre	PMT-JY
3.76 %	3.85 %

Tab.4.4 Proportion of lost single photoelectrons by the discriminator cut, relative to the integrating of the peak of the real single photoelectron. No uncertainties are specified on these values, because they are so weak that an error of a few % would be negligible in any case.

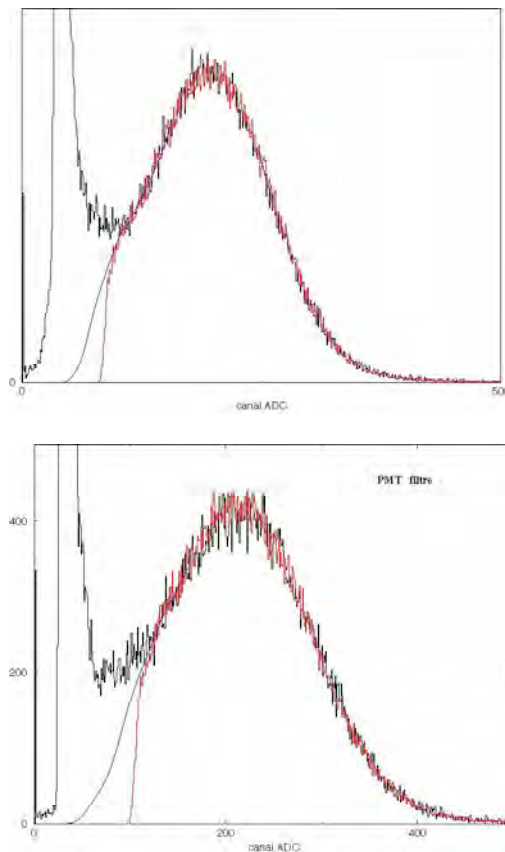


Fig.4.18 Top: spectra of the PMT-filter, bottom: spectra of the PMT-JY. The whole single photoelectron spectrum in black. The narrow (truncated) peak corresponds to the absence of photoelectron when the ADC trigger is the LED generator: there are on average forty times more triggers without detection of photoelectron that with. In red, the same spectrum, once applied the threshold of the discriminator. The loss of real photoelectrons is tiny: it corresponds to the integrating between the blue curve (spectrum of the single photoelectron if there were no “0”) and the real curve in red (see text).

## Chapter 5

### Calibration of the Bench

#### 5.1 Pressure and temperature probes

The absolute reference for the internal and external pressure probes is taken on a mercury precision barometer to which all corrections due to the meniscus, etc have summer applied (precision of reading of 0.02 mmHg). Variation of channel ADC versus pressure is obtained by pumping gas contained in the cross, and measuring the pressure with the manometer incorporated in the pump. The lowest pressure is taken when the pump indicates a pressure lower than  $10^{-2}$  mbar. The point at atmospheric pressure is taken with the barometer. The graph of figure 5.1 shows this calibration.

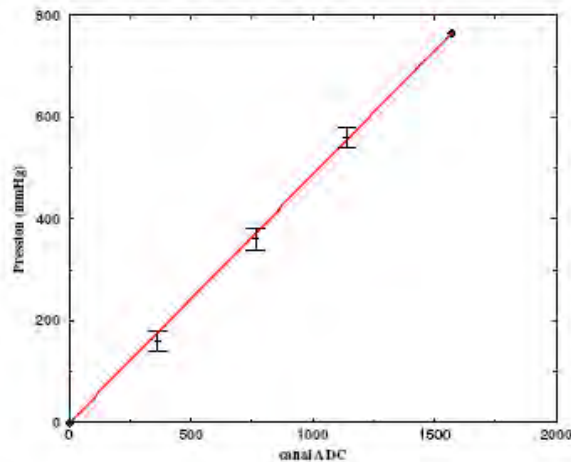


Fig.5.1 Calibration of the internal pressure.

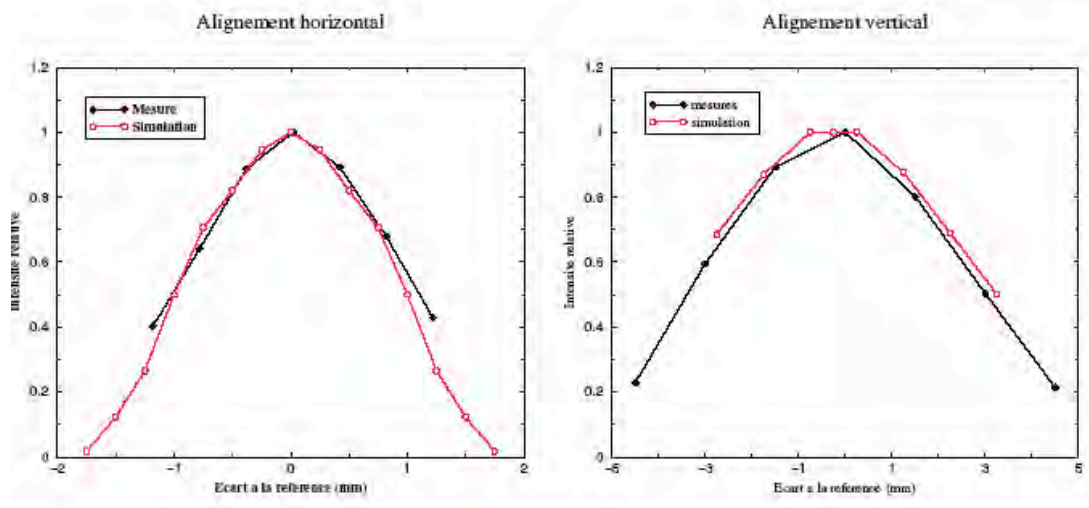
The two temperature signals, internal and external to the cross, are sent to a slow ADC (CAMAC Lecroy 3510 of 11 bits, integration time 42 ms) after having been amplified to increase dynamics. They were have been calibrated by measuring the room temperature during several days.

## 5.2 Centering of the lens

The centering of the lens was made in two times: first the lens is fixed at the good distance from the optical object (fluorescence volume) so that its image that is focused in the plane of the spectrometer entry slit. The object and image lengths were calculated knowing the characteristics of the lens (Edmund Optics C46-278, focal distance 150 mm and useful diameter 46 mm), its desired magnification (7) and finally the numerical aperture of the spectrometer. If one does not want to lose photons, it is essential that the aperture angle of the lens towards the spectrometer is lower than that of the spectrometer. This condition is observed. The object and images distances are respectively 1200 mm and 171 mm.

To adjust this focusing distance, a cone of depolished scintillator, height 38 mm and base diameter 20 mm, was centered in the cross before the strontium source was introduced. Illuminated by a UV lamp, it emits by excitation blue visible light. This light is focused by the lens in the plane of the spectrometer entry slit. The axial position of the lens was thus adjusted according to the clearness of the image observed on the slit (closed).

The lens is mounted on a micrometric movement allowing to center the image of the cone on the slit of entry to better than 10  $\mu\text{m}$  in transverse and vertical. Precise adjustment is made on the most intense line of the spectrum of nitrogen (337.1 nm). Measurements of horizontal and vertical alignment were compared with the simulations carried out by Jean Dolbeau (Monte Carlo [Dolbeau]), and are represented on figure 5.2.



5.2 Results of successive measurements made to align precisely the lens transversely (on the left) and vertically (on the right). The axis origins are relative. Measurements (black curve) are completely compatible with simulation (red curve).

## 5.3 Grating spectrometer

It is very difficult to measure precisely the efficiency of an apparatus as complex as a grating spectrometer. The manufacturer himself provides a spectral calibration with 15 to 20% uncertainty. Nevertheless, a measurement can give us an idea of the difference between the manufacturer data of and our own apparatus, just like for the PMT.

The source is the 400 nm LED matrix. It is a broad source (20 nm FWHM), broader than the response of spectrometer (6 nm). We did not have a UV laser. The response of the spectrometer to a monochromatic beam was obtained with a He-Ne laser, central wavelength 632.8 nm and with naturally a very weak angular dispersion. Figure 5.3 shows the compared widths of the LED and laser, analyzed by the spectrometer opened to 2 mm.

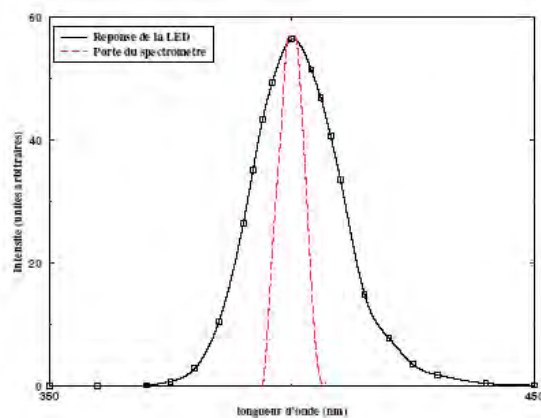


Fig.5.3 Compared widths of the LED and the response of the spectrometer. In black, the 400 Nm LED. In red, the spectrometer response: it is the curve of figure 5.6 for slits of 2 mm, translated to 400 Nm.

As a laser is much narrower in wavelength than the resolution of the spectrometer, only the height of the signal counts, i.e. the intensity of the detected flux (and not its integrating). We can thus build the curve of the spectrometer intrinsic response: it is in figure 5.6. This measurement was made for three different slit widths of (entrance and exit): 2 mm (the maximum), 1 mm and 0.5 mm. In the first approximation, the measured intensity varies linearly with the slit width. The measurement of the fluorescence yield is made with slits open to the maximum. The resolution would be better with narrower slits but, at equal duration, the statistics would be less important, hence the precision would be worse.

The spectrometer was thus calibrated with two wavelengths

- 633 nm with the laser He-Ne
- 400 nm with the LED.

Each absolute efficiency is obtained by comparing the flux received by one calibrated photodiode in the presence of the spectrometer and in its absence. Photodiodes used here

are from Ophir (Ophir Optronics, model PD300-UV-HS), they will be named Ophir 1 and Ophir 2. Their calibration precision is 1.5%. The assemblies are indicated on figures 5.4 and 5.5 in the laser case. For the 400 nm measurement, the LED support was fixed directly on the entry port of the sphere.

The laser light (non-polarized) enters the integrating sphere after diffusion on a Teflon sheet 0.5 mm thick. There is no diffuser for the measurement using the LED. The photodiode Ophir 2 is fixed on a port of the sphere (it is used as reference), while the other port is directed towards the spectrometer. The luminous flux is attenuated by means of two diaphragms of 1 mm diameter separated by 10 mm one from the other, in order to respect the numerical aperture of the spectrometer. The photodiode Ophir 1 is fixed on the exit of the spectrometer.

The intensity measured by each photodiode is recorded and converted into power via their calibration curves. The flux ratio between the two exit is  $7.58 \cdot 10^3$ . Table 5.1 gathers the results of two measurements, as well as the nominal apparatus efficiency.

As the LED is broader than the spectrometer resolution, it normally should be done:

- to measure the spectrum of the LED analyzed by the spectrometer;
- to de-convolute from the response of this last.

One would thus find the “true” intensity of the flux, that one would have measured if this source had been narrower than 6 nm.

$\lambda$ (nm)	Mesure	Donnée Jobin-Yvon
400	15 %	61 %
633	33 %	40 %

Tab.5.1 Comparison between the measured spectrometer efficiency and the nominal efficiency, given by the manufacturer.

However, in this precise case, this step is not necessary. In effect, the photodiode already carries out the integration of the LED spectrum with an uncertainty of 1.5%, the spectrometer being present (integration on 6 nm) or not (integration on 20 nm). By comparing both measurements, one compares already the flux intensities. The efficiency which one wants to measure (which is, by definition, the ratio of the surfaces of the detected de-convoluted spectra with and without the spectrometer) is thus simply the ratio of the fluxes received by the photodiode (see figure 5.3).

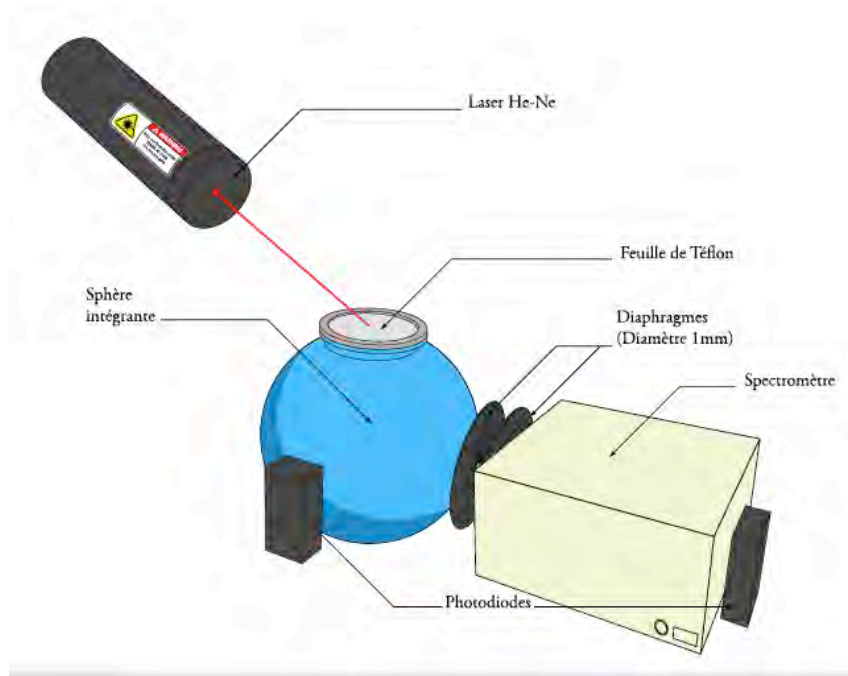


Fig.5.4 Calibration of the spectrometer. After diffusion, the laser light is directed towards a photodiode and the spectrometer. For the 400 nm measurement, the LED support was fixed directly on the entry port of the sphere.

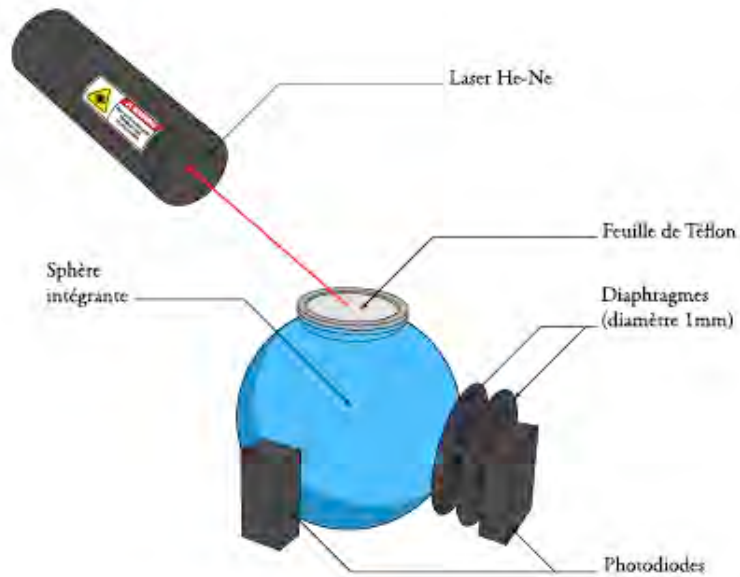


Fig.5.5 Determination of the ratio of the light fluxes for the spectrometer calibration. For the 400 nm measurement, the LED support was fixed directly on the entry port of the sphere.

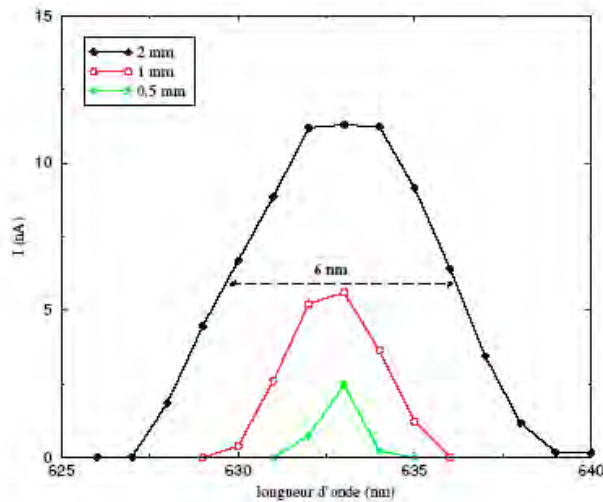


Fig. 5.6 Intensity measured by the photodiode fixed at the spectrometer exit versus wavelength, for three slits openings. The entry and exit slits have the same width. The wavelength of the laser is 632.8 nm.

The efficiency measured at 400 nm has an uncertainty of 10%, mainly because of that on the solid angle of entry in the spectrometer. The efficiency measured at 633 nm has an uncertainty of 20%. Uncertainty on the solid angle at the sphere entry, in spite of the presence of the diffuser, is added to that of the entry in the spectrometer.

There no was specific effort made to improve the precision of this measurement, because the laser was mainly used to measure the of the response width of the spectrometer.

The absolute efficiency curve of the spectrometer, given by the manufacturer when the spectrometer is new, is presented on figure 7.7. Our measurements results are in red. The noted variation between our measurement and the value of documentation comes from the ageing of the apparatus [Hocrelle]. Internal optical elements (four mirrors and a grating) are aluminized, and oxidize with air. After ten years, according to the conditions of storage and the quantity of UV photons received, the loss in efficiency can reach 15% per optical element, that is to say 40% in all. The spectrometer of this measurement is about twenty years old, and was previously used with a deuterium lamp rated at a hundred watts. The efficiency loss is not constant in wavelength, because the system is damaged more quickly in the UV that in the visible.

Finally, one can wonder whether a single point between 300 and 430 nm is enough for a spectral measurement. The efficiency variation of the spectrometer is very important between 633 and 400 nm, and is also very different from the manufacturer data. It is thus possible to imagine a variation higher than the 10% of uncertainty which we quote to the measurement. We will compare at chapter 7 the lines intensities which we measured to those measured by Ulrich [air].

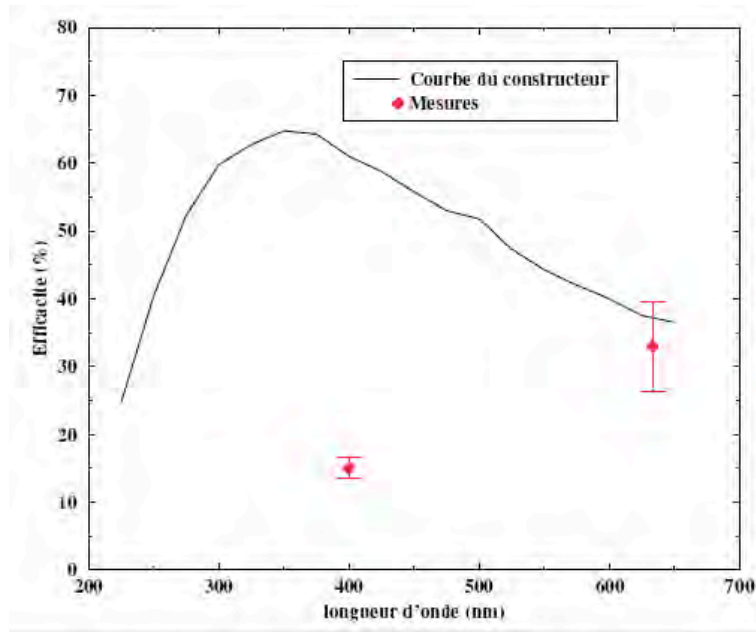


Fig. 5.7 Efficiency curve of the spectrometer between 225 and 650 nm. Uncertainty given by the manufacturer (black line) is known to 20%. The two red points are our measurements at 400 and 633 nm.

# Chapter 6

## Measurement of photomultipliers efficiencies

### 6.1 Principle of the measurement

Efficiency of detection during a measurement is defined like the ratio of the numbers of times where the phenomenon to be measured is observed to the number of times where it is produced. It is related to the apparatus geometrical configuration (solid angles), to the different attenuations (absorption in the air, presence of filters ) and to the quality of the measuring instrument.

The fluorescence measurement uses three photomultipliers. Like it was explained in the preceding chapter, two of them detect photons and work in single photoelectron mode, contrary to the third, which measures the spectrum of the  $\beta$  source. A good knowledge of the detection efficiency is not too critical for this last. In order to understand why, the following paragraph explains how PMT work of the and defines the efficiencies of each detector component. Then only, it is possible to imagine a measurement which allows to obtain the detection efficiency with precision.

#### 6.1.1 The Photomultiplier

##### **Operation of a photomultiplier**

The photomultiplier tube converts the photons it detects into a current of which the intensity is proportional to the luminous deposited power [Pho02]. If the light flux is continuous, the yield current will be also continuous. If the light is pulsed, the current will be pulsed. The internal time-constant is about 10 ns (the PMT works as a current source, thus with low impedance, and with low capacitances because the dynodes are distant them from each other). Any slower phenomenon will be then be well reproduced. The PMT schematic diagram is shown figure 6.1. Four parts can be distinguished:

- the photocathode, where the photoelectric emission takes place. The photo emissive material is evaporated on the internal transparent surface of the detector (transmissive photocathode);
- an electrostatic system focusing electrons on the first dynode;

- some ten dynodes, which amplify successively the signal by secondary emission. Like the photocathode, the dynodes can be semiconductor to maximize the secondary emission;
- the final anode, which gives the yield pulses.

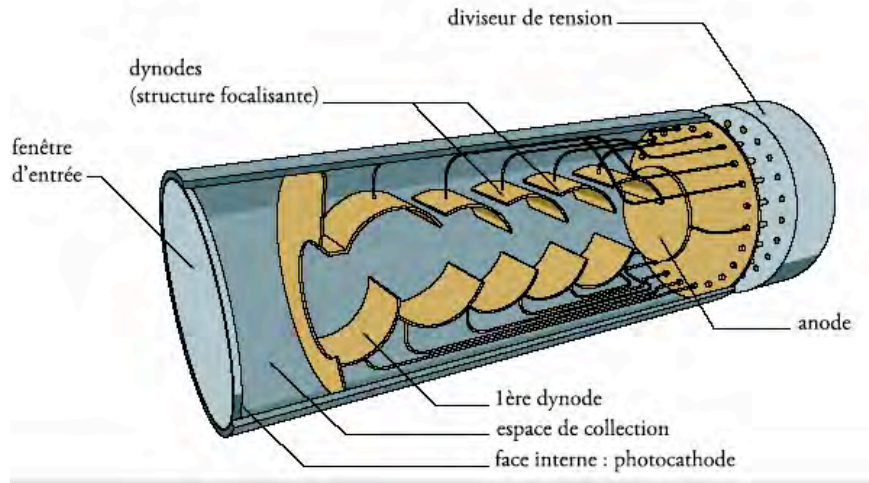


Fig. 6.1 Schematic representation of a photomultiplier tube.

The PMT and its power supply (voltage divider) are chosen specifically for the measurement to make: produce spectra, pulse speed, background noise, gain. The characteristics of the two PMT XP2020Q of Photonis used to detect the fluorescence photons are summarized in table 6.1.

### Definitions of the PMT efficiencies

Each step of the detection is characterized by an efficiency [Pho02, Pho99]:

- $\varepsilon_q$ , **the quantum efficiency** of the photocathode indicates its capacity to produce photoelectrons. It is defined by the ratio of the number of photoelectrons emitted by the photocathode to the number of incident photons  $N_{pe} / N_{ph}$ . One speaks also of the radiative sensitivity of the photocathode,  $S_k$ , given in  $\text{mA} \cdot \text{W}^{-1}$ . On one hand, the power  $P$  ( $W$ ) is proportional to the number of photons  $N_{ph}$  received per unit of time for  $P = N_{ph} \cdot hc / \lambda$ . On the other hand, the current  $I$  is proportional to the number of electrons  $N_{pe}$  by unit of time via the relation  $I = N_{pe}e$ . The radiative sensitivity is

$$S_k = \frac{I}{P} = \frac{N_{pe}e}{N_{ph} \frac{hc}{\lambda}} = \varepsilon_q \frac{\lambda e}{hc}$$

In practice,  $\varepsilon_q$  can be deduced from the measurement of  $S_k$

Fenêtre d'entrée	
Matériau	quartz (silice)
Photocathode	bi-alkaline
Intervalle spectral	150 - 650 nm
Sensibilité maximale à	420 nm
Indice de réfraction à 420 nm	1.48
Multiplicateur	
Structure	focalisante
Nombre de dynodes	12
Diviseur de tension type C	
Polarité	positive
Bruit de fond	30 et 300 coups/s
Rapport pic/vallée	2.5
Résolution	70 %
Temps de montée	1.6 ns
Gain pour HT = 2000 V	$3 \times 10^7$

Tab. 6.1 Summary of the characteristics of the photomultiplier tubes (PMT) XP2020Q used in the experiment.

- $\epsilon_{coll}$ , **the collection efficiency**, defined as the ratio of the number of photoelectrons reaching the useful surface of the first dynode to the total number of produced photoelectrons  $N_1 / N_{pe}$ . It depends on the high voltage applied to the PMT, because this one will define the shape of the electrostatic “funnel” attracting the photoelectrons towards the first dynode. We will see later how the product  $\epsilon_q \cdot \epsilon_{coll}$  varies in function of the position of the impact point of the photon on the photocathode.
- **The efficiencies of collection  $\eta_i$  and multiplication  $\delta_i$**  of the following dynodes.  $\delta_i$  is the number of electrons emitted by the dynode  $i$  per incident electron.  $\eta_i$  is the collection efficiency of the inter-dynode space following dynode  $i$ .  $\eta_i$  and  $\epsilon_{coll}$  depend on the voltage divider used for to feed the dynodes and thus on the high voltage applied to the PMT. In fact, the yield measurements will show that  $\eta_i$  is lower at high gain than at average gain.

These parameters make possible to define the gain  $G$  of a PMT like the ratio of a number of electrons reaching the anode to that of the photoelectrons:  $G = N_{anode} / N_{pe}$ . Introducing  $n_1$ , the number of electrons reaching the 1<sup>st</sup> dynode, one can write

$$G = \frac{N_1}{N_{pe}} \cdot \frac{N_{anode}}{N_1}$$

If the gain of dynode  $i$  is defined as like  $g_i = \eta_i \delta_i$ , one expresses  $G$  as efficiencies:

$$G = \varepsilon_{coll} \cdot \prod_{i=1}^N g_i$$

The quantities  $\varepsilon_q$  and  $G$  are not constants. They vary primarily in function of two parameters:

- **the position, on the photocathode, from where the photoelectrons are emitted.** The thickness of the photo emissive layer is not perfectly constant on the photocathode surface because of its mode of deposit (by evaporation or by flash) : the emission probability is thus function  $f(x, y)$ . Moreover, the dynodes position is not symmetrical with respect to the PMT axis. The collection of electrons will thus not be equally efficient on the cathode surface. This sensitivity is generally not given by the manufacturer: it is the case for the PMT employed in the fluorescence bench. The sensitivity cartography of the photocathode surface, made at the laboratory on the PMTs of the experiment, are detailed in the following section. It is a measurement of the PMT relative efficiency;
- **the wavelength.** The photocathode has its own spectrum of efficiency, i.e. it varies also with the wavelength of the incidental photons. Within the framework of fluorescence measurements, this dependence is weak for the studied spectral interval is relatively narrow (130 nm). Our measurement point is in this spectrum: the used LED emits light in near UV (wavelength with maximum of intensity 370 nm, spectral width of 12 nm).

The spectral photocathode sensitivity is given by Photonis with an relative error (from one wavelength to another) smaller than 1%, and this measurement is made with a calibrated light source. The absolute error is important: about 15 to 20%. It is effectively very difficult, and thus not precise, to control the number of photons emitted by a light source and also the variations of it: for that, the intensity as well as the angle and surface of emission have to be controlled to better than 1%, which is almost impossible. Moreover, the efficiency versus the position on the photocathode can vary up to 30%.

### 6.1.2 Use in the fluorescence bench

Within the framework of the Fluorescence bench, two luminous phenomena are measured:

- on one hand the scintillator light, excited by the source electrons;
- on the other hand, the production of a Fluorescence photon and its detection in one of the two arms.

The following paragraph explains the reason why the required precision on the measurement efficiency of each of these phenomena is not at all the same one.

## Electrons detection

The source emits isotropically electrons of energy varying between 0 and 2.28 MeV. Only the electrons touching the scintillator can be detected and the geometrical efficiency has to be taken into account. The number of photons emitted by the scintillator will be approximately 10 000 by MeV. The PMT “electrons” efficiency being about 20%, there will be on average 2000 photoelectrons per 1 MeV electron. The probability of detection is thus 1. The measuring accuracy is thus, in this case, independent of the precision with which one knows the PMT efficiency. It is thus useless of to measure the efficiency in single photoelectron mode of this PMT since it does not work in this mode.

In a general way, when a PMT receives a large quantity of light, i.e. when the number of photons is largely higher than 5 (for a detection efficiency of 20%), the photocathode will always emit several photoelectrons. It is not thus not necessary that the gain of the PMT is very high, since the signal is then already measurable. One says that the PMT works at “low gain”. We must, however, distinguish clearly the detection efficiency (here, 1) from efficiency of the PMT itself, which by definition is the ratio of the number is of photoelectrons emitted by the photocathode to the number of received photons.

## Detection of the fluorescence photons

Approximately 4 photons are created by electron and per traversed meter [Kakimoto+96], and they are isotropically emitted. There is thus approximately 0.2 photon per electron in the 4 cm window of the bench (see preceding chapter). The PMT-filter geometrical efficiency being  $3.689 \cdot 10^{-4}$ , the probability of detecting 2 photons is very low (of the order of  $10^{-8}$ ). As always, we must consider the geometrical efficiency (solid angles), the absorption and the reflection on the windows and lenses.

When a photon reaches the photocathode of the one of the 2 PMT, the detection efficiency of this single photon will depend on that of the PMT, i.e. of its faculty to transform it in a pulse of electrons, of a sufficient size to trigger a discriminator. In this case, contrary to the PMT “electrons”, the knowledge of the PMT efficiency is crucial. The measuring accuracy will be directly proportional to the precision with which this efficiency is known (the efficiencies, geometrical, of absorption and of reflections are easily appraisable to better than 1%).

One calls “high gain” mode, the detection by a PMT of individual photons in a very small number: it imposes a great gain  $G$ , i.e. to apply a very high voltage. The two PMT which detects the fluorescence photons work this way.

Photonis supplies its PMT efficiencies to within 15-20%. However, the precision desired by the cosmic rays physics requires that this uncertainty be brought back to less than 5%. Naturally, in order that the fluorescence measurement is absolute, the PMT efficiency must it also be absolute. The variation of absolute efficiency on the photocathode surface is largely higher than our limit of 5%. It is thus necessary of realize this cartography and to normalize it to the absolute measurement in a point of the photocathode. Many experiments were already confronted to this problem of efficiency determination. But in

the majority of the cases, it was a question of choosing a PMT rather than another one, and not to calibrate it. The most used methods of measurements of efficiency are detailed below. They are not applicable to the bench PMT calibration, because it has to be done in conditions all identical to those of the physics measurement.

### **Problems raised by the use of a calibrated light source in an efficiency measurement**

- **gain problems** ([Foord+69], [BirenbaumScar173], [LakesPoultney71], [Tub])

The direct measurement of the cathode current allows to determine the gain and the quantum efficiency separately. For the gain, we must also to measure the anode current of, since  $G = N_{anode} / N_{pe} = I_{anode} / I_{photocathode}$ . To be measurable and in order that the precision is sufficient, the cathode current must be at least a nanoampere. But in the case where the PMT should work at high gain ( $10^7$ ), the anode current will be too intense (10 mA) for the PMT to be still linear. The measurement will be wrong. For this reason, it is usual to make the detector work like a photodiode, i.e. only the cathode and the first two dynodes are put under voltage to have a normal electric field in the collection space. One can then measure the cathode current directly.

This two steps measurement requires to vary the light source intensity by several orders of magnitude. It is very difficult to preserve a good precision of absolute flux during such a variation.

One can also notice that, as with high gain, if one decreases the photon flux, one will not remain in continuous mode. At a moment, one will be in single photoelectron mode: the PMT will detect the photons independently one from each other.

- **problems involved in the use of a calibrated light source** ([BirenbaumScar173], [Tub], [Besson+94])

Knowing the number of photons sent on the PMT, it is easy to deduce its quantum efficiency: according to the flux, it is sufficient to count the number of photoelectrons which triggered a discriminator or to measure the cathode current. Different types of light sources can be calibrated in an absolute way to this end (lasers, lamps, LEDs). One has the power spectrum of the source  $d^3P / dSd\lambda d\Omega$ . Although the principle is very simple, the implementation is very delicate because of the source flux fluctuations with the temperature or in the course of time (and, as explained higher, the surface of emission, the solid angle and the flux have to be controlled). These fluctuations are difficult to control precisely.

The main problem lies in the numerical opening of the source, because the precise solid angle in which it emits its photons is most often badly known. In effect, it is almost impossible to obtain a light source without lobes, which will be the cause of the bad quality of measurement if the solid angle is not wide enough [BirenbaumScar173], [Tub]. To mitigate this effect, the source can be calibrated only in the central part of the luminous spot [Besson +94]. In short, the PMT measured this way have efficiencies known to within 10-15%.

## Comparison of light flux detected by the PMT and a calibrated detector (NIST) ([Biller+99])

This method frees from the problems of light source intensity variation. It consists in measuring simultaneously the fluxes received by the PMT and a photodiode calibrated in an absolute way (NIST, NPL, CNAM ). Simultaneous measurement of the fluxes is done most of the time with a separating parallel plate. The main difficulty is due to the fact that the gain of the photodiode NIST is 1 at maximum, whereas that of the PMT can be higher than  $10^7$ . And the efficiencies of the detectors must absolutely be measured with high gain, because they vary with the gain: electrons collection in the PMT modified with the electrostatics, therefore with the inter-dynode voltage, and finally with the gain [Lavoute].

Another type of flux divider, used by the SNO experiment to calibrate their PMTs, is described in [Biller+99]. It uses an integrating sphere, which is explained in details in chapter 6.3. The diagram of the set-up is reproduced in figure 6.2.

A monochromatic beam is focalized in an integrating sphere having a port of entry and two ports of exit. The sphere is used to create a stable and non-polarized light source. Its spectral radiant intensity is measured permanently by a calibrated photodiode (“Monitor Photodiode” on diagram 6.2). The unit {source + sphere + photodiode} is similar to a source calibrated in intensity (and intensity only), with the difference that this source is constantly calibrated. It thus is a very important progress compared with the preceding methods, which accept one definitive calibration, without taking into account any possible later variations.

The other exit port is directed towards a dark box in which is placed the PMT to be tested. Regularly during measurement, a second photodiode is inserted between the sphere and the PMT to control the absolute flux value (“Reference Photodiode” on diagram 6.2). In spite of its ambition, this assembly does not solve the problem which consists in measuring in an absolute way the efficiency of a PMT, and this for two reasons:

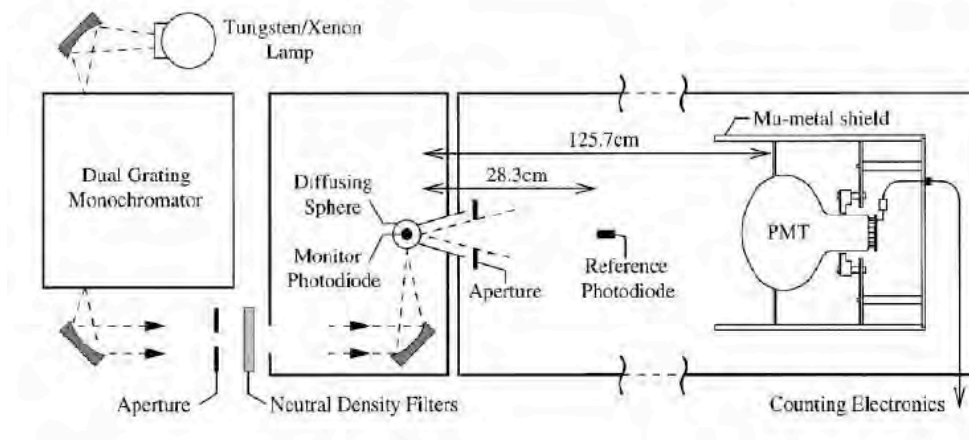


Fig. 6.2 – Set-up of a controlled source for PMT calibration [Biller+99]

- The flux at the exit of the sphere is lambertian, that is proportional to  $\cos \theta$ . The PMT is thus not uniformly illuminated, which is necessary if one wants to measure its efficiency on all the photocathode.
- The gain difference prevents from placing the reference photodiode at the same distance from the sphere that the PMT. The flux received by the PMT is thus not measured directly, but deduced from the measurement with the photodiode.

In spite of the progress this set-up represents, it finds its limitation here: none of two photodiodes do control the flux *effectively* received by the PMT.

### **PMT calibration method developed for fluorescence measurement**

Finally, the “ideal” calibration which we propose is very close to that which proposed [Biller+99]. In particular, the constant sphere flux control allows to decrease the systematic error on the source calibration. But it allows, on top, a control of the intensity variations, and to get rid of the problems of luminous distribution. If one wants to calibrate the PMT at high gain with a precision better than 5%, two improvements are essential:

- For the calibration of the PMT, the intensity control of the source alone is not sufficient. The set-up shown in figure 6.2 does not allow to measure precisely the PMT flux. We have thus to imagine a system which allows to attenuate the light intensity in a stable and repetitive way by a factor of approximately  $10^7$  to be able to use the two instruments *at the same time*. One gets rid thus completely of the light source flux variations. The use of neutrals filters does not solve either the flux attenuation problem, because the response of an association of such filters is not known to better than approximately 10% (effects of reflection, diffusion ). The filters thus cannot be the solution to obtain a precise result.
- As this attenuation is itself a source of systematic error, it is necessary to calibrate it too. For that, it the idea is to replace the PMT by the reference photodiode, i.e. to place the latter exactly at the same distance from the sphere center and to use the same opening than for the PMT. This way, the intensity and possible lobes are identical for two measurements.

This set-up which answers these two requirements was designed and realized at the laboratory. It is presented in the third part of this chapter. One integrating sphere is not enough to attenuate the light intensity sufficiently, and [Biller+99] recognizes this fact and does not allow to put the photodiode at the same place that the PMT. In other words, with only one sphere, the ratio of the detecting surfaces of two photodiodes (photodiode of measurement:  $1 \text{ mm}^2$  and photodiode of control:  $100 \text{ mm}^2$ ) is only 1/100, very far from the necessary  $10^{-7}$ . Instead of one, it will be thus two spheres which, joined, allow on one hand to attenuate the flux of a stable and measurable quantity, and, on the other hand to be able to make the PMT and photodiode work simultaneously in spite of difference of gains. One will use the ratio of the surfaces of the spheres and of the surfaces of the diaphragms (between the spheres and in front of the PMT).

### 6.1.3 Conclusion

The absolute calibration of our two photon-PMT thus has been realized into two steps. First of all, the cartography of the detection surface yields a relative efficiency. It is carried out by moving the end of optical fiber in front of the photocathode, perpendicular to it. This will be described in the following part. Then, the comparison of luminous flux measured by a calibrated photodiode and of the number of photoelectrons in the PMT fixes the scale of the relative calibration: it makes the measurement absolute. This comparison is made for only one position (x, y) on the photocathode. It is described in the third part.

One must here specify the conditions in which the efficiencies were measured for each PMT. The photocathode of the PMT-JY is remained “naked” (no coating whatsoever), since it receives directly the photons leaving the spectrometer. The efficiency of the PMT-filter was measured with the filter optically glued to the center of photocathode, since it is in this condition that this PMT is used to measure the fluorescence yield. The non filtered part of the photocathode was made opaque to the light.

Although the calibration was necessary at the gain of single photoelectron, it also was carried out at low gain in order to validate this new method. Set-up and measurement results can be looked at in appendix C.

## 6.2 Cartographies of the Photomultipliers Photocathodes

The efficiency given by Photonis is for a certain type of photocathode and at a point of its surface. One does not know neither this position nor the surface. It does not take into account the photocathode dimension, neither the possible efficiency variations of on this surface, neither the edge effects (the variation scale of the order of a few millimeters). Moreover, in our application, the detection surfaces are not the same: only a vertical central rectangle of 18 x 10 mm of the PMT-JY photocathode is used to detect the photons, while the PMT-filter is covered with a 34 mm diameter filter (the remainder being blackened). But to succeed in lighting such surfaces cannot make possible to reach the wanted precision, because no light source really emits light in a really uniform way.

It is thus essential of make an efficiency measurement “point by point”, on small size surfaces, to be able to then calculate the effective average efficiency, i.e. taking account of the effective detection surface. This of course implies to be under conditions identical to those of the experiment, i.e. at high gain. Let us recall that the efficiency varies with the gain.

### 6.2.1 Description

#### **The black box.**

The set-up is installed in a box of approximately 1 m<sup>3</sup> whose internal walls are painted in mate black. Tightness to the external light is ensured by baffles and not by joints. One avoids then light leaks of and in the long run, leaks due to the ageing of the joints. The baffles are a simple mechanical system who prevents the photons from passing thanks to successive obstacles (it is the system used in photo cameras). This box is provided with a absolute safety lock preventing to open it if the PMT HV is on: the external SHV connector blocks the opening mechanism. As a matter of fact, only one mistake on a few hundreds openings (necessary to fulfill the efficiency measurement) would be enough to destroy the PMT.

#### **XY movement.**

In this box, one fixes the PMT to be surface calibrated to a XY table (5 x 5 cm displacements with a theoretical precision of 1 μm, approximately 5 μm in reality). An electroluminescent diode (LED RLT370-10 of the company Roithner Lasertechnik) feeding light to two identical optical fibers is fixed on this table. The LED emits in the near ultraviolet, with a peak at 377 nm (see its spectrum figure 6.4). It is seen that the full width

half maximum is 12 nm. Knowing that the spectrometer has a FWHM of 6 nm (when it is lit by a laser), one deduces from it that the width of the LED is of 10 Nm.

These fibers are made out of quartz clad with plastic. They have a diameter of 200  $\mu\text{m}$ . Their numerical opening was measured by projecting light emitted by a fiber on a screen (a red laser was feeding the fiber). Measuring the diameter of the luminous spot  $D$  and the distance between the fiber end and the screen  $L$ , one deduces the numerical aperture  $NA$ :

$$NA = \sin(\alpha)$$

with

$$\alpha = \tan^{-1}\left(\frac{D/2}{L}\right)$$

The numerical aperture of these fibers is  $NA = 0.22$

One of the two fibers (the moving one) has its end at 2 mm of the photocathode, perpendicularly to it. The light spot has then a 1.5 mm diameter, which is smaller to the distance necessary for the efficiency to vary more than a few percent.

### Photodiode NIST.

The end of the other fiber is in front of a NIST (National Institute of Standards)

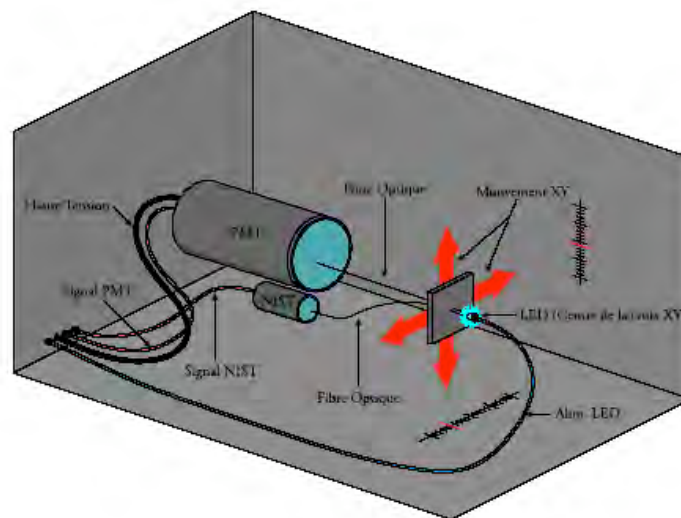


Fig. 6.3 Schematic representation of the PMT and a photodiode illuminations in the black box. The LED is fixed on a X-Y movement controlled from outside. It illuminates two optical fibers, one towards each detector. One makes sure naturally that the light of the LED itself arrives neither at the PMT nor to the photodiode.

photodiode. This one is calibrated in an absolute and precise way on a broad spectral range. The photodiode used for the cartography is a UDT S370, which has a calibration precision to  $1 \sigma$  of 1.5%. Its efficiency curve is represented figure 6.5. At 370 nm, it generates a current of 0.147 na per nW received as photons. The nanoammeter used with the UDT also contains its calibration, so that one can read directly the received power  $P$  after having displayed the wavelength. To return to the number of photons per unit of time  $N$ , it is sufficient to know their wavelength since  $P = N \cdot hc / \lambda$ .

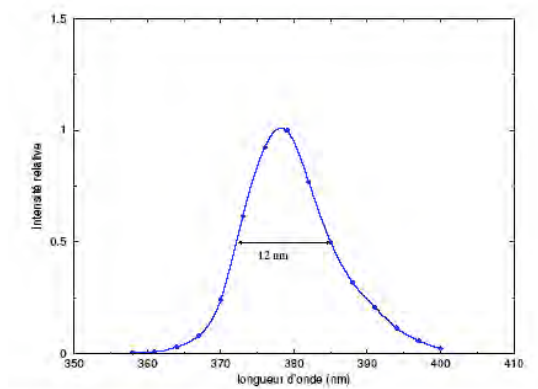


Fig. 6.4 Spectrum of relative intensity of LED RLT370-10 used for the calibration, measured with the spectrometer. The entry and exit slits are opened to 2 mm and contribute for 6 nm to the observed width. The real width of the LED is thus 10 nm.

As the LED temperature varies rather quickly, it does not send always the same number of photons in the fibers. One can get rid of these flux variations by normalizing the measurements with the power received by another NIST photodiode (Ophir Optronics PD300-UV-SH) at the same time.

### Protocol.

The protocol adopted to carry out the measurements is the same one for each PMT:

1. Once the PMT placed in front of the moving fiber, its gain is set. Then one leaves the PMT under voltage during several hours (on average a night) so that its gain and darkness current stabilize;
2. One seeks the position of the center of the photocathode with the XY movement by going from one extremity to the other;
3. One carries out the cartography at this gain.

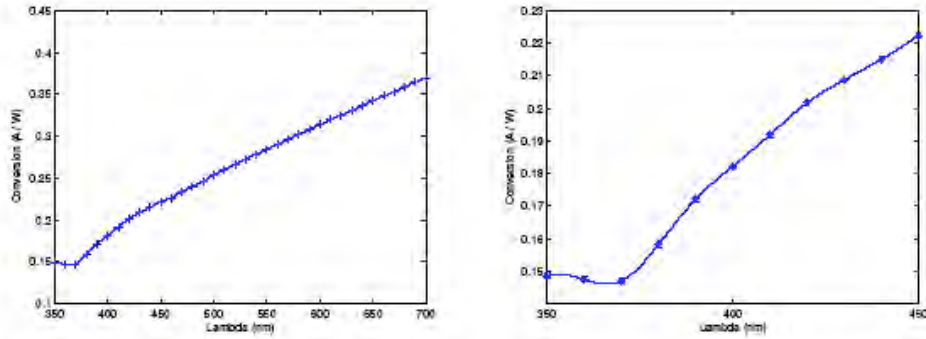


Fig. 6.5 Curve of absolute efficiency of the calibrated photodiode UDT S370: on the left, on most part of the ultraviolet and visible spectrum. On the right, a blow up on the ultraviolet range of the wavelength. This curve is absolute for it gives the emitted current versus the received luminous power.

**Precautions.**

The distance between two neighboring measurements, which will be called the measurement step has to be decided. This one must be slightly higher than the size of the spot of light on the photocathode. On the other hand, it should not be too large (superior to 5 mm): the photocathode efficiency varies approximately every 5 mm, due to the evaporation process and shape of the electrostatic “funnel” towards the first dynode. Finally, the selected step is 3 mm.

**Tube orientation**

Last, the PMT orientation has to be taken care of, because the dynodes do not have axial symmetry and the terrestrial magnetic field influences the electrons trajectories. This is an important effect, of some 10% for the efficiency if the tube is not  $\mu$ metal shielded. Our tubes are  $\mu$ metal shielded, but as it is the case for most applications, not perfectly: the end of the  $\mu$ metal shield is at the photocathode, instead of extending by two tube diameters as recommended: there was no room for that. So the result is that the tube response varies by 2-3% when it is  $2\pi$  rotated. To take care of that effect, we make an azimuthal mark (the HV connector is up!) and keep the tube that way in all our measurements.

We will see later, in the chapter devoted to the absolute efficiency, that we have to take into account the orientation of the tube with respect to earth.

**6.2.2 Determination of the center of the photocathode.**

The fiber is placed with the naked eye at the central area of the PMT. Two successive measurements are enough to find the position of the photocathode center with a sufficient precision. A first horizontal sweep every 3 mm produce one profile of efficiency. The FWHM of the efficiency profile is equal to the detection surface diameter (34 mm for

PMT-filter, 51 mm for the PMT-JY). The middle of this curve is thus regarded as the X-coordinate of the photocathode center. With this position, a second sweep, vertical, yields the Y-coordinate of the center of the photocathode. The (0-0) position of the photocathode center is hence determined.

Measurements of efficiency itself allow to check the found position: the cartography of a photocathode is a collection of profiles (horizontal or vertical) separated by 3 mm. In order for the position (0, 0) to be confirmed exact, the center must thus be the same one on all the curves. Effectively, the error made is about 0.2 mm. Figures 6.6 and 6.7 show an example of these horizontal profiles for each photomultiplier.

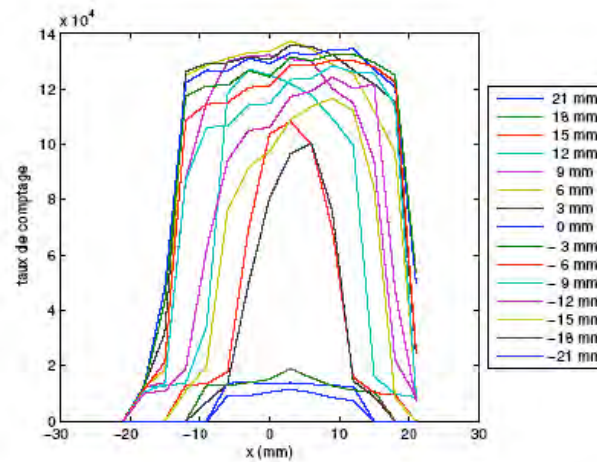


Fig. 6.6 Profiles of the response of PMT-filter at low gain taken along the horizontal axis, to check the photocathode center position. This position is used then to give an origin to the cartography. Each curve corresponds to an different ordinate on the photocathode. The more central profiles ( $-6 \text{ mm} < y < 6 \text{ mm}$ ) have a FWHM compatible with the diameter of the BG3filter, 34 mm. The x and y axis are only measurement conventions: they quite naturally define the horizontal and vertical directions.

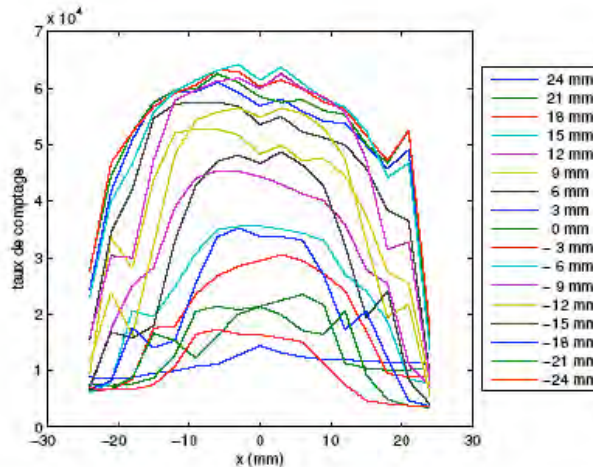


Fig. 6.7 Response curves of the PMT-JY taken along the horizontal axis at low gain. One already sees that the edges are less stiff than those of the PMT-filter.

### 6.2.3 Cartography at high gain

To be in single photoelectron mode, one lowers the light level with using the “LED Driver” and compensates the response by increasing the PMT high voltage. The chosen gain, about  $10^7$ , corresponds to a high voltage of 2176 V for PMT-filter and 2325 V for the PMT-JY. The set-up is represented schematically on figure 6.8. If the coincidence between the pulse generator and the discriminator (set between the “0” and the “1”) yield let pass only signal A (coincidence OFF), the ADC spectrum has two peaks, the “0” and the “1”. If coincidence is A and B, one selects only the “true” events and the spectrum contains only the peak “1 photoelectron”.

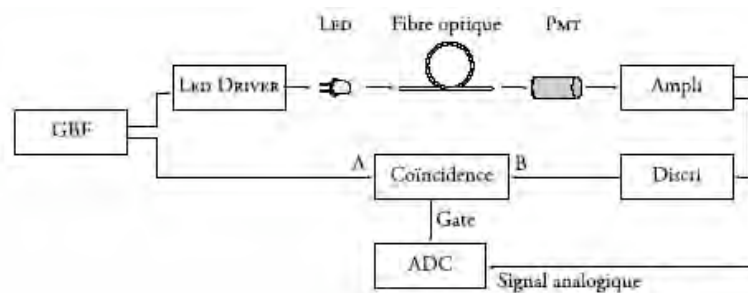


Fig. 6.8. Single photoelectron DAQ for the high gain PMT mapping

As the light level has dropped a lot, as well as the generator rate (10 kHz), a temporal coincidence selects the “1 photoelectron” events. There is coincidence when the PMT produces a pulse which triggers a discriminator while the LED is lit. The normalization is made with the UDT photodiode. For that, the GBF frequency must be temporarily raised to 1 MHz in order to increase the quantity of emitted light and to decrease the reading

uncertainty on the photodiode. Utility of such control by a calibrated detector is proven when one finds out that the light of the LED detected by the photodiode varied from 3.7% for PMT-filter and 10% for the PMT-JY during the cartographies. In fact, a control of how much the LED varied is made every 5 minutes. As the cartography is only a relative measurement, this control is sufficient.

Figures 6.10 to 6.13 show the responses of the photocathodes of each PMT.

## 6.2.4 Conclusion

The photocathode center is not mandatorily the place where efficiency is highest. Important differences of shape appear from one PMT to another. The analysis of the charts shows that only the central area is usable if the wanted precision is about 1%. Beyond, the variations are too important. One will see (figure 6.21) that the efficiency decreases quickly when the detector effective surface is increased starting from the center.

Following this measurement, a black diaphragm of 20 mm diameter was fixed on the PMT-filter to measure the fluorescence, because it was impossible to keep enough precision with the full filter surface. This operation is not necessary for the PMT-JY, because the luminous spot on the photocathode, at the exit of the spectrometer, has only a surface of approximately 200 mm<sup>2</sup>.

The small bump which one observes on the side of the topography of the PMT-JY chart (region of X-coordinate -3 mm to 3 mm and of Y-coordinate 20 mm) is explained by taking account of the mode of deposit of the photo emissive layer (by evaporation). This one does not only settle on the internal surface of the PMT window, but also along the glass cylinder on a few millimeters. In other words, the edge of the window acts like a prism, and a little more photons are recovered on the higher edge of the tube of glass (see the diagram of figure 6.9).

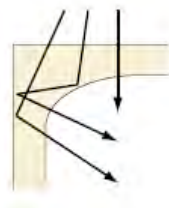


Fig. 6.9 The unexpected increase in the photocathode efficiency of the PMT-JY is due to the presence of the photo emissive layer on a few millimeters along the glass cylinder.

The efficiency of our two PMT was measured on about 200 positions on the photocathode. This relative measurement is precise, because we could take account of the temporal flux variations of the LED.

The next part explains how, by comparing the fluxes measured by a photodiode and a PMT (at a given position on the photocathode), we could make absolute our relative charts.

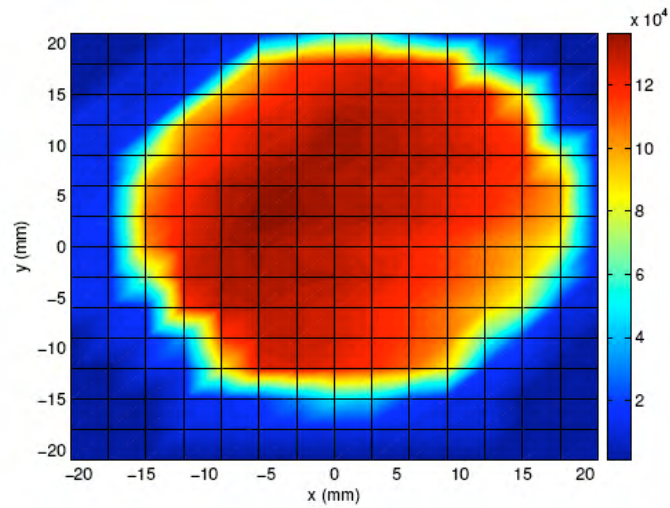


Fig. 6.10 Topography of PMT-filter at high gain, normalized to the luminous power received by the photodiode.

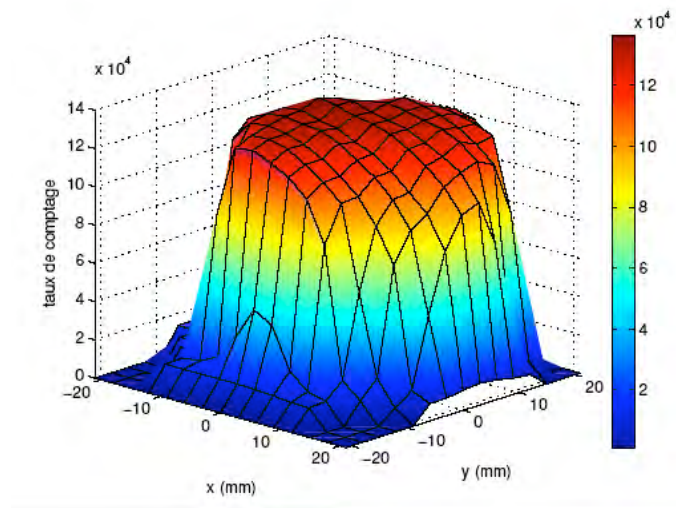


Fig. 6.11 Topography in 3D of PMT-filter at high gain, normalized to the luminous power received by the photodiode.

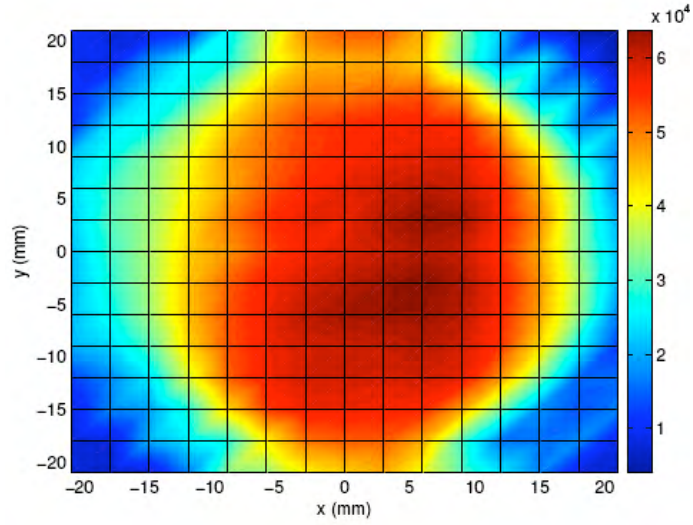


Fig. 6.12 Topography of PMT-JY at high gain, normalized to the luminous power received by the photodiode.

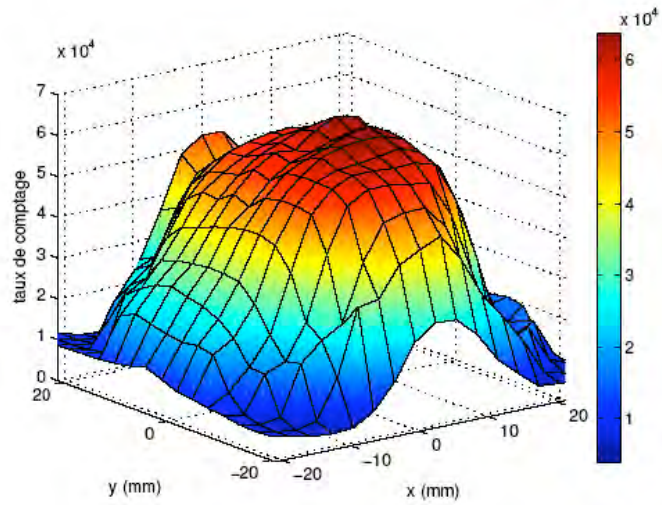


Fig. 6.13 Topography in 3D of PMT-JY at high gain, normalized to the luminous power received by the photodiode.

## 6.3 Absolute Yield in a Point of the Photocathode

The yield of each PMT at a point of the photocathode relative to another one is now known with precision. In order for the PMT characterization to be complete, one must determine the ratio of effectively detected photons to the number of emitted photons. This quantity is the absolute yield of the photomultiplier.

As seen earlier, to measure the absolute yield, one can theoretically use either a calibrated source, either compare the measurement to a calibrated detector. The first solution supposes that source emits a quantity of photons known and stable so that one can use this number in the calculation of the yield. This method is not applicable to a measurement more precise than 10%, primarily because of the lobes.

It is thus a question now of finding a set-up which allows at the same time:

- to compare the number of photons emitted towards the PMT to the number of effectively detected photons,
- to make this comparison simultaneously in order to get completely rid of the flux variations,
- to compensate for the incompatibility of the photodiodes gains with respect to the PMT.

This chapter describes the method which reaches these objectives. simultaneous operation of a photodiode and a PMT, i.e. the division of the luminous flux by a  $10^7$  factor in a stable and repetitive way, is ensured by integrating spheres, whose principle is described in the following part. This makes the originality of this set-up.

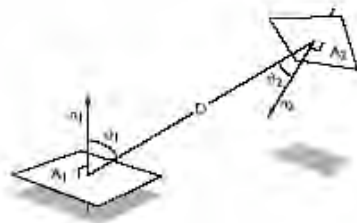
### 6.3.1 Operation of the integrating spheres

#### **Principle**

An integrating sphere is a hollow sphere whose wall is coated with a light diffuser (the grain of the diffusion must agree with the wavelengths of the photons to be studied). It is used to collect an external electromagnetic flux, generally with the goal of measuring it or of attenuating it. After a sufficient number of reflections on the walls, the internal electromagnetic radiation is completely uniformized, and its intensity is directly proportional to that of incidental flux [Lab].

The principle of operation of an integrating sphere is described by a simple equation which expresses the energy transfer between two diffusing surfaces, one transmitting, the other one receiving.

In a general way, one considers two surface elements  $dA_1$  and  $dA_2$



The flux fraction emitted by  $dA_1$  which reaches  $dA_2$  is written:

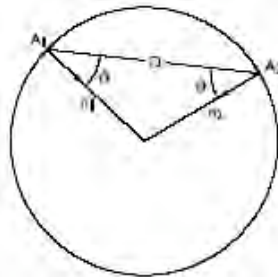
$$d\mathcal{F} = \frac{\cos \theta_1 \cdot \cos \theta_2}{\pi D^2} dA_2$$

$\theta_1$  and  $\theta_2$  are measured relative to the perpendicular of each surface element, and  $D$  is the distance between  $dA_1$  and  $dA_2$ . In the case of a sphere,  $dA_1$  and  $dA_2$  are located on the internal wall. In this case,  $\theta_1 = \theta_2 = \theta$ , and  $D = 2R \cos \theta$ . One has then:

$$d\mathcal{F} = \frac{\cos \theta_1 \cdot \cos \theta_2}{\pi D^2} dA_2$$

that is to say

$$d\mathcal{F} = \frac{dA_2}{4\pi R^2} = \frac{dA_2}{A_{\text{sphere}}}$$



This result is remarkable insofar as it is independent of the view angle between the surfaces, of the distance which separates them and of the size of the emitting part  $A_1$ . The spherical shape thus not only allows an important theoretical simplification but also very practical since the only parameters which enter into account are the surfaces of the sphere and of the exit port of the flux.

A flux  $\Phi_i$  thus reaches the surface  $A_2$ , on which it is reflected. After the reflection, the flux is expressed in function of the reflectivity of the wall,  $\rho$ , and of the surface towards which it is reflected,  $A_{\text{eff}}$ :

$$\Phi_r = \Phi_{in} \rho \frac{A_{eff}}{A_{sphere}}$$

Finally, if the sphere has  $m$  ports, then the efficient surface  $A_{eff}$  is worth

$$A_{eff} = A_{sphere} - \sum_{i=1}^m A_i$$

The experimentalist must thus optimize the entry and exit surfaces of the flux to maximize the reflected flux. One considers generally that the advantage of a high reflectivity is lost when the openings occupy more than 5% of the sphere total surface. The assembly described in this chapter complies with this rule.

### Calibration of the PMT with the integrating spheres

The two spheres used for this measurement are made by LabSphere. They are identical, with a diameter of 4 in. each (10.16 cm) and three ports located at  $90^\circ$  from each other. Two of the ports have a diameter of 1 in. (2.54 cm) and one of 1.5 in. (3.81 cm). The reflecting material coating their internal wall is SpectraFlect<sup>®</sup>, optimized for a use in the visible and the close ultraviolet light. Between 300 and 400 nm, its reflectivity varies between 0.94 and 0.98. Because of the great number of reflections to which are the photons subjected in a sphere, there will be a considerable attenuation. But we do not need to know this attenuation: it is enough to know that it is constant.

The largest port is used as entrance point of the light, the two others for the measurements. Table 6.2 gathers the numerical values of the surfaces which will enter in account in the calculations:

Surfaces	
totale, $A_{sphere}$	324.29 cm <sup>2</sup>
du port de 1.5 in, $A_{1.5}$	11.40 cm <sup>2</sup>
de chaque port de 1 in, $A_1$	3.99 cm <sup>2</sup>
effective, $A_{eff}$	304.91 cm <sup>2</sup>
déetectrice de la photodiode, $A_{MDI}$	0.78 cm <sup>2</sup>

Tab. 6.2 Summary of the surfaces intervening in the efficiencies calculations of the spheres. They are only given here as an indication: it is much more precise to measure the ratios than to calculate them.

The adopted method is identical for the two gains. Prior to any yield measurement, the necessary diaphragms dimensions have to be determined, and a suitable measurement be done. Then only, the PMT can be assembled on a sphere. Stability of the luminous flux inside the sphere must constantly be controlled by a photodiode, the same one which was used to calibrate the system.

## 6.3.2 Efficiency at high gain

### Optimization of the assembly

To know the size of the diaphragms to be set in front of the photodiode and the PMT, one has to give an estimate of the division of flux necessary between these elements. The reflections in the materials which surround the photodiode detecting surface could lead to an over-estimate of the real flux on  $A_{UDT}$ . One circular diaphragm, 9 mm in diameter, is thus fixed on this photodiode. The flux who reaches the photodiode is written

$$\Phi_{UDT} = \Phi_{sphere} \frac{A_{UDT}}{A_{eff}}$$

and that which reaches the PMT,

$$\Phi_{PMT} = \Phi_{sphere} \frac{\pi r^2}{A_{eff}}$$

where R is the radius of the diaphragm which one seeks. The ratio of luminous flux is thus

$$\frac{\Phi_{UDT}}{\Phi_{PMT}} = \frac{A_{UDT}}{\pi r^2}$$

that is to say

$$\frac{\Phi_{UDT}}{\Phi_{PMT}} = \frac{r_{UDT}}{r^2} = \frac{0.25(cm^2)}{r^2}$$

However, the photodiode has a background noise of about 2 pA. For the measurement to be precise, it is mandatory to remain constantly at least to 2 nA, i.e. the photodiode must receive about  $2.6 \cdot 10^{10}$  photons per second. On the PMT side, one estimates that the single photoelectron spectra are clean when there is a maximum of one photoelectron for 50 pulses. At a rate of 100 kHz, this corresponds to  $10^4$  photons per second. The set-up thus must be able to divide the luminous flux by a factor of  $2.6 \cdot 10^6$  which, as shows the formula of the flux ratio, is impossible with only one sphere: R should be  $3 \cdot 10^{-4}$  cm!

To add a sphere allows to add a diaphragm. An additional term goes in the preceding equations, the flux in the second sphere:

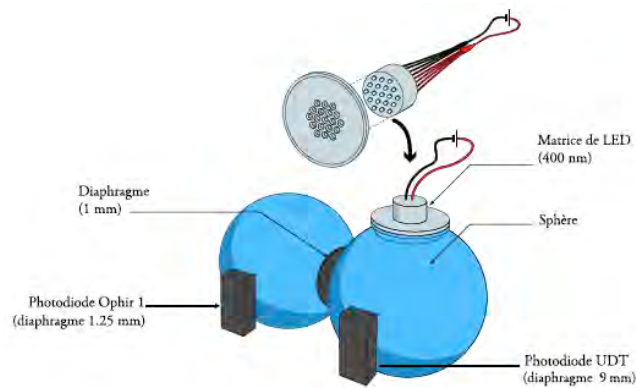
$$\Phi_2 = \Phi_1 \frac{\pi r^2}{A_{1eff}}$$

One considers for the moment that the diaphragms between the spheres and in front of the PMT are identical. The ratio of the fluxes is this time:

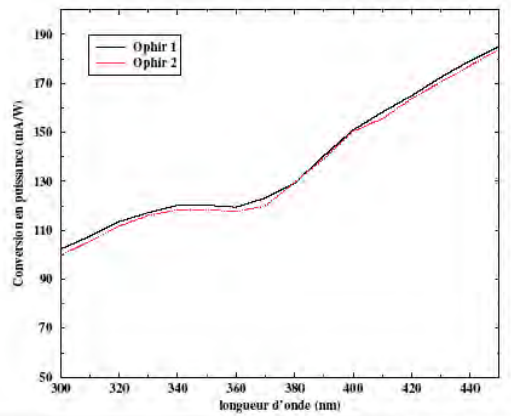
$$\frac{\Phi_{UDT}}{\Phi_{PMT}} = \frac{A_{UDT} \cdot A_{2eff}}{(\pi r^2)^2}$$

With this calculation, one finds that the two diaphragms must have a maximum radius of 1 mm. When measuring, we observed that the “0”/“1” ratio was largely higher than 50, and that one thus lost time with doing the measurements. By replacing the 1 mm diaphragm by a 1.25 mm one in front of the PMT, the good ratio was obtained.

The check of the fluxes ratio is made by setting another photodiode at the place the PMT will occupy, as shown on scheme 6.14. This way, it is possible to read simultaneously the fluxes received in each sphere and behind each diaphragm. The second photodiode is by manufacturer Ophir, and will be noted Ophir 1 not to mistake it with another photodiode of same manufacturer, Ophir 2, which will be used later on. Its calibration precision to  $1\sigma$  is also 1.5% [Laser2000]. The calibration curves of these two photodiodes are represented on figure 6.15.



6.14 Diagram of the set-up for the division of luminous flux between the two detectors with two integral spheres.



6.15 Curves of absolute calibration of the two Ophir photodiodes between 300 and 450 nm. The precision on these numbers is 1.5%.

## Measurement of the light flux ratio

The photodiode has to be sufficiently illuminated, in order that the precision of reading the received flux is sufficient, the light sent in the first sphere must be very powerful. One thus use 12 mW LEDs of (ETG-3UV400-30), presenting a maximum of emission at 400 nm, in the place of the LED of 377 Nm, whose power is only 0.75 mW. Their spectrum is represented on figure 6.17. 19 of these LED are connected in parallel, with a resistance of 100  $\Omega$  in series on each one. (see photo 6.16). This matrix of LED is fixed on an aluminum plate to dissipate the heat and to maintain them together. They fill a circle of 25 mm in diameter. Taking into account the resistances, the maximum voltage applicable is 4.9 V.

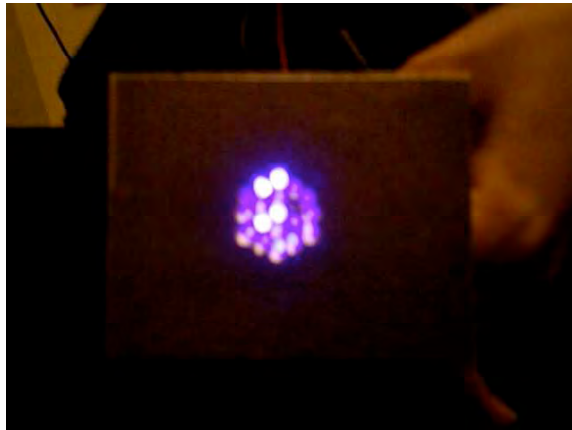


Fig. 6.16 Matrix of Leds.

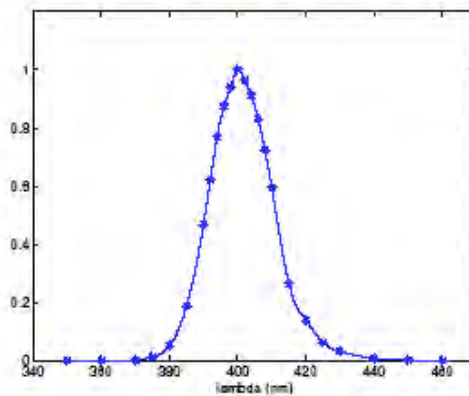


Fig. 6.17 Intensity curve of a LED ETG-3UV400-30 versus wavelength. These LED have a power of 12 mW, which allows a stronger illumination. This is necessary to measure the yield of the two spheres. The spectrum is normalized to the highest intensity. It was obtained by measuring the light intensity of the LED matrix with the spectrometer, whose slits were opened to the maximum (2 mm).

Table 6.3 gathers the results of the flux ratio measurement of each sphere. The received current is read with the optometer (the pico-ammeter used with the UDT photodiode). The calibration of the photodiodes allows to convert the currents into powers for a given

wavelength, here 400 nm. The power being proportional to the number of photons, the ratio of the powers is quite equal to the ratio of the numbers of photons received by each detector.

As one can note it thanks to the reading precision shown in table 6.3, the currents are very stable. The total error of this measurement can be written:

$$\frac{\Delta R}{R} = \frac{\Delta I_{udt}}{I_{udt}} + \frac{\Delta \alpha_{udt}}{\alpha_{udt}} + \frac{\Delta I_{ophir1}}{I_{ophir1}} + \frac{\Delta \alpha_{ophir1}}{\alpha_{ophir1}}$$

with:

$$\begin{aligned} \frac{\Delta I_{udt}}{I_{udt}} &= 0.03 \% \\ \frac{\Delta I_{ophir1}}{I_{ophir1}} &= 0.5 \% \\ \frac{\Delta \alpha_{udt}}{\alpha_{udt}} &= 1.5 \% \\ \frac{\Delta \alpha_{ophir1}}{\alpha_{ophir1}} &= 1.5 \% \end{aligned}$$

One will finally retain an error of 3.1% on this measurement.

	UDT (Sphère 1)	Ophir 1 (Sphère 2)
Courant lu	63.39 $\mu\text{A}$	21.8 pA
Puissance à 400 nm	347.91 $\mu\text{W}$	143.89 pW
Précision de lecture	< 0.02 $\mu\text{A}$ (0.03 %)	< 0.1 pA (0.5 %)

Tab. 6.3 Currents measured by each photodiode to calibrate the flux divider represented by the coupling of the two spheres.

Finally, the flux ratio is:

$$\boxed{R = (2.42 \pm 0.07) \cdot 10^6}$$

### Measurement of the PMT efficiency

To measure the absolute efficiency of a PMT at a point of the photocathode, we replace the photodiode of the second sphere (here, the photodiode Ophir 1) by the PMT, keeping the 1.25 mm diaphragm (see the diagram of figure 6.18). Three essential precautions must be taken before starting the measurements:

1. As the luminous flux leaving the sphere is not measured as such (especially its shape), the detecting surface (photocathode for PMT-JY or BG3 filter for the PMT-filter) must be exactly at the same distance from the center of the sphere that it was for the photodiode. The part which allows the fixation of one or the other of these detectors on the sphere was designed to this end. With the back, the PMT is maintained into touching that part by springs. Keeping both detectors at the same distance, and keeping the same diaphragm, allows also to be sure that the spatial distribution of the light is quite identical for both measurements.

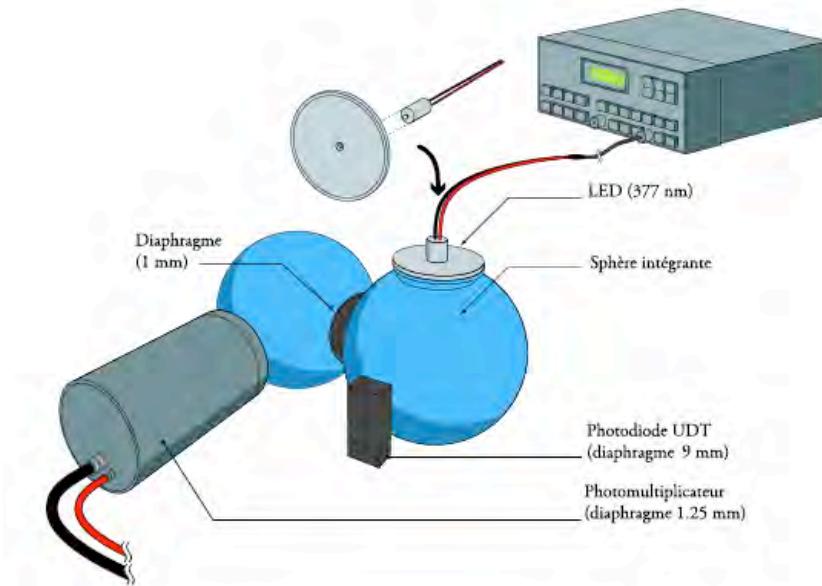


Fig. 6.18 Set-up of the absolute efficiency measurement of the PMT at high gain. The second photodiode was replaced by the PMT to calibrate. To decrease the quantity of light, the matrix of 19 LEDs has been replaced by a single LED.

2. The internal structure of the PMT of this experiment is not symmetrical. Moreover, the terrestrial magnetic field has a large influence on the collection efficiencies, by modifying the electrons trajectories. While turning the PMT equipped with their  $\mu$ -metal, one observes a maximum variation of 2%, that is to say a one  $\sigma$  of approximately 0.5%. Nevertheless, the azimuthal  $\Phi$  orientation (important for orientation of the photocathode and for the collection of electrons between the photocathode and the first dynode) which had been selected during the cartography is preserved for the measurement of the absolute yield. The  $\theta$  angle relative to the North, important for the electron trajectories from dynode to dynode which has been taken for the PMT absolute calibration will be kept for the fluorescence yield measurement.
3. Finally, the photocathodes were mapped every 3 mm, dividing the surfaces in pixels of 3 mm. It is necessary to know the position, on the photocathode where is made the absolute measurement, in order to know on which bin it is applied. Rather than a approximate centering, one here chooses to trust gravity: the PMT rests in a tube of

a slightly larger diameter. It is shifted toward the bottom by 3 mm. The absolute efficiencies which follow (at high gain and low gain) were measured in the pixel (0 mm, +3 mm), and not (0 mm, 0 mm).

The necessary light for the measurement itself is less: the matrix of LED of 12 mW are replaced by only one LED of 0.75 MW (maximum at 377 nm, see chapter 6.2). It is put in series with a resistance of 43  $\Omega$  and sends light pulsed to a 100 kHz rate. The flux received by the UDT photodiode is controlled in real time by connecting the analogical yield on a CAMAC ADC 3510 (11 bits). A LabVIEW interface makes it possible to be ensured of the stability of the LED during measurement and to eliminate the measurements during which the emitted light has too much varied. The calibration line of connects the ADC channel with the received current:

$$I_{UDT} (pA) = (4.878 \pm 0.010) \times Channel + (8.6 \pm 6.2)$$

We have then noted that the measured yield varied with of the quantity of light sent by the LED! Background noise of coming from the PMT photocathode the was very variable and on an abnormally high level: up to several thousands of pulses per second! We finally understood that the negative polarity of the voltage divider (divider VD 124K/T by Photonis, otherwise excellent in single electron resolution) was not adapted to measurements to such a weak level of light: it connects the photocathode to the negative high voltage. Micro-discharges occur then between the photocathode and the black plastic part, connected to ground, which maintains it on the sphere across the silica window. These micro-discharges cause brutal and uncontrollable increases of the counting rate. On the other hand, as soon as the photocathode was connected to the ground by using a positive voltage divider, these discharges disappeared.

For that, two voltage dividers of positive polarity were thus built at the laboratory on the model of the Photonis negative polarity dividers. Naturally, the voltage division itself, i.e. the tensions applied between each dynode, remained identical to what it was in negative polarity. The anode (now at the positive high voltage) is then connected to the outside through a large capacitor. This, which can cause base-line shifts at large rates, works here very well, for the rates are very low.

The background noise of each PMT has considerably decreased: that of PMT-filter went from approximately 3.000 counts/second to approximately 300 counts/second, and that of the PMT-JY, of approximately 300 counts/second (which was already excellent) to approximately 30 counts/second (which is exceptional). Without the abnormal background noise, the measurements are stable. They do not vary any more nor with the quantity of light, nor with the LED rate. A low level of background noise is a crucial element for the precise detection of fluorescence.

The measurement itself consists in counting the number of temporal coincidences between the pulses of the discriminator placed behind the PMT and those of the low frequency generator (GBF) feeding the LED for a sufficient length of time (100 s at 100 kHz). In the same time, the analogical signal sent by the UDT photodiode is recorded, in order to calculate the average channel and its dispersion throughout the measurement (which is then

converted into current). The photodiode calibration makes possible to calculate the number of corresponding photons. The absolute yield is the ratio between the number of photoelectrons and the numbers of photons:

$$\varepsilon = \frac{N_C R h c \alpha_{udt}}{\Delta t \lambda I_{udt}}$$

where:

- $N_C$  is the number of coincidences,
- $\Delta T$  is the duration of measurement,
- $R$  is the ratio of the fluxes measured in the preceding part
- $I_{udt}$  is the current read by the UDT photodiode through the optometer,
- $\alpha_{udt}$  is the photodiode conversion factor from current to power.

The UDT photodiode was used in the calibration and in the measurement. So, the error associated with its use cancels out. As:

$$\frac{\Delta R}{R} = \frac{\Delta I_{udt}}{I_{udt}} + \frac{\Delta \alpha_{udt}}{\alpha_{udt}} + \frac{\Delta I_{ophir1}}{I_{ophir1}} + \frac{\Delta \alpha_{ophir1}}{\alpha_{ophir1}}$$

the error of measurement is written:

$$\frac{\Delta \varepsilon}{\varepsilon} = \frac{\Delta N_C}{N_C} + \frac{\Delta(\Delta t)}{\Delta t} + \frac{\Delta \lambda}{\lambda} + \frac{\Delta R}{R} - \frac{\Delta I_{udt}}{I_{udt}} - \frac{\Delta \alpha_{udt}}{\alpha_{udt}}$$

and it remains:

$$\frac{\Delta \varepsilon}{\varepsilon} = \frac{\Delta \alpha_{ophir1}}{\alpha_{ophir1}} + \frac{\Delta I_{ophir1}}{I_{ophir1}}$$

All other uncertainties, of a statistical nature, are negligible. Finally, the error on the measurement of the efficiency of the PMT at high gain is 1.7% (naturally more lower than the 3.1% of the measurement of  $R$ ). It takes into account the effects of the terrestrial magnetic field. It is the value which was retained in table 6.4.

	PMT-JY	PMT-filtre
HT (V)	2350	2134
$N_{pe}$ (/s)	2140	2024
$I_{UDT}$ (pA)	$2177.12 \pm 5$	$2127.56 \pm 5$
$N_{ph}$ (/s)	10966	10716
Efficacité	$(20.0 \pm 0.3) \%$	$(18.9 \pm 0.3) \%$

Tab. 6.4 Results of absolute efficiency measurements of the two PMT at the position (0 mm, 3 mm) of the photocathode.

Now that one has the absolute value of the efficiencies in the bin (0, 3), one can normalize the chart of each PMT at high gain. The detector efficiency itself is integrated on the full useful surface PMT: it is the average efficiency of the detector. However, as the photocathode edges are much less efficient than the center, this integral is finally much lower than the value measured above: 16.1% instead of 18.9% for PMT-filter (with its 34 mm diameter filter in), and 9.7% instead of 20.0% for the PMT-JY!

### PMT-filter, for the fluorescence measurement

All the filter surface of the PMT-filter is active. A priori, it is thus not possible to increase the efficiency except if the effective surface is further decreased. A compromise can be found between the detection solid angle and the total efficiency. Evolution of the efficiency versus the detecting surface is shown on figure 6.21. It shows clearly that the detecting surface can be reduced to the third of the filter surface, allowing to reach a total

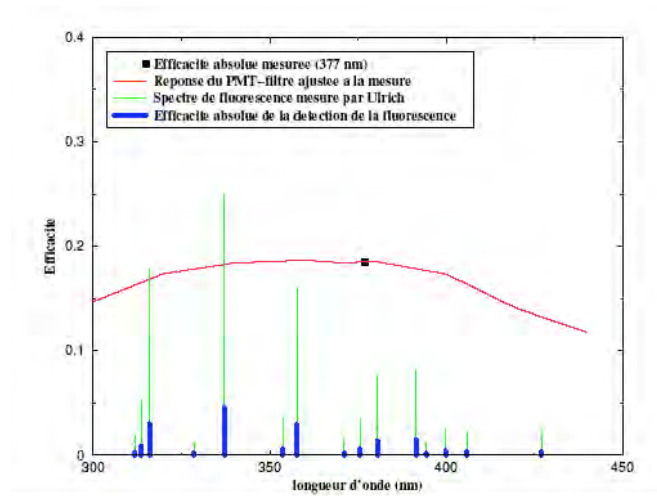


Fig. 6.19 Absolute efficiency of the PMT-filter when detecting the fluorescence spectrum. The black square shows the result of the measurement of the PMT-filter absolute efficiency. The red curve represents the spectral efficiency of the PMT convoluted with that of 2 mm thick BG3 filter, after adjustment with our absolute measurement. The spectrum in thin green lines represents the relative intensities of the lines of fluorescence, as Ulrich ([air]) measured it. Finally, the spectrum in thick blue lines is the convolution of the PMT-filter efficiency with the fluorescence spectrum. The sum of the detection efficiencies of each line gives the detection efficiency of the whole spectrum by this PMT.

efficiency hardly 3% lower than the center efficiency. So, a 20 mm diameter diaphragm was built. The effective surface,  $314 \text{ mm}^2$ , corresponds to an integrated efficiency of 18.5%. Naturally, the solid angle is lowered in this operation by a factor of 2.89, so that the net result is we detect less photons, but, and this is the important point, in the  $314 \text{ mm}^2$ , the PMT efficiency is much better controlled than the full filter surface. Hence, the uncertainties will be lower. This value of 18.5% for PMT-filter does not correspond yet to the fluorescence detection efficiency, because it corresponds only to the efficiency at 377

nm. Now, the fluorescence spectrum extends from 300 to 430 nm. Thus the PMT absolute efficiency must be integrated on this interval, by taking account of the proper spectrum of fluorescence. One uses for that the Photonis curve (precise in relative) and the spectrum measured by Ulrich ([air], itself also precise in relative). Figure 6.19 shows these different efficiencies. Each line is multiplied by the Photonis spectrum. The result is indicated in thick blue features on the figure. The integration of the blue lines gives a efficiency of 17.8%.

PMT-filtre	PMT-JY
$17.8 \pm 0.4 \%$	$19.3 \pm 0.3 \%$

Tab. 6.5 Absolute efficiencies of the two PMT at high gain. The value given for PMT-filter is integrated between 300 and 430 nm, and that of the PMT-JY is given for 377 nm.

### PMT-JY

The larger detecting surface of the PMT-JY, compared to PMT-filter, explain in part why the PMT-JY efficiency is lower than that of the PMT-filter. But the PMT-JY receives photons only on a rectangular zone of approximately 18 mm by 10 mm. The total efficiency integrated on a surface hardly larger (18 by 12 mm) is finally 19.3%. This number is given for 377 nm. One will refer to the curve shown on figure 6.20 for the analysis of the spectral measurements in order to know the absolute efficiency at a given wavelength.

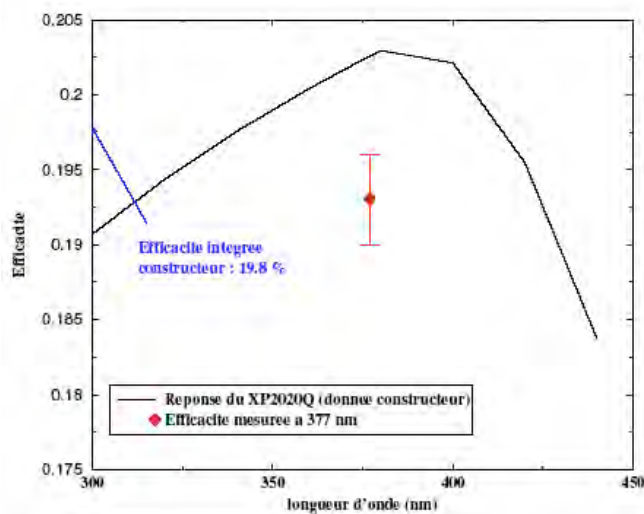


Fig. 6.20 Curve of absolute efficiency of the PMT-JY versus wavelength (note that the vertical scale does not start at 0 %).

Table 6.5 summarizes the absolute efficiencies used for both photodetectors, in the measurement of the fluorescence yield. For PMT-JY, it one must refer to the spectral efficiency curve for the analysis of the results. The spectral integration having made the

PMT-filter efficiency to go from 18.9% to 17.8%, one will undoubtedly lose efficiency on the PMT-JY in an equivalent way. Table 6.6 lists our estimates of error sources on the convolution.

Efficacité spectrale du PMT (données du constructeur)	0.5 %
Efficacité spectrale du filtre BG3 (données du constructeur)	0.5 %
Intensité relative des raies de fluorescence (mesure d'Ulrich)	1 %
Variations pendant la cartographie	0.5 %
<b>Erreur Totale</b>	<b>2.3 %</b>

Tab. 6.6 Estimates of the errors on the calculation of the efficiency of the detection of the fluorescence spectrum by PMT-filter

### 6.3.3 Conclusion: consequence for the fluorescence yield measurement

It is now possible to estimate the shift between two measurements of fluorescence integral yield of, one with a calibrated PMT, the other with a non calibrated one. The efficiency of the non calibrated PMT is simply the integral from 300 to 430 nm of the efficiency curve provided by the manufacturer. This, for the XP2020Q is 19.8%, and is indicated by an arrow on figure 6.20. For a Hamamatsu PMT H7195PX, used in [Nagano+04], it is 27%. Although these values are larger than those which we measured, Photonis and Hamamatsu recognize that they are slightly over-estimated, and that they are known only short of approximately 20%.

The over-estimate of the efficiency of a photodetector implies that one under-estimates the fluorescence yield. Thus, for a given gas, with equal energy, pressure and temperature, our measurements will give a result 11% superior so that it would have been if the XP2020Q had not been calibrated, by using the Photonis documentation.

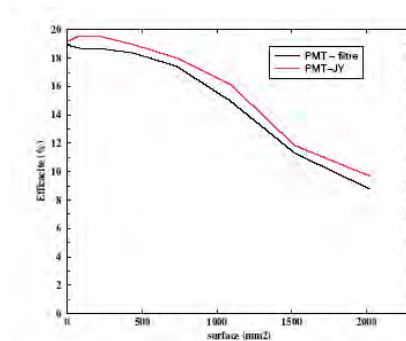


Fig. 6.21 Variation of the total absolute efficiency of the PMT in versus the detecting surface. Not to lose the benefit of a better efficiency in the central area, a diaphragm of 20 mm restricts the detecting surface of the PMT-filter (314 mm<sup>2</sup>). The PMT-JY receives photons on a rectangular surface of approximately 220 mm<sup>2</sup>.

## Third part

### Results

## Chapter 7

# Results of Fluorescence Yield Measurements and Implications

### 7.1 Execution of a measurement

Measurements were carried out in nitrogen and reconstituted air, which does not contain any argon. Naturally, the useful information for cosmic ray experiments is the fluorescence yield in air. Nevertheless, measures in pure nitrogen are used as reference insofar as there is no quenching due to oxygen. In a first time, the measurements in nitrogen are used for calibrations, since the Signal/Background (due to random coincidences) ratio is larger there than in air. They will be also used for to compare the results with those of the others experiments (fluorescence yield, ratio of yields in nitrogen and in air).

A measurement is launched only once that the internal pressure is stable, for example after a variation of pressure in the cross. If the nature of gas has changed (going from nitrogen to air), two steps are necessary to be ensured of the absence of impurities. The interior of the cross is pumped until an approximately  $5 \cdot 10^{-3}$  mbar vacuum is reached. Then, the gas circulates during 2 days with a flow from 1 to 2 L.h<sup>-1</sup>. One is certain that the gas is clean when measurement is perfectly reproducible.

By accumulating data over a very long duration, the statistical error on the integral measurement becomes almost negligible. Each measurement lasts approximately a night. Stability is controlled by recording regularly the internal and external pressures and temperatures. The measurements for which the internal temperature varied too much are eliminated in order to avoid introducing additional uncertainty on the results. As a matter of fact, a variation of 5° C on the temperature induces a variation of 1% on the production of fluorescence. On the other hand, a variation of 10% on the pressure modifies the fluorescence from only 0.2% (in the same direction as P).

Our precision on the temperature is 0.5° C, which involves an error of 0.1% on the fluorescence. It is of 0.2 mmHg on the pressure, whose incidence is of 0.03% on the fluorescence yield, which is completely negligible.

## 7.2 Extraction of the signal

The analysis is based on the extraction of the signal peak in the TDC spectrum. Let us recall that a TDC converts the duration separating two signals (a start and a stop) into a number. Here, the start is the coincidence between a photon signal and an electron signal. The photon signal can arrive from 0 to 100 ns after the electron signal. The stop is the electron signal delayed (see appendix A for more details).

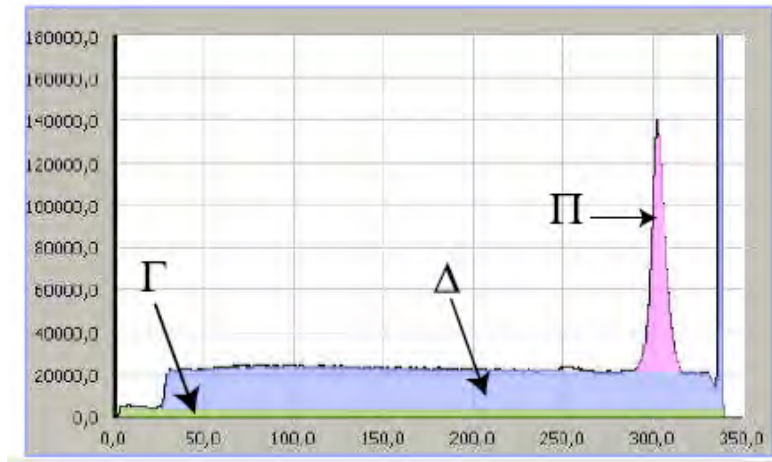


Fig. 7.1 Spectrum TDC of PMT-filter at low energy.  $\Pi$  is the true signal.  $\Delta$  is the randoms plateau.  $\Gamma$  is the plateau of random events (see text).

The spectrum recorded for the integrated measurement at 1.1 MeV is shown figure 7.1. Three components can be distinguished:

- the part  $\Pi$  (in pink on the graph), is the signal itself. The start is the signal resulting from coincidence between a photon of fluorescence and the electron which produced it. The stop is made by that same electron;
- the part  $\Delta$  (purple), is called the plateau of random coincidences. The “Start” is the signal resulting from a random coincidence between an electron and a photoelectron emitted by the photocathode of the PMT. The “Stop” is made by this electron. This photoelectron can arise from a spontaneous emission of the photocathode or from a true fluorescence photon of. In this last case, the photon is not associated in time with the electron (when for example two photons are emitted in the 100 ns window). No temporal relation existing between the two, all durations between start and stop have the same probability: the randoms spectrum is flat. If the photon signal precedes the electron signal in the coincidence (naturally with a superposition), then the TDC start is ordered by the electron. The constant time interval between the beginning and the end of the conversion produces then a narrow peak in the spectrum. It is what one can observe around channel 350.
- the part  $\Gamma$  (in green) is a plateau of random TDC events. As in the  $\Delta$  part, the “Start” is due to a random coincidence. But now the conversion stop of is made by another

electron (which did not take part in the coincidence): it is in some kind a plateau of "randoms of randoms". Its counting rate is thus lower. The larger the counting rate, the larger  $\Gamma$  will be, because it is proportional to the square of the counting rate. It is more important in the 1.1 MeV measurement than for the 1.5 MeV one.

## 7.3 Integrated yield from 300 to 430 nm

### 7.3.1 Measurements in air at atmospheric pressure

We will call integrated yield the result of the measurement made by PMT-filter. It is written:

$$Y = \frac{\Pi \frac{C}{H} (1 + D)}{N_e (1 + T_M) L_{moy} \varepsilon_{PMT} T_{quartz} \varepsilon_{geo}}$$

where:

- $\Pi$  is the integral of the signal peak of the TDC spectrum (see the spectrum given in example figure 4.3);
- $H$  is the integral of the TDC spectrum ( $H = \Pi + \Delta + \Gamma$ );
- $C$  is the number of coincidences counted by the scaler to correct the dead time effect;
- $D$  is the discriminator cut on the photon signal (see part 4.6);
- $N_e$  is the number of electrons having reached the scintillator (counted in a scaler);
- $T_M$  is the dead time (Temps Mort in French) of the scaler;
- $L_{moy}$  is the average length traversed by an electron in the volume of fluorescence;
- $\varepsilon_{PMT}$  is the absolute efficiency of the PMT-filter;
- $T_{quartz}$  is the transmission of the quartz window which closes the fluorescence volume;
- $\varepsilon_{geo}$  is the geometrical efficiency for the photon detection by the PMT-filter.

The numerical values of the different efficiencies and transmissions are gathered in table 7.1. Other than the quartz window transmission, given by the manufacturer, all the constant quantities were measured specifically. One will refer to the *ad hoc* chapters for more details.

Table 7.3 gathers the results obtained for the first two energy intervals. The measurement statistical error at 1.1 MeV is 0.2%, that at 1.5 MeV is 0.9%.

Grandeur	Valeur	
	Mesure à 1.1 MeV	Mesure à 1.5 MeV
$\Pi, H, C, N_e$	d'après spectre et échelles	
$T_M$	1.2 %	0.7 %
D	3.76 %	
$L_{moy}$	46.11 mm	
$\varepsilon_{geo}$	$3.689 \cdot 10^{-4}$	
$\varepsilon_{PMT}$	0.178	
$T_{quartz}$	0.992	

Tab. 7.1 Numerical values used in the analysis of the PMT-filter spectra. The quartz window transmission is given by the manufacturer. The other quantities were specifically calculated or measured.

The systematic errors are gathered in table 7.2. Values of D and  $T_M$  being very small, the errors on  $1 + D$  and  $1 + T_M$  are negligible (about 1% on a value of some percent). On the other hand, the uncertainty on the counting of the TDC is a consequence of the very high counting rates. Spectra of two measurements are not homothetic whereas they should be it, since the same physical phenomenon are dealt with. This induces a systematic uncertainty which one can evaluate by comparing the spectra of a “monohit” CAMAC TDC with the spectra of a “multihit” VME TDC. Comparing the production rates at low and high energy for the two types of TDCs, one deduces the uncertainty on the way the TDC works, and it is 4%.

Taking into account the statistical error, the total error thus amounts to 4.7% for the measurements at 1.1 MeV and 4.8% for those at 1.5 MeV.

Grandeur	Incertitude	Origine
$1 + D$	négligeable	mesure (voir section 4.6)
$1 + T_M$	négligeable	mesure (voir annexe A)
$L_{moy}$ et $\varepsilon_{geo}$	1.5 %	précision d'usinage et simulation
$T_{quartz}$	1 %	donnée du fabricant
$\varepsilon_{PMT}$	1.7 %	voir section 6.3
Comptage des TDC	4 %	voir texte
<b>Total</b>	<b>4.7 %</b>	

Tab. 7.2 Systematic uncertainties of the integrated measurement.

There is a ratio of 0.91 between the two measurements, compatible with this uncertainty. Is this ratio stable for different acquisitions? To check it, we use the very great number of measurements made during the wavelength spectrum acquisition (see section 7.4). These spectra were recorded with a TDC VME Multihit instead of the TCD CAMAC. How the TDC VME works is detailed in appendix A.

$E_{moy}$ (MeV)	P (mmHg)	T (K)	Rendement (photons/m)
1.1	753.8	295.95	$3.95 \pm 0.19$
1.5	751.8	296.05	$4.34 \pm 0.21$

Tab. 7.3 Measured fluorescence yields, and pressure and temperature for each measurement.

Figure 7.2 shows for each measurement the ratio of the number of counts in the signal P of the TDC spectrum, normalized to the number of electrons counted by the scaler. This quantity being directly proportional to the fluorescence yield, allows to evaluate the stability of our measurements. The slope of the straight regression line is compatible with a constant. The variances of each measurement are 0.2% at 1.1 MeV and 0.3% at 1.5 MeV.

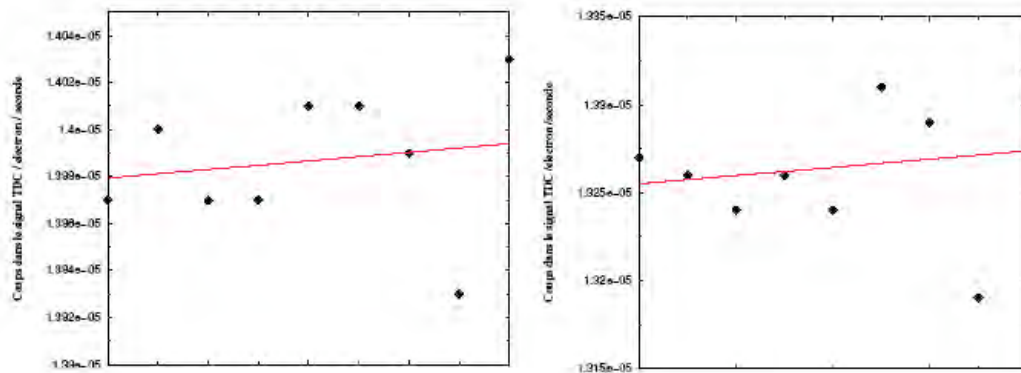


Fig. 7.2 - Variation of integral measurements at 1.1 MeV (left) and at 1.5 MeV (right). The ordinate is directly proportional to the fluorescence yield. The regression slopes are compatible with a constant (horizontal slope).

These curves show that measurements are stable. We can thus use them to check how our yield values relevant.

### 7.3.2 Normalization of the results

To be able to be compared with the preceding results ([Nagano+04]), our values must to be normalized in electron energy, but also in pressure and temperature. The usual normalization for electron energy is 0.85 MeV. That for the pressures and temperatures is the Standard US atmosphere at sea level.

$E_{moy}$ (MeV)	$dE/dX$ dans l'air ( $\text{MeV.cm}^2.\text{g}^{-1}$ )
0.85	$1.6875 \pm 0.08$
1.1	$1.673 \pm 0.08$
1.5	$1.680 \pm 0.08$

Tab. 7.4 Electron energy losses in air, used to normalize our results to the electron energy of 0.85 MeV.

## Energy normalization

For the experiments using electron sources, the usual normalization in energy is at 0.85 MeV. Table 7.4 points out the values of the electrons  $dE/dx$  in air. Our values are calculated according to the supplied bases of the National Institute of Standards [is]. Figure 7.3 shows the variation of the energy loss of an electron in air versus its kinetic energy. The averages energies of the two measurements, and the normalization energy, are indicated by arrows.

The uncertainty made during the calculation of the electrons average energies is highest for the lowest energy because of the more important contribution of the electrons diffused by lead. It is estimated at 6%, inducing on the  $dE/dx$  a variation of 0.05% for the measurement at 1.1 MeV and 0.3% for the one at 1.5 MeV.

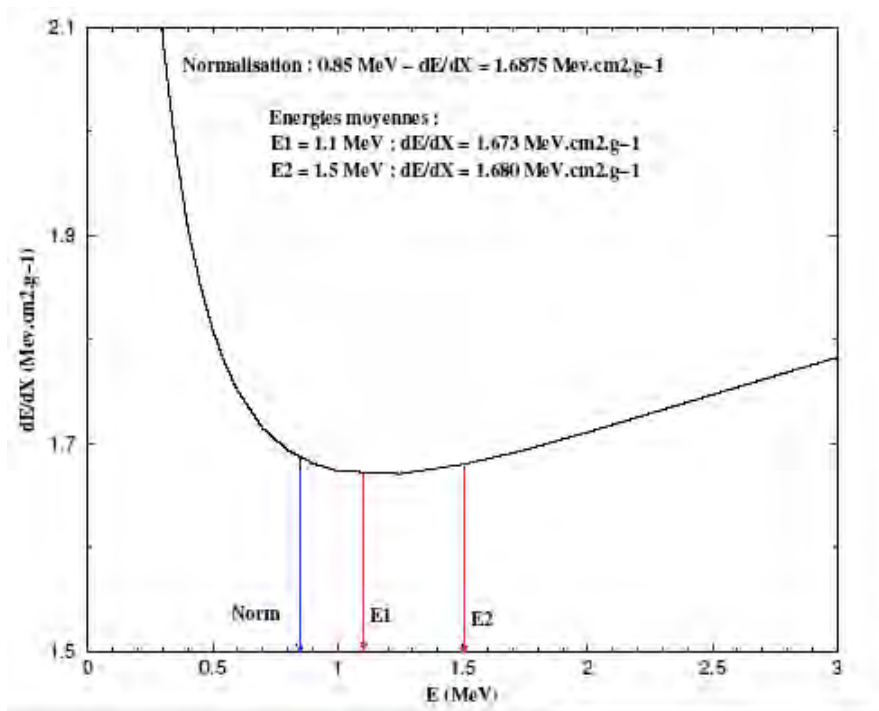


Fig. 7.3 Energy loss of an electron in air and average energies of each measurements.

Table 7.4 shows that the fluorescence yield at 1.1 MeV is 0.9% smaller than the yield at 0.85 MeV. This ratio is 0.4% for an energy of 1.5 MeV.

## Normalization to the US Standard pressure and temperature

This normalization is not as immediate as it is for the energy. As a matter of fact, contrary to all the other authors, the yield that we measure is already integrated from 300 to 430 nm. We thus cannot compare the yields line by line, as it is usually made. Moreover, it is for this reason that our measurement is more precise.

Our results are normalized using the models describing the fluorescence yield variation of each line with altitude. We can satisfy ourselves to use the simplest model, described in chapter 2 ([Nagano+04]), because the variations are practically identical from a model to the other. Let us recall that the yield versus altitude is written:

$$Y_\nu(z) = \frac{A_\nu \rho(z)}{1 + B_\nu \rho(z) \sqrt{T(z)}}$$

where constants  $A_\nu$  and  $B_\nu$  are listed in table 2.1.

We can calculate the yield which we would have measured if we had examined each line. For that, we use the coefficients  $A_\nu$  and  $B_\nu$  of [Nagano+04]. To normalize our results with the US Standard conditions, we compute the yield in the same way. Table 7.5 lists the pressures and temperatures of our two measurements, as well as the observed variations.

E (MeV)	P(mmHg)	$\Delta P/P(\%)$	T (K)	$\Delta T/T (\%)$	Y calculé	Rapport à US Std
0.85	753.8	0.07	295.95	0.08	$4.029 \pm 0.60$	0.9863
0.85	751.8	0.13	296.05	0.07	$4.028 \pm 0.60$	0.9860
0.85	760	0	288.15	0	$4.085 \pm 0.61$	1

Tab. 7.5 Fluorescence yields computed according to the [NaganoWatson00] model for three sets of parameters (P, T) and for a 0.85 MeV energy. The last line indicates the Standard US conditions of the atmosphere.

With the 1.1 MeV measurement conditions, the [Nagano+04] model gives 4.029 photons per m. For the 1.5 MeV ones, one calculates 4.028 photons per m. Under the US Standard conditions at sea level, one finds 4.085 photons per m.

The calculated numbers are higher than what we determined in experiments. To bring back them to 760 mmHg and 288.15 °K, we must use the ratios of the last column of table 7.5. These ratios are very precise for the model systematic errors, estimated to 15%, cancel each other. The uncertainty on the measurement at 1.1 MeV remains 4.7%, and that on the measure at 1.5 MeV, 4.8%, because the errors on pressures and temperatures are very small.

Our results, normalized to 0.85 MeV, 760 mmHg and 288.15° K, finally give

$Y = 4.05 \pm 0.19$ photons par mètre
$Y = 4.41 \pm 0.21$ photons par mètre

### Final result

The only experimental difference between the two obtained values of yield reside in the energy threshold applied to the electrons spectrum. It is thus natural to conclude this analysis by combining them. The absolute mean yield is:

$$Y = 4.23 \pm 0.20 \text{ photons par mètre}$$

Figure 7.4 gathers the different results obtained up to now. Experimental conditions (energy, temperature) are indicated for each experiment, but all the results are brought back to 0.85 MeV and the US Standard conditions.

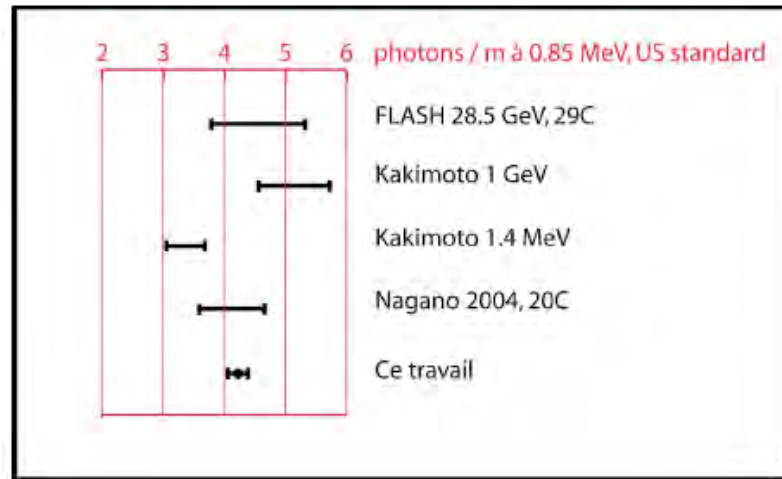


Fig. 7.4 Comparison of the fluorescence yield measurements results at 0.85 MeV and under the Standard US atmosphere conditions. The result of [Nagano+04] is the one for wavelengths between 300 and 430 nm, hence, it is directly comparable with our value.

Figure 7.5 shows the experimental results of preceding measurements ([Kakimoto+96], [NaganoWatson00]) and the parameterizations employed to deduce from  $z = 0$  measurement the fluorescence production in altitude. Our result and its uncertainty were added in red.

### Yield in number of photons per MeV

According to [Keilhauer04], the spectral fluorescence yield per traversed unit of length can be expressed:

$$Y_{\nu, \lambda} = \phi_{\nu} \frac{\lambda}{hc} \rho \frac{dE}{dX}$$

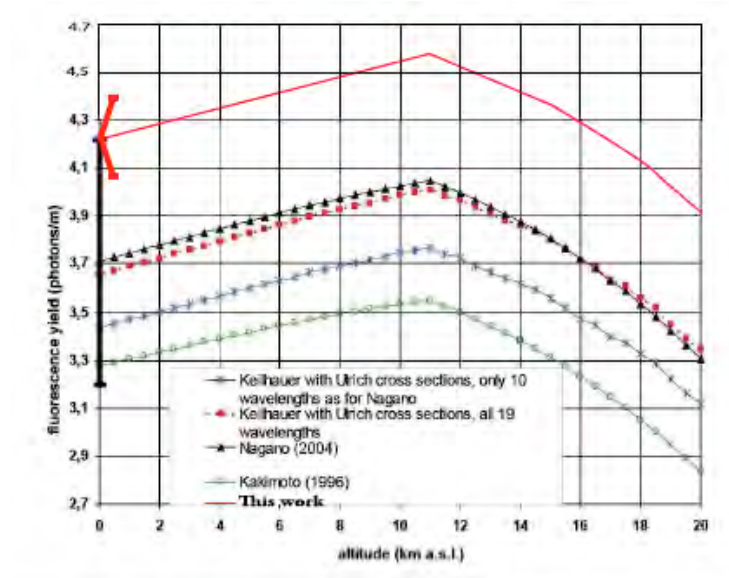


Fig. 7.5 Comparison of the results of fluorescence yields measurements at 0.85 MeV and under the Standard US atmosphere conditions. Measurements were normalized at sea level, and the parameterizations show the yield variation of the with altitude. In black, it [Nagano+04] result between 300 and 400 nm, and in red, our result.

or by unit of deposited energy in the medium:

$$Y_{\nu,E} = \phi_{\nu} \frac{\lambda}{hc}$$

that is to say

$$Y_{\nu,E} = Y_{\nu,m} \times \left( \rho \frac{dE}{dX} \right)^{-1}$$

where  $\Phi_{\nu}$  is the efficiency of the considered line as it was defined in chapter 2.

The integral measurement allows to get rid automatically of the  $\lambda$  parameter. The conversion of the preceding result gives a value of

$$Y_E = 20.46 \pm 0.98 \text{ photons / MeV}$$

This is totally compatible with the experiments at higher energy, for example [Colin05], which gives  $19 \pm 4$  photons / MeV.

### 7.3.3 Ratio of the yields in nitrogen and air at atmospheric pressure

By comparing the counting rates in the signal peak the TDC for **nitrogen and air**, we measure a **ratio** of the fluorescence yields of  $4.90 \pm 0.01$ . We exclude thus the value of

[DavidsonO' Neil64], which is 25, but we are compatible with the result of [Nagano+04], which gives  $5.48 \pm 0.71$ .

## 7.4 Spectral measurements

The fluorescence spectrum was carried out in air, at atmospheric pressure, with the spectrometer slits open to the maximum (2 mm). The full width at half maximum of the spectrometer response is then 6 nm, that is to say a  $\sigma \approx 3$  nm. A measurement was thus made every 3 nm, from 302 to 436 nm. Figure 7.6 points out the variation of the spectral width observed for different slit widths. Let us recall that the efficiency of the spectrometer measured in chapter 5 is  $(15.0 \pm 1.5) \%$  at 400 nm. This value is used to calculate our yields from 300 to 430 nm. The PMT-JY efficiency follows the efficiency spectral curve given by Photonis (see section 6.3).

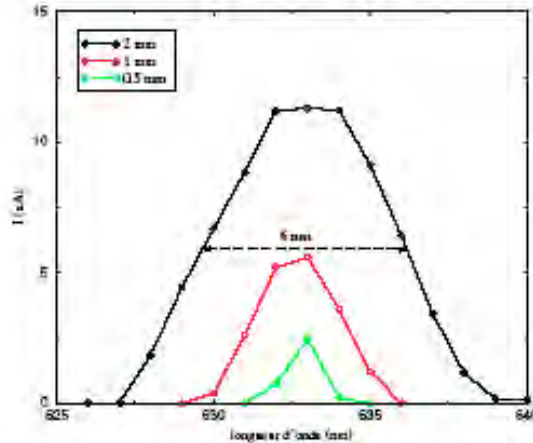


Fig. 7.6 Spectral width of the spectrometer for different slit widths. Measurements were made with the entry and exit slits at 2 mm. This measurement was obtained with a narrow source (He-Ne laser).

The fluorescence yield at a given wavelength is:

$$Y = \frac{\Pi \frac{C}{H} (1 + D)}{N_E (1 + T_M) L_{moy} \varepsilon_{PMT}(\lambda) \varepsilon_{JY} T_{lentille} T_{quartz} \varepsilon_{geo}}$$

where the specific quantities for this measurement are:

- $\varepsilon_{PMT}(\lambda)$  is the absolute PMT-filter efficiency at this wavelength;
- $\varepsilon_{JY}$  is the spectrometer efficiency;

- $T_{\text{lentille}}$  (lentille is French for lens) is the transmission of the convergent lens;

The numerical values of the constants are gathered in table 7.6.

This measurement was made possible only because of the very strong activity of the source. The counting rates are in effectively low: only 5 to 8 coincidences per second, and 0.16 count per second in the signal peak the for the most intense line. With this rate, it is only possible to make a maximum of two measurements per 24 h. The statistical error is a minimum of 5%, and the total error, around 20%, mainly because of the spectrometer itself.

The spectrum we measured is represented in the lower part of figure 7.8. It is first time that the absolute fluorescence spectrum is measured.

Grandeur	Valeur
$\Pi, H, C, N_e$	d'après spectre et échelles
$T_M$	1.2 %
D	3.85 %
$L_{\text{moy}}$	46.11 mm
$\varepsilon_{\text{geo}}$	$7.481 \cdot 10^{-6}$
$\varepsilon_N$	0.15
$T_{\text{quartz}}$	0.992
$T_{\text{lentille}}$	0.999

Tab. 7.6 Numerical values used in the analysis of the spectra of the PMT-JY.

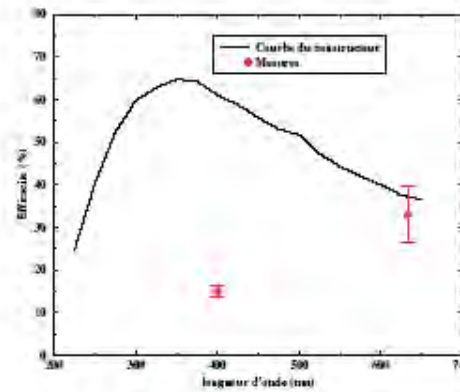


Fig. 7.7 Absolute spectrometer efficiency. Relative data given by the manufacturer (full black line) is known only to about 20%. The two red points are our absolute measurements at 400 and 633 nm.

The two error bars shown as example are purely statistical. The negative values are due to the method of extraction of the signal, which subtracts the background noise. One observes already a good agreement between the two spectra of figure 7.8.

As in the case of a laser, the lines are much more narrow that the 6 nm of the spectrometer resolution. The fluorescence yield of one line is thus given by the height of the curve at the

transition wavelength, and not by the integral. If one adds the heights of each observed peak, one obtains  $3.9 \pm 0.8$  photons per meter, which is totally compatible with the value measured with the PMT- filter.

The higher part of the figure shows the spectrum measured by Ulrich ([air]) with conditions very different from ours: the electrons have a very low energy (between 7 and 10 keV), produced by an electron gun. At this energy and because of the great number electrons, the production of fluorescence is very important, which allows to obtain good statistics to build the spectrum, and to close the spectrometer slits to get a very good resolution. In revenge, it is impossible to know the distance covered by the electrons because they are very quickly stopped in gas: the scale of this spectrum is relative.

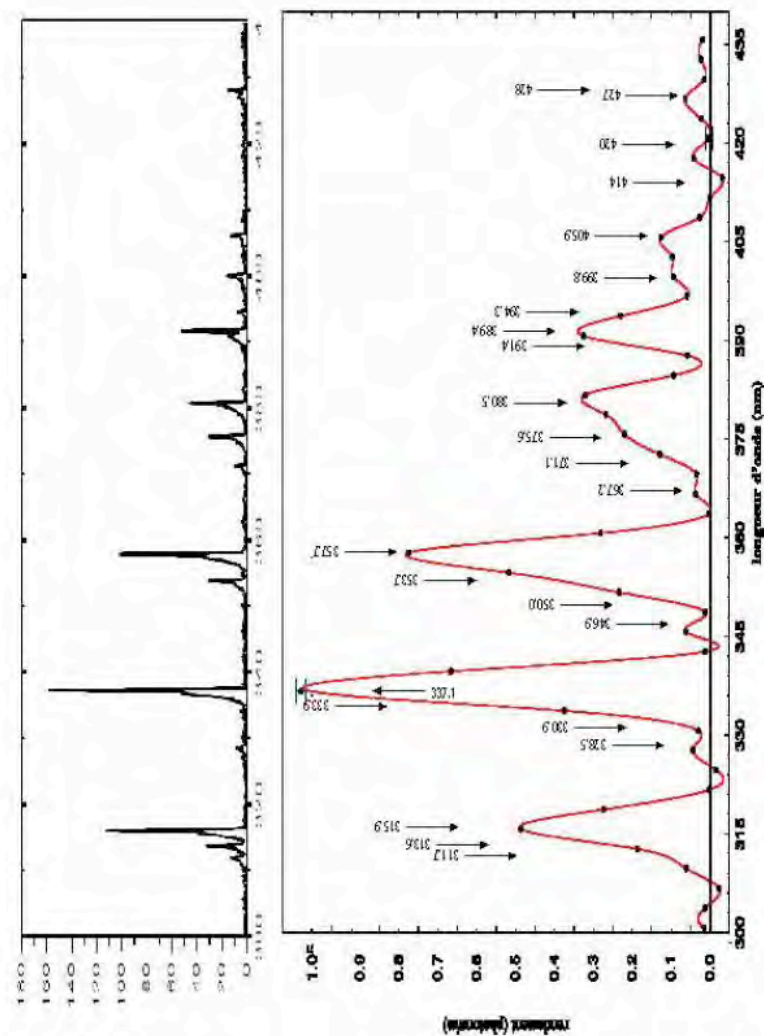


Fig. 7.8 In the lower part, the measured fluorescence spectrum at atmospheric pressure, with the slits open to 2 mm. Measurements are made every 3 nm. The upper part, for comparison, shows the spectrum measured by Ulrich [air] at lower energy.

By making a convolution of Ulrich measurements with a Gaussian of  $\sigma = 3$  nm, one can represent the spectrum which he would have measured with our spectrometer. The result of this calculation is the green curve on figure 7.9. It is superimposed to our result (in red). The two curves are normalized to 337 nm to compare the intensities (our result is absolute, Ulrich's is relative).

To the first order, the agreement between the two spectra is confirmed. One can however notice that the intensities which we measure are less important than those of Ulrich. At 316 nm, the difference is even a factor of two. We can suppose that our spectrometer efficiency is not constant between 300 and 430 nm and that it does not vary linearly (the measurement of this efficiency, described in chapter 5, was performed at 400 nm only). It is already remarkable to arrive to such an agreement with an apparatus so much damaged.

## 7.5 Conclusion

We could measure the absolute fluorescence yield of nitrogen in air, at atmospheric pressure, in a much more precise way than what had been made up to now. We also give the ratio of the yields in nitrogen and in air. Finally, for the first time, the fluorescence spectrum, between 302 and 436 nm, has been measured in air at atmospheric pressure with a source of  $^{90}\text{Sr}$ .

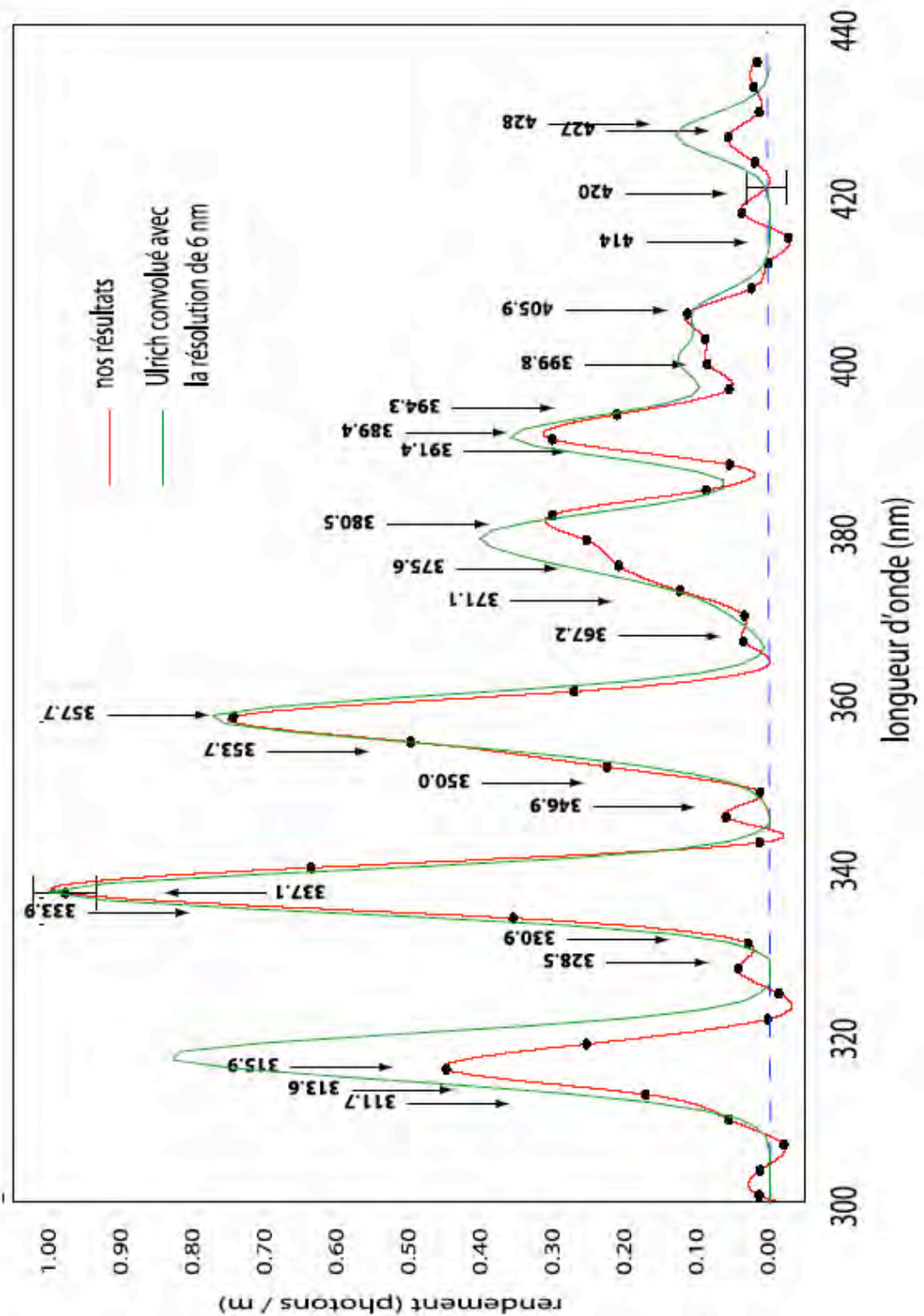


Fig. 7.9 Comparison between the fluorescence spectra of measured by Ulrich and our work (red). The green spectrum represents the convolution of spectrum measured by Ulrich with the opening of 6 nm (FWHM) of our spectrometer.

# Chapter 8

## Conclusion and Perspectives

Experiments of ultra-high energy cosmic rays currently use the nitrogen fluorescence, emitted with the passage of an atmospheric shower, to study the primary particle. The fluorescence phenomenon consists of a photon emission in the near ultraviolet when a nitrogen molecule de-excites. The detection and analysis of fluorescence, as it is shown in the first chapter, is easier and more precise than the sampling of the particles by a network of detectors on the ground. The Auger experiment, for example, still calibrates its surface detector of thanks to the energy measured by fluorescence.

Such a philosophy implies that it is imperative to know very precisely the absolute fluorescence yield of, i.e. the number of photons produced per meter traversed by an electron of the shower. Naturally, this yield evolves during the descent of the electrons towards the ground, because pressure, density and temperature change, and thus probability of radiative de-excitation of the nitrogen molecule. Different models of the variation of the yield with altitude lead to very similar results. One can thus consider that the yield of fluorescence is well-known in a relative way.

The knowledge of the absolute yield would thus allow to fix the scale of production of fluorescence. But the experiments carried out since 1967 with the aim to measure it never obtained a better precision than approximately 15% ([Bunner67], [Kakimoto+96], [Nagano+03] ). This work presents an experiment making it possible to reach an accuracy of 5%.

This experiment was conceived in opposition to the preceding experiments to realize two measurements:

- one known as integral, from 300 to 430 nm, by means of a band pass filter;
- the other, spectral, thanks to a grating spectrometer.

The electrons are generated by a very intense  $^{90}\text{Sr}$   $\beta$  source (370 MBq). Their energy is about one MeV. But the approach which we have chosen is different of that of other experiments, which all use narrow filters to measure the yield of the most intense lines of the nitrogen spectrum, with all the biases than that supposes. The grating spectrometer makes possible to optimize the resolution in wavelength carry continuous variations.

As it is described in chapters 4 and 5, each element of the set-up has been the object of a deep study and of a calibration if necessary. The various sources of background noise and

inefficiency were taken into account, for example by a lead shielding to protect from the x-rays that are produced in large quantity, or by a simulation of the possible interactions of the electrons. The gas pressure and temperature are regularly controlled. Its purity is ensured by a constant circulation in the fluorescence enclosure.

The measurement itself is based on counting:

- the electrons of the source;
- the coincidences between the electrons and the photoelectrons.

It uses the temporal relation existing between the photon of fluorescence and the electron who produced it, because the nitrogen can take up to a few tens of nanoseconds to de-excite itself. On a TDC spectrum, the signal is thus clearly recognizable. The normalization to the counting of the electrons and coincidences by fast scalers allows to eliminate the dead time due to the data acquisition.

The fluorescence yield is weak, and the photomultipliers (PMT) detect only one photon at a time. The PMT work in single photoelectron mode, i.e. at very high gain (approximately  $10^7$ ). It is thus of primary importance to know very precisely their own efficiency, i.e. the number of photons effectively detected compared to the total number of photons having reached the PMT. The PMT manufacturers admit an uncertainty of at least 15% on their calibration: it is this uncertainty which is responsible for the important error on the fluorescence yield. We have decreased the latter by measuring the efficiency of each PMT under the conditions of use. Our goal was to achieve a precision of about 5% on the fluorescence yield, and thus approximately 3% on the PMT efficiencies. We reached 1.7% on the PMT efficiencies and 4.5% on the fluorescence yield.

The efficiency of a PMT depends primarily on the wavelength of the incident photon and on the position on the photocathode, where it arrives. The spectral calibration (relative) of the manufacturer being precise, the absolute calibration with a given wavelength is sufficient. The variations on the photocathode surface require a specific measurement, because the efficiency varies strongly from one edge to another of the photocathode, and also from one PMT to another. We have thus realized a cartography for the two PMT which detect the photons.

The measurement of the absolute yield at the gain of the single photoelectron in a point of the photocathode is much more delicate. There are two possibilities to make an absolute measurement:

- to send a quantity of known light on the detector, i.e. to use a calibrated luminous source;
- to compare what the PMT measures and a calibrated detector.

On the level of the wished precision, the use of a calibrated source is not reliable. The uncertainty which it introduces is approximately 10%, because it is impossible to control

precisely its emission solid angle and its variations (in the course of time, or with temperature). This is why we decided to use calibrated light detectors.

The selected reference detectors are NIST photodiodes (calibrated by the National Institute of Standard). Their calibration is precise to 1.5%. By comparing at the same time the flux detected by the PMT and a photodiode, one gets rid of the systematics due to the temporal or temperature variations. The major difficulty in their use is due to the large difference of gain between them and the PMT: approximately 1 for the photodiode and  $10^7$  for the PMT. This means that the PMT must receive approximately  $10^7$  times less light than the photodiode.

We solved this problem by realizing a totally original set-up all based on the geometrical properties of integrating spheres. To reduce the quantity of light by some  $10^6$ , two spheres are fixed one to the other via a small diaphragm. One then has a flux divider, stable and very precise. We have thus been able to calibrate the two PMT at the single photoelectron gain to an accuracy of 1.7%, which had never been carried out up to now.

Finally, the absolute fluorescence yield has been measured in dry recomposed air (without argon, moisture nor impurities). At a pressure of 753.8 mmHg and a temperature of 295.95° K, an electron of 1.1 MeV produces  $3.95 \pm 0.17$  photons per traversed meter. This result must be normalized to be compared with the results of the previous experiments. The usual normalization is at an energy of 0.85 MeV, a pressure of 760 mmHg and a temperature of 288.15° K. Under these conditions, the average of the two realized measurements of fluorescence yield is  $4.23 \pm 0.16$  photons per electron and per meter.

Our result is totally compatible with those of the experiments of Nagano ([Nagano+04]) and FLASH [Belz+06], and the uncertainty has been divided by 2.9 and 3.6 respectively. But it excludes the results from [Kakimoto+96].

At present, the Auger experiment is using the fluorescence yield to calibrate in energy the surface network of detectors. The value of the yield used has thus a crucial importance in the rebuilding of the energy of the primary particle. From now on, the uncertainty on the energy of the showers can go from 15% to some percents (here we speak only of the instrumental errors, not of the uncertainties the hadron collisions at these extremely high energies can bring).

The value measured by Nagano between 300 and 400 nm is lower by almost 14% than our result (it is 3.73 photons/m). And, it is this yield which the Auger collaboration uses to deduce the detected cosmic ray energy: their energies are thus over-estimated by 14%. In energy, this is not too much. However, in flux (in E-3), this is almost 36% less.

At last, let us recall the ambiguity between the HiRes (measuring the showers fluorescence) and AGASA (sampling the muons and electrons at ground level) experimental results. In 2003, Bahcall and Waxman had proposed an explanation allowing to join together the two spectra [BahcallWaxman03]. Their assumption rests on possible difference of absolute energy calibration for both experiments. By evaluating a 15% undervaluation from HiRes an over evaluation also of 15% from AGASA, the two spectra are superimpose perfectly

(and, incidentally, prove the existence of the GZK cut). It seems that the results published by HiRes use the result of Bunner [Bunner67], that is almost 5 photons/m. This number being 22% superior to our own result, we go completely in the direction of Bahcall and Waxman assumption. Furthermore, we recently learned from AGASA spokesman M. Teshima, that a new analysis of their results lowered their energy by 10% which adds a further weight to this assumption.

## **Perspectives**

With the help of some improvements in the equipment, several studies could to be realized with this assembly. On one hand, the use of a Flash ADC would allow to record amplitudes and times simultaneously with much less dead time. We would then have an event by event data acquisition (what we could not do in this work because of the dead time), allowing the study of possible time/amplitude correlations. Moreover, a better apprehension of the pile-up would be possible. It would free us from the TDC problems arising when the “stop” has a MHz rate (it is then impossible to have an uncertainty lower than 4%).

In addition, a great improvement would be to measure the fluorescence spectrum with a spectrometer equipped with a CCD camera together with a light intensifier. The whole spectrum could be measured in each data acquisition. It would decrease the duration of data taking of a spectrum and improve the statistics and the resolution. Let us recall that each spectral measurement we made lasted one night, and that we have measured 46 points on the spectrum

With this type of more performing material, measurements to be considered are of three kinds:

- the modification of the nature of gas. By introducing 1 % of argon, then water vapor (up to 4%), then finally other types of impurities in controlled quantities, one can measure the fluorescence yield of under realistic conditions and study the effect of each component;
- the study of the variation of the yield with the pressure. One would then be able of to give a parameterization of fluorescence line by line, like other experiments do, but with better resolution and precision;
- the study of the variation of the yield with the temperature. We have to imagine a system allowing to cool the gas before injecting it in the fluorescence enclosure, and keeping it cold there. This is a rather complex problem, because the temperature to go down to  $-60^{\circ}$  C. To avoid condensation problems, etc, it the gas assembly (hence the fluorescence volume) should be part of a cryostat But nothing is impossible!

With these modifications and these measurements, the study of nitrogen fluorescence would be complete. One could then be interested in the other problems of fluorescence in the experiments of cosmic rays, like for instance its propagation in the atmosphere, in the presence of Rayleigh and Mie diffusing centers.

Fourth part

Annexes

# Annex A

## Data acquisition

### A.1 Acquisition electronics

The complete diagram of the acquisition chain of is represented on figure A.1. It was realized with NIM modules for treatment of fast signals (of the order the nanosecond) and CAMAC and VME modules to record the spectra (on a PC with Windows XP) and to count the impulses.

#### **Photons and electrons signals.**

The principle of the treatment of the signals is the same one for photons and electrons. Each anode signal is amplifier 10 times to save the PMT, to remain in a linear mode for the anode current and to be better observed with the ADC. The amplitude of the photons signals (single photoelectron mode) on the anode is a maximum of about 20 mV.

The signals are then duplicated: one remains analogical and is used to build the ADC spectrum, the other is sent in a discriminator. The discriminator is used to select the signals having exceeded a certain threshold. The produced logical signal is then sent in a coincidence unit.

Two discriminators are applied to the electron signal with two different thresholds. This is equivalent to make two simultaneous measurements at different electron average energies.

#### **Coincidences.**

The random coincidences rate between two signals of rate  $N_1$  and  $N_2$  (in Hz) and of width  $\tau_1$  and  $\tau_2$  (in seconds) is proportional to the sum of the signals widths:

$$f = (\tau_1 + \tau_2) \cdot N_1 \cdot N_2$$

As the electron and photon signals are naturally shifted in time, the logical electron signal must be at least three times broader than the lifetime of the molecular level. It is fixed to 100 ns, i.e. the signal photon (of width 8 ns) can arrive up to 100 ns after the electron. Such an important duration is not necessary at atmospheric pressure, since the lifetime is then shorter. But a study of the yield. of fluorescence at a lower pressure requires the width.

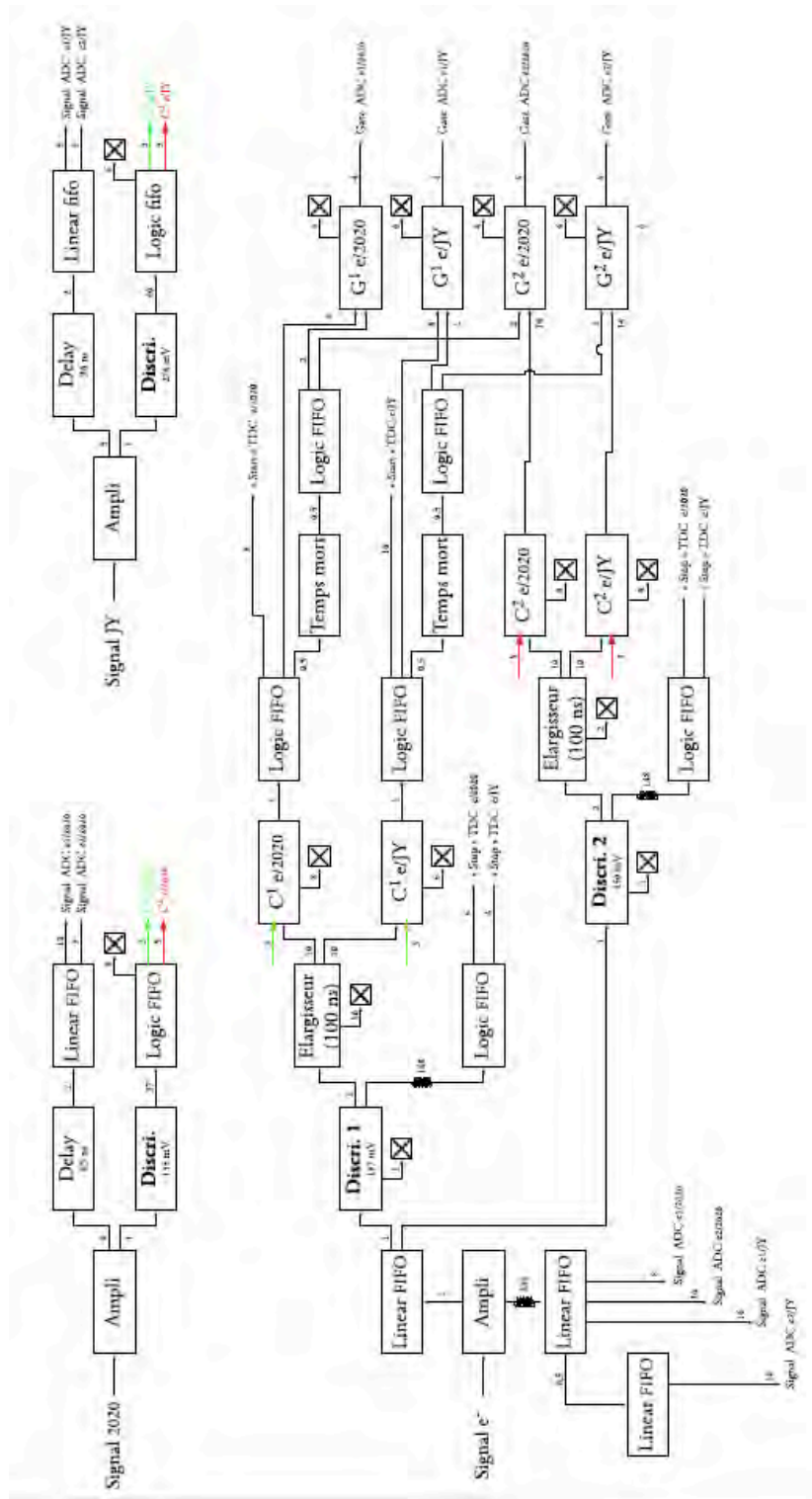


Fig. A.1 Complete diagram of the data acquisition. The numbers on top of each cable are their delay in ns. The discriminators thresholds of are also specified, and the scalers are symbolized by a cross in a square.

It must remain constant whatever the pressure to keep a maximum precision (biases cancellation).

Electrons and photons signals synchronization and the widths adjustments of the different pulses were realized before the source introduction. For that, three pulsed LED of 377 nm, have been placed at the center of the fluorescence enclosure, each one directed towards a PMT. The lifetimes were simulated by delays.

### **TDC.**

Time to Digital Converter. This module converts a time interval between two signals in a number (the TDC channel). Although the electron arrives before the photon, it is the coincidences which are used as a start to the TDC. The TDC is then stopped by the electron signal, delayed by 148 ns. This inversion avoids the great number of useless stops (i.e. an occupation of the TDC only for randoms), because there are very few photons compared to the electrons. The abscissa axis is thus reversed: the greater the TDC channel is, the smaller the time interval between the TDC start and stop is (see figure 4.3).

Fluorescence measurements were carried out with a monohit CAMAC TDC (LRD 2228A). Another TDC was used to control the PMT-filter spectrum during spectral measurement (then that TDC was on the PMT-JY). The other TDC is VME multihit unit (CAEN V1290N). It is equipped with a circulating memory which enables him to record several signals electrons per start (several stops for only one start). The signal peak and the randoms plateau are thus more important than for the CAMAC TDC. No computation of fluorescence yield was carried out with its spectra.

The number of randoms coincidences between an electron and the background noise of the PMT-photons is relatively important compared to the counting rate of each photon signal: approximately 200 per second for the PMT-filter signal, and 9 for the PMT-JY signal. The TDC spectra TDC of the random coincidences make a base line above which the peak of the signal rises. Thus when the number of randoms decreases, the statistical uncertainty on the peak surface decreases it too.

Before the polarity of the PMT-photons was reversed, their background noise was three times higher, and so were the random coincidences. One distinguished hardly the signal peak in the TDC spectrum of the PMT-JY. This modification was thus crucial in the measuring accuracy of the fluorescence spectrum.

### **ADC.**

Analog to Digital Converter. This module integrates the charge of a signal in a gate temporal user defined, and converts it into a number: the ADC channel. An ADC channel thus corresponds to a certain number of electrons (which depends on the ADC models). The ADC (LRS 2249A) require approximately 250  $\mu$ s for a conversion. The coincidences rate being too high, we created an artificial dead time of 300  $\mu$ s by blocking the signals.

The rate of coincidences is not important for the ADC spectra, because these are not used in the analysis. They are used only to control the stability of the gain of each PMT.

Taux de comptage approximatifs à pression atmosphérique (Hz)	
Signal e <sup>-</sup> "D1"	2 · 10 <sup>6</sup>
Signal e <sup>-</sup> "D2"	6 · 10 <sup>5</sup>
Signal photon PMT-filtre	1 000
Coïncidences e <sup>-</sup> "D1" - photon PMT-filtre	220
Coïncidences e <sup>-</sup> "D2" - photon PMT-filtre	70
Signal photon PMT-JY	40
Coïncidences e <sup>-</sup> "D1" - photon PMT-filtre	5

A.1 Summary of the counting rates of different signals. The indexes 1 and 2 indicate the energy threshold applied to the electrons spectrum. The conditions are air and atmospheric pressure.

### Counting scalers.

The pulses are counted at each stage of the treatment. The orders of magnitude of the counting rates are indicated in table A.1. The scaler reserved for the fastest signals is a 100 MHz VME module (VMEV560E with 64 bits). The others signals are counted in the only scalers that we had at our disposal, that are 25 MHz CAMAC modules (CERNSPEC 003 with 32 bits). These last are nevertheless fast enough to count the coincidences. All the scales receive narrow impulses (10 ns) to minimize dead times due to these widths. The dead times were measured for the two electron signals (the fastest), by measuring the rate versus their width. The results are represented on figure A.2. Extrapolation to an null duration pulse gives the counting rate which one would have with a zero dead time. With impulses of approximately 10 ns, the dead times are of the order a percent. One takes account of this effect in the analysis.

## A.2 LabVIEW interface

The interface of the CAMAC and VME modules of acquisition has been realized with LabVIEW 6.1. It allows possible to control the smooth running of the data acquisition. I conceived it and realized it completely.

### A measurement.

Each measurement lasts the equivalent of one night. If an anomaly occurs, which prevents the good course of the acquisition (for example, a server stops), the measurement data are lost. To avoid that, a measurement is made up of several takes of successive and completely independent data.

Each data acquisition gives 19 folders:

- 18 in the format of the LabVIEW histograms (12 ADC spectra and 6 TDC spectra);

- 1 folder (text format) which contains the summary of the data acquisition (date and hour, wavelength, pressures and temperatures at the beginning and at the end), scalers contents and the 18 histograms in text format.

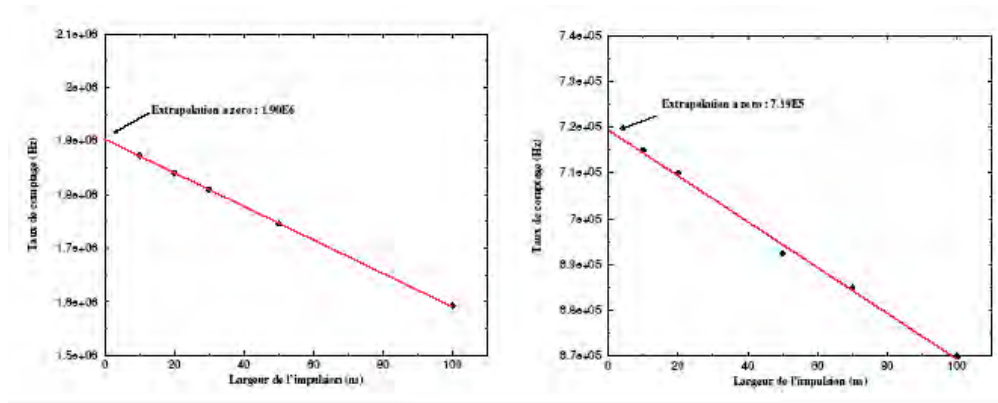


Fig. A.2 Measurements of the dead time of the two signals with the highest rate, i.e. electron signals at the discriminators yield. The discriminators pulses width was varied between 10 and 100 ns and the number of counts recorded for a given time in the scaler. The signals used here are the random signals coming from the source, and not generator pulses. The data are on a straight line (in red), as it should. The extrapolation of this line to a null width gives the counting rate for a zero dead time.

An event by event data acquisition was also prepared in order to study the time-amplitude correlations. It gives two binary folders. It was not however used, because at atmospheric pressure, the lifetimes are short and the correlations do not bring any additional information. The spectra amplitude always represent the same single photoelectron spectrum. There is no variation of this spectrum, other than possibly the gain.

### The principal menu.

The data acquisitions have a fixed duration, but the measurement lasts as long as the user wishes. Figures A.3 and A.4 are commented screen copies of the users interfaces. Figure A.5 shows, in the body of the acquisition program, part of the reading and recording loop of the ADC and TDC spectra.

### Execution of a data acquisition.

The scalers receive a start order and a stop order at the beginning and end of the data taking. In practice, two orders are sent. One is intended for the fast VME scaler (100 MHz). The other is a binary word which commands simultaneously the 6 CAMAC scalers (25 MHz). We considered that the two orders are simultaneous, because the time between them is well inferior to 1  $\mu$ s.

The program questions permanently ADC and TDC modules. As soon as one of them receives a conversion signal, the contents of the concerned inputs are recorded in the histograms. Their display is regularly refreshed to control the good course of the

measurement. A dead time is introduced during the recording and the display of the spectra, and we take account of it in the analysis. The flow chart of the course of a measurement is presented figure A. 6.

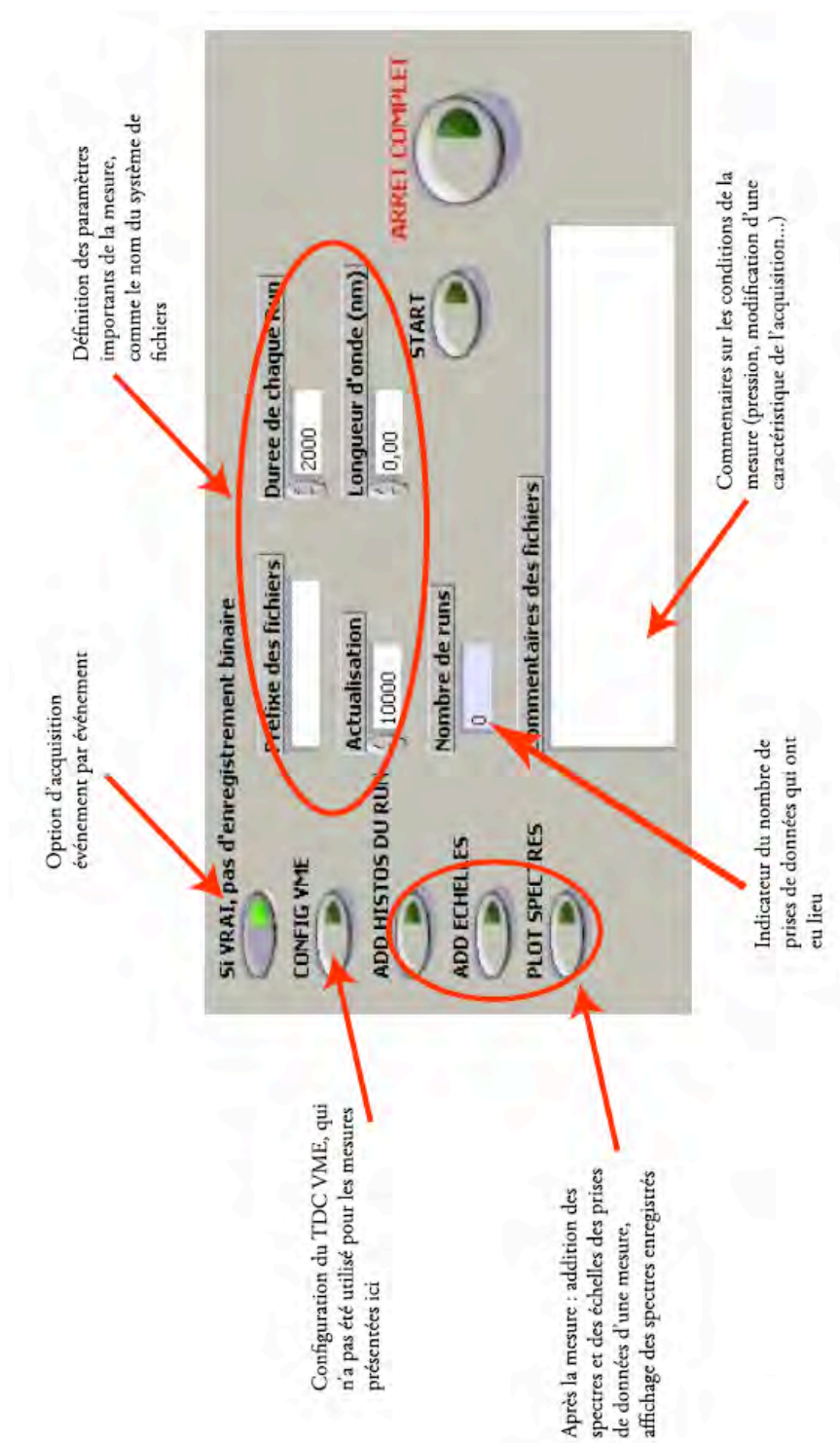


Fig. A3 – LabVIEW interface: how to start a measurement

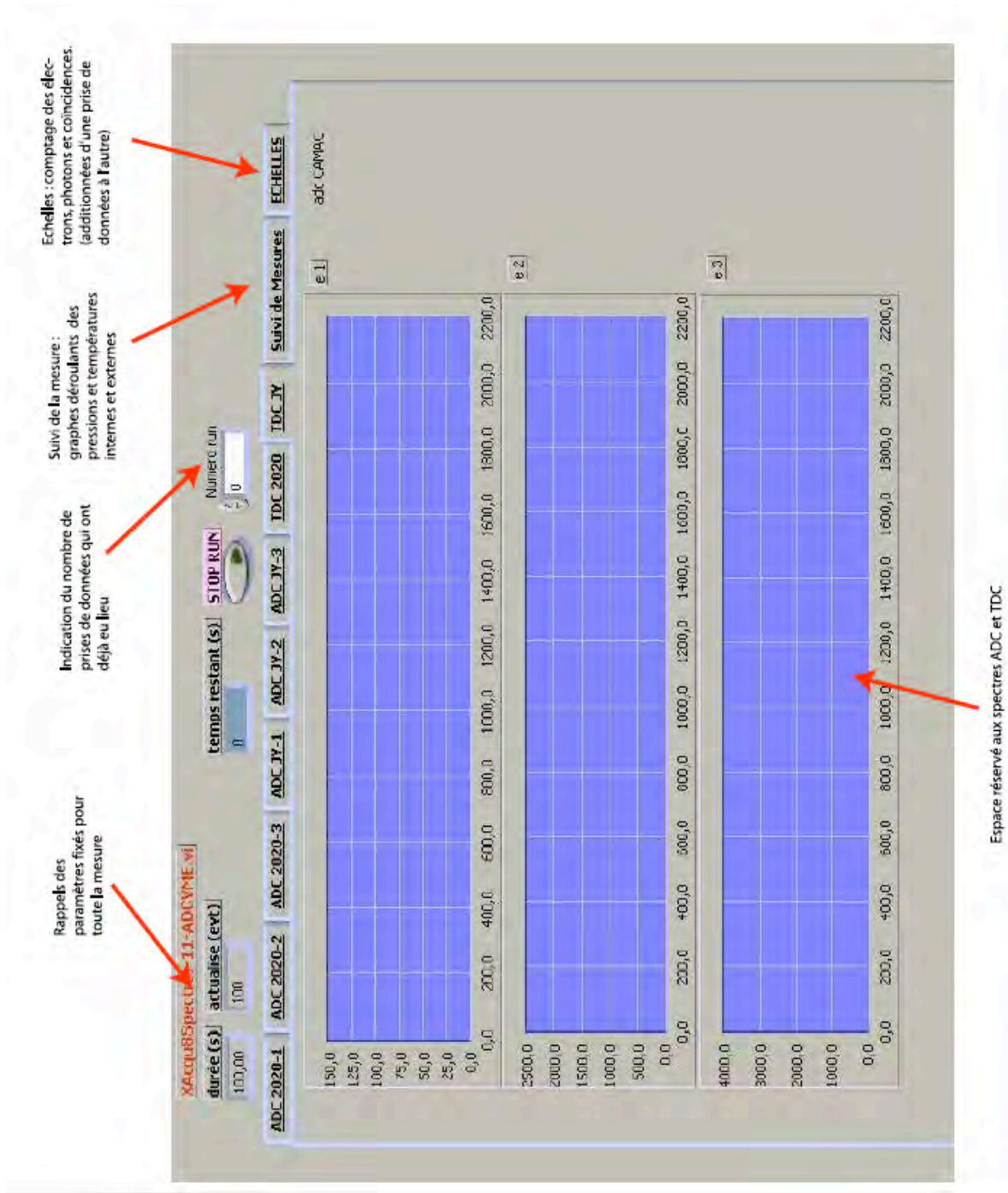


Fig. A4 – LabVIEW interface: spectra acquisition



Fig. A5 – LabVIEW program: reading and recording of the spectra

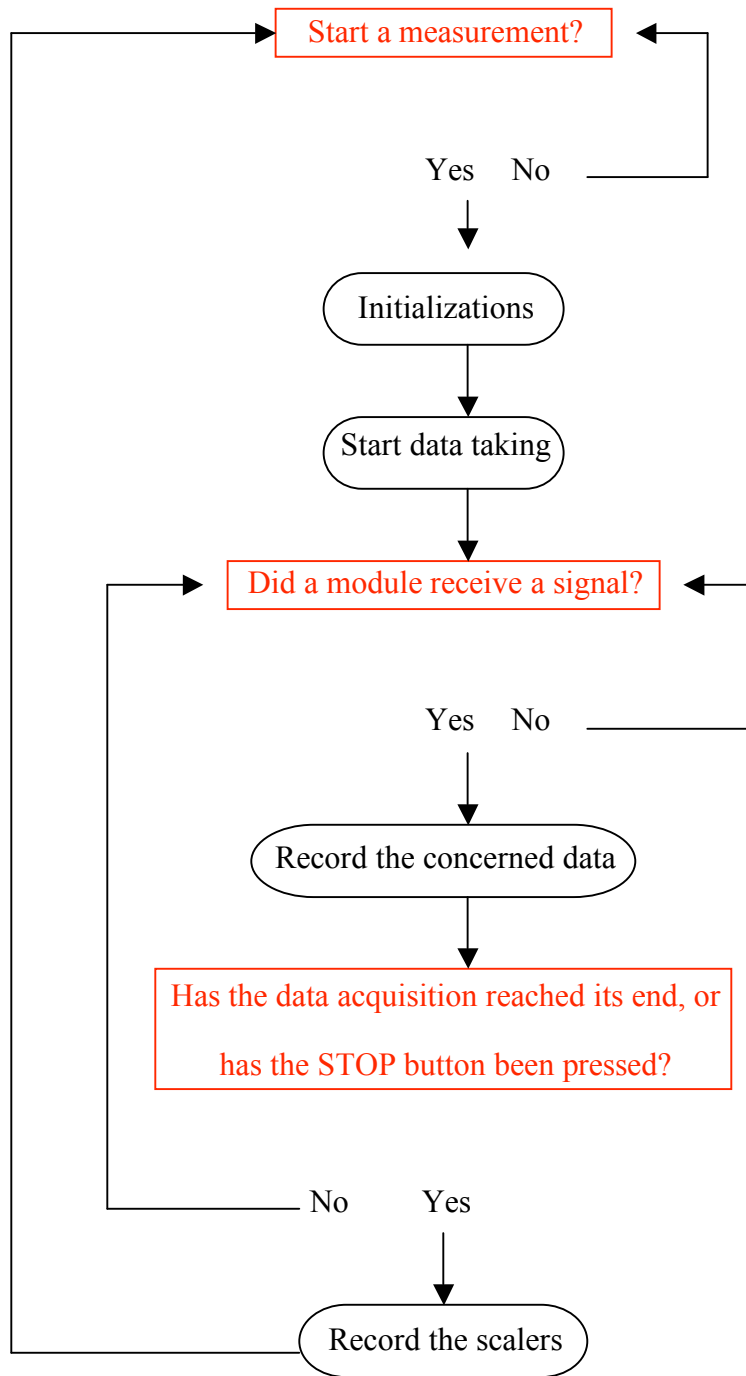


Fig. A6 – Flow-chart of a measurement course

# Annex B

## The Single Photoelectron Mode

### B.1 Spectrum of single photoelectron

When a PMT is exposed to a certain quantity of light, the probability of detection follows a Poisson law: the probability of detecting  $N$  photons is given by

$$P(N) = \frac{\mu^N \exp(-\mu)}{N!}$$

where  $\mu$  is the average number of detected photons.

This law is a discrete law, in particular when the level of light is sufficiently low, the photons are detected one by one.

The Poisson law is represented on figure B.1 in red for an average value of 0.025 (ratio of the peaks “0”/“1” of 40). Like it will be seen later, the spectrum of this figure is obtained by pulsing a LED with a low frequency generator (GBF).

Contrary to the PMT-electrons, the two PMT-photons work in single photoelectron mode. The first receives at least 10 000 photons per electron of the  $^{90}\text{Sr}$  source having touched the scintillator, i.e. approximately 2 000 photoelectrons by pulse. The two others detect only one photon at a time: approximately 1 every 3 ms for the PMT-filter, and 1 every 20 ms for the PMT-JY. However, the time-constant of the PMT being only of 10 ns, there will be never be more than one photoelectron at a time emitted by the photocathode. The yield pulse of will thus corresponds to only one photoelectron.

The width of the peak “1”, corresponding to the events where there was amplification, is due mainly to the fluctuations in the multiplication by the first dynode (if it is a factor of 4, then the resolution is  $1/\sqrt{4} = 50\%$ ). We call peak “0” the distribution centered on  $P(0) = \exp(-\mu)$ , and peak “1” that centered on  $P(1) = \mu \exp(-\mu)$ . Incidentally, “0”/“1” =  $1/\mu$ .

The peak “0”, or pedestal, is much narrower than the peak “1” for it corresponds to sending a gate to the ADC without sending a corresponding analogical signal. Only the electronic noise is then analyzed. The full spectrum is the sum of the peaks “0” and “1”. Figure B.1 shows a real spectrum superimposed on the discrete law. In this case, the ratio “2”/“1” is of

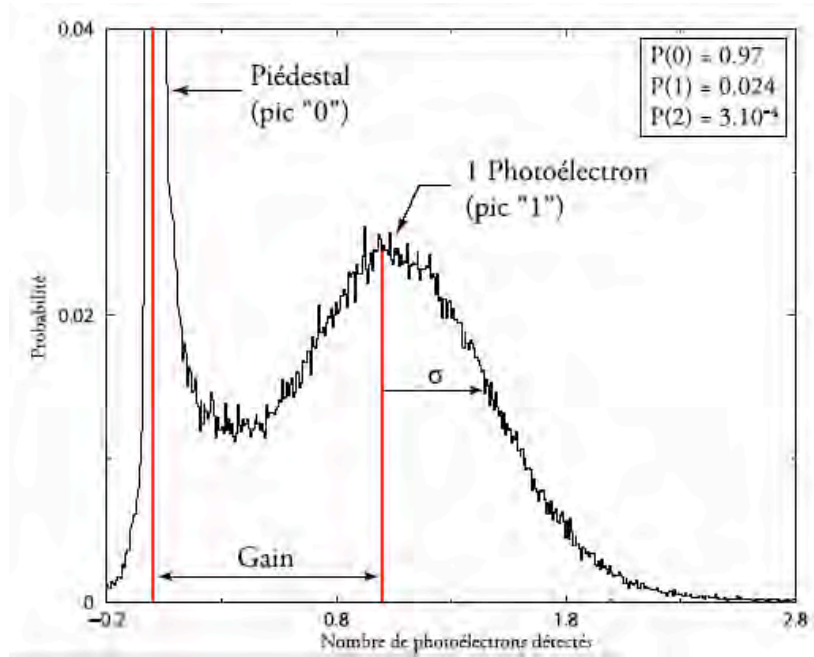


Fig. B.1 The Poisson law. In red, the discrete spectrum calculated for an average of 0.025, which corresponds to a ratio “0”/“1” of 40. In black, a single photoelectron spectrum detected by a PMT. In this precise case, the quantity of light is so weak that one never detects two photoelectrons.

0.0125, therefore lower than the required precision. If the fluorescence counting rates are much lower, this ratio will be still be smaller.

The peak of the single photoelectron is generally represented by Polya function (see for example [BlumRolandi94]), which describes the evolution of the number of electrons in a avalanche system. The Polya function admits the Poisson law as a limit case. It is necessary use it only if the contribution of the peak of 2 photoelectrons is not yet negligible, i.e. if the illumination is strong enough. It is useless here, because the LED is precisely set in order to have a large ratio “0”/“1”, and thus a “2” contamination completely negligible. Moreover, the ADC spectra are only useful to check that the PMT gain does not drift. They are not used in the analysis.

## B.2 Adjustment of the PMT-photons

The fluorescence measurement requires to detect the single photoelectrons in the best possible way. Hence, the discriminator of each PMT-photons must be set at the lowest part of the valley between the peaks “0” and “1”. For that, one uses a specific assembly schematized on figure B.2.

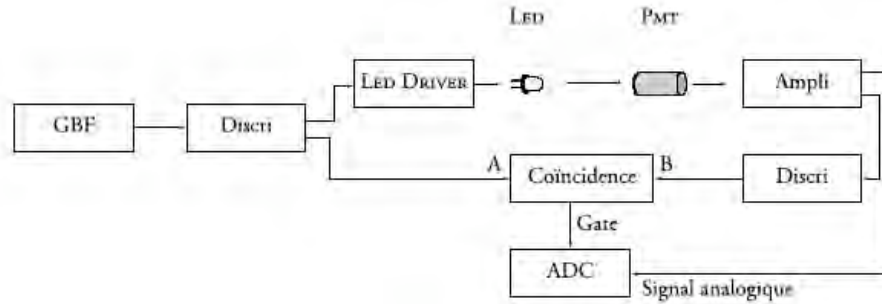


Fig. B.2 Diagram of an assembly allowing to set up the PMT working in single photoelectron mode.

A very weak quantity of light is sent to the PMT via a LED. The detected signal is analyzed by an ADC. This ADC is gated by a coincidence between the LED signal (A) and the PMT signal (through a discriminator) (B). If only (A) goes through the coincidence, the spectrum will show the “0” and “1” peaks (since the majority of photons will not have been detected by the PMT). If (A) and (B) are engaged in the coincidence, the spectrum will have only the peak “1” for which the analog signals will have exceeded the discriminator threshold.

A pulse generator (GBF) feeds the LED (377 nm) via a NIM Light Diode Driver (LDD CERN N4168). The LDD yield impedance ( $50 \Omega$ ), allows a good adaptation of the LED in fast pulse mode. A resistor of approximately  $40 \Omega$  is inserted in series with the LED. This resistance has a double function: impedance adaptation and temperature compensation. The yield voltage of the LDD, which gives the quantity of emitted light, is continuously variable from 0 to 25 V. The pulse width of can be as small as 5 ns, and the rise and fall times are of the order of 0.5 ns.

### B.2.1 Adjustment of the light level

The goal is to optimize the observation of the single photoelectron peak by varying the quantity of light received by the PMT. If there is not enough light, it is not possible, unless waiting several days, to reach enough statistics in the peak (at least a thousand counts). If there is too much of it, the probability of detecting two photons is not any more negligible with respect to detect one, and the resolution is such that the “2” peak will be on top of the “1”.

The peak “0 photoelectron” has a double utility:

- to ensure of the spectrum purity in “1”, i.e. contamination by the simultaneous detection of 2 photoelectrons is negligible. For that the ratio of the peaks heights “0”/“1” must be higher than 20 (we take between 30 and 50).
- to indicate the origin of the “1 photoelectron” peak which is at the center of the “0” peak. Effectively, one has to extrapolate until the origin to know the number of photoelectrons lost by the discriminator cut.

One can also estimate the PMT single photoelectron resolution through its ratio Peak/Valley, i.e. between the single photoelectron peak height and that of the minimum between the peaks “0” and “1”. In our case, to have reversed the polarity of the PMT has slightly degraded the Peak ratio/Valley. It went from 2.5 with a negative base to 2 with a positive one. This value is nevertheless sufficient to estimate that the resolution is 50%.

## B.2.2 Adjustment of the threshold of the discriminator

The discriminator threshold must correspond to the valley between the peaks “0” and “1”. The results are represented on figure B.3 for the two PMT. The spectrum cut by the discriminator, in red, is superimposed to the original single photoelectron spectrum, in black.

The loss due to this cut must also be evaluated. One has to estimate the number of single photoelectrons missed relative to the integral of the peak if there was no “0”. The position of the peak “0” indicates the foot of the true peak “1”. This “inefficiency” amounts to 3.76% for PMT-filter and 3.85% for the PMT-JY. This is taken in account during the data analysis.

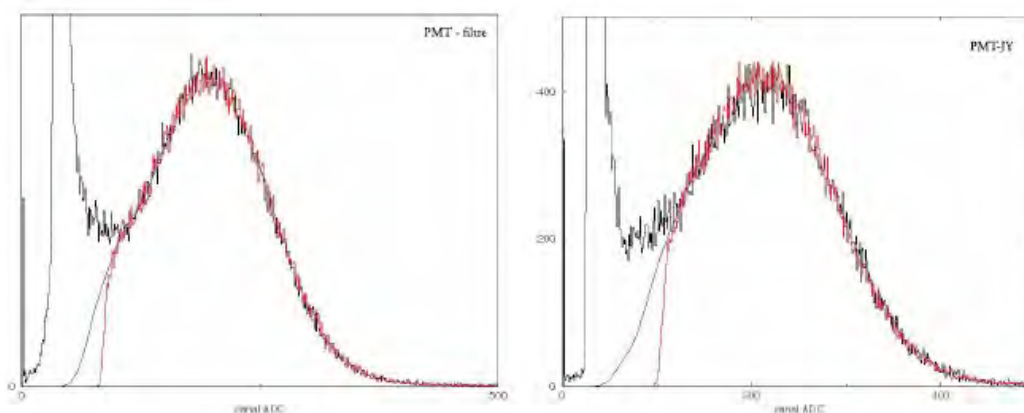


Fig. B.3 On the left, the PMT-filter spectra, and on the right, those of the PMT-JY. The single photoelectron spectrum, including the pedestal is in black. This pedestal (“0”) is the narrow (truncated) peak which corresponds to the absence of photoelectron when the ADC gate of the is only the generator controlling the LED: there are on average forty “0”s for one “1”. In red, the same spectrum, once applied the discriminator threshold. The loss of real photoelectrons is tiny: it corresponds to the integral between the blue curve (single photoelectron spectrum if there was no “0”) and the curve real in red (see text).

# Annex C

## Absolute calibration of the PMT at Low Gain

The photocathode quantum efficiency of a PMT is normally independent of the high voltage value applied to the tube. The small variation on the difference of potential between the photocathode and the first dynode (less than 100 V) cannot modify the extraction potential of the electrons.

On the other hand, the collection and multiplication efficiencies can vary in a significant way. This is why we have undertaken to measure the PMT efficiency at low gain, i.e. with a “low high voltage”, by sending a large number of photons on the photocathode.

The method of measurement is identical to that employed at low gain: to realize, using integrating spheres, an adapted light divider, and then to replace the photodiode by a PMT. However, the method used to observe the tube behavior is different. At high gain, one counts one after the other the single photoelectrons. Here, one observes a peak on a ADC. A variation of efficiency results in a variation of the number of electrons emitted per anode pulse, therefore by a variation of gain. The position of peak itself gives the gain; its width is statistically related to the number of photoelectrons emitted by the photocathode.

### C.1 Cartography

The gain chosen for the cartography is about  $10^4$ , which corresponds to a high voltage of 1385 V for the PMT-filter and 1509 V for the PMT-JY. The LED, driven by a low frequency generator (GBF), sends pulses at a 100 kHz rate. The level of light is such that the UDT control photodiode receives a power of about 12 nW with a background noise of about 1 pW. During the measurements, the light level varied by less than 1%. As the gain of the PMT varies slowly, mainly because temperature changes due to the voltage divider, each map must be carried out without interruption. This temperature changes have no incidence on the calibration at high gain.

To define the value of this gain, we chose to send approximately 20 000 photons per pulsates (about 5 000 photoelectrons). The PMT thus not work in single photoelectron. Mode. Anode pulses are directly sent on an ADC gated by the LED generator.

At a given position  $(x, y)$ , the spectrum observed is Gaussian and centered on a channel noted  $p$  with a variance  $\sigma_p$ . The pedestal for this measurement was adjusted to the channel 0

(use of a module qVt of Lecroy). The efficiency is directly proportional to the gain, i.e. to  $p$ .

Figures C.1 and C.2 show the normalized response of the PMT-filter. Figures C.3 and C.4 show that of the PMT-JY.

An important remark is that at low gain, it is already possible to extract the absolute efficiency of the PMT. On one hand, the power measured by the NIST photodiode gives directly the number of photons per unit of time. On the other hand, the width the Gaussian is statistically connected to the number of photoelectrons emitted by the photocathode, :  $\sigma_p / p = 1 / \sqrt{N_{pe}}$ .

The table below gives, as an example, what was measured at the (0, 0) position.

$p$	$P_{UDT}$	$N_{ph}/\text{pulse}$	FWHM	$\sigma_p/p$	$N_{pe}$	Efficacité
907	12.42 nW	23 555	34 canaux	$1.37 \cdot 10^{-3}$	5 337	$(22.7 \pm 4.6) \%$

However, this method is not very precise, because the distribution of the light between both fibers is not mandatorily equal and even optical fibers produce luminous lobes. One can try to appreciate the systematic errors. Those arise almost only from the way the light enters in the optical fibers. Through various tests, this error is estimated at 20%.

## C.2 Absolute efficiency at a point of the photocathode

### Optimization of the set-up

Each pulsates is composed of approximately 20000 photons: only one sphere is sufficient to attenuate the luminous flux between the photodiode and the PMT. The flux ratio is written

$$\frac{\Phi_{UDT}}{\Phi_{PMT}} = \frac{A_{UDT}}{\pi r^2}$$

By using a 5 mm diameter diaphragm at the entry of the PMT and a 9 mm one at the UDT, we have a ratio of about 4. The set-up diagram is represented on figure C.5.

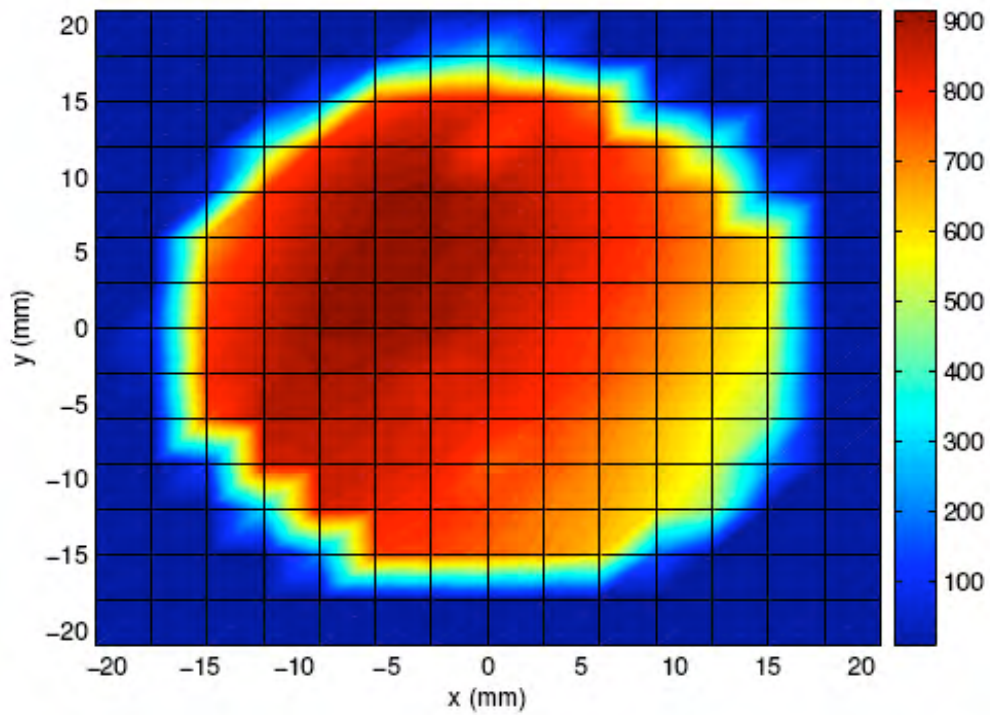


Fig. C.1 Topography of PMT-filter at low gain. The normalization to the luminous flux measured by the photodiode is already made.

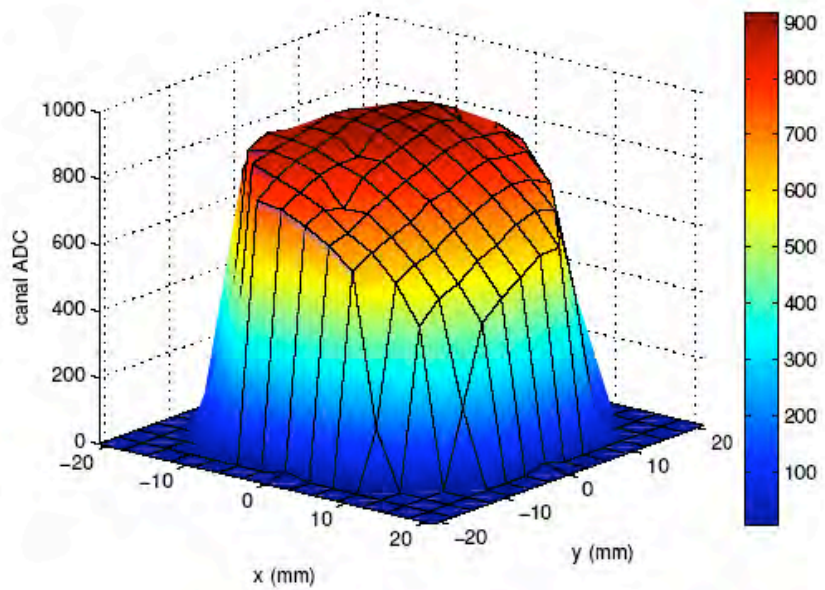


Fig. C.2 Response of PMT-filter seen into 3D and under the same conditions that figure C.1

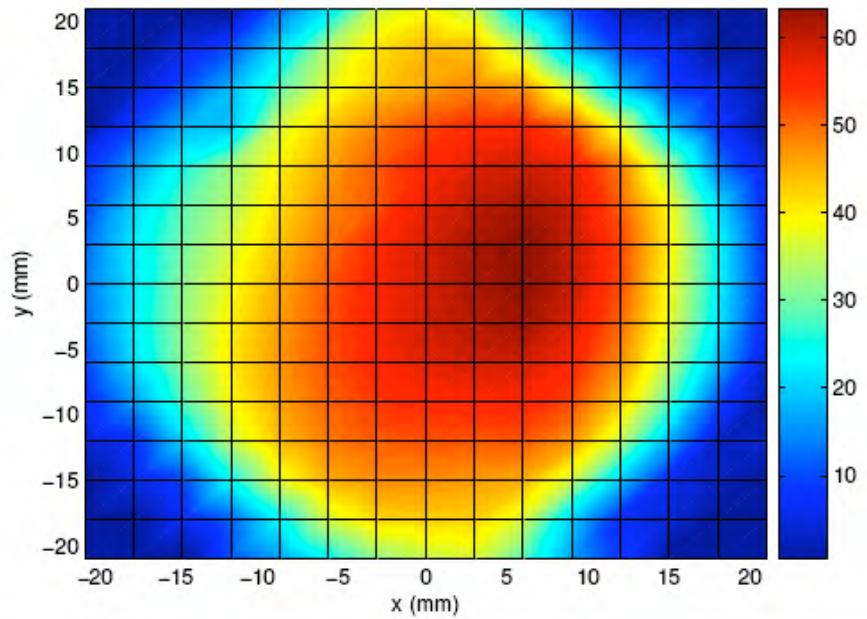


Fig. C.3 Topography of PMT-JY at low gain. The normalization to the luminous flux measured by the photodiode is already made.

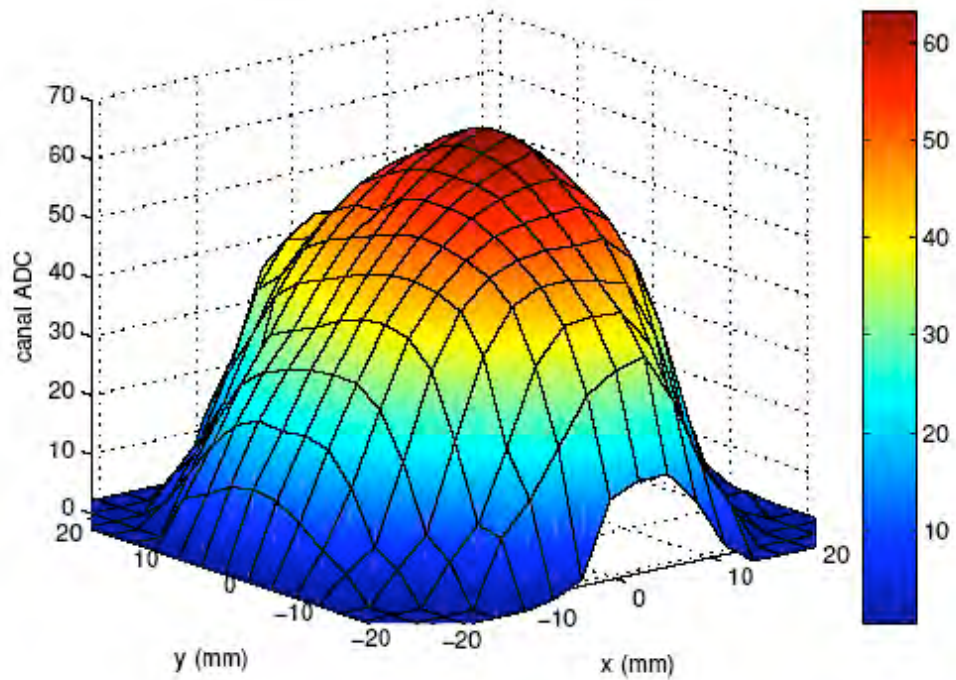


Fig. C.4 Response of PMT-JY seen into 3D and under the same conditions that figure C.3

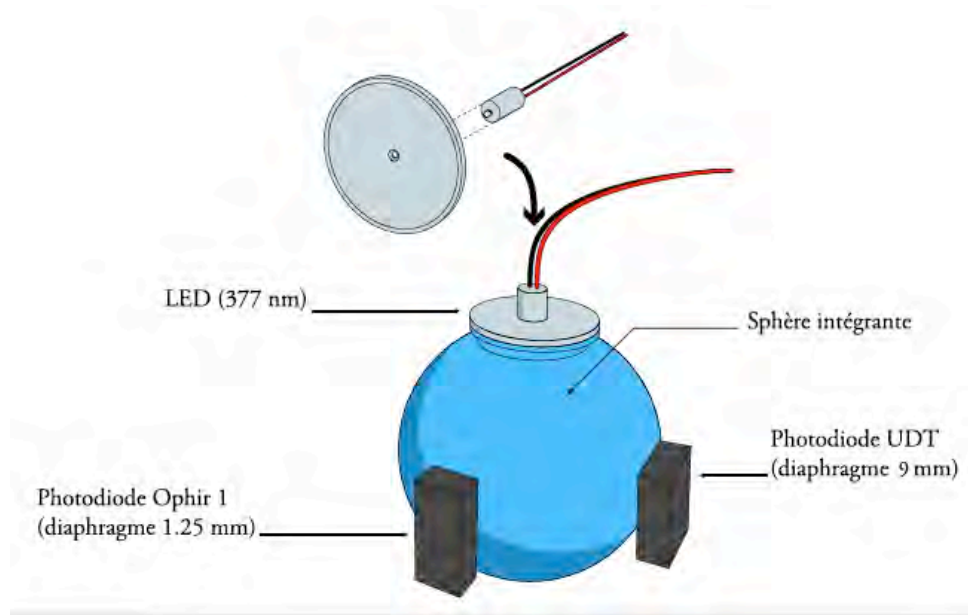


Fig. C.5 Determination of the division of the luminous fluxes for the efficiency measurement at with low gain.

### Measure of the ratio of luminous fluxes between the two exit ports of the sphere

In the same way that at high gain, one measures at the same time the currents in each photodiodes. The photodiode Ophir 1 is put at the place what will occupy the PMT. The 377 nm LED is enough now to light both photodiodes. Table C.1 gathers the currents and the conversions into power.

	UDT	Ophir 1
<b>Courant lu</b>	2347 pA	550.4 pA
<b>Facteur de conversion</b>	0.1556 A/W	0.1320 A/W
<b>Puissance correspondante</b>	15.084 nW	4.170 nW

Tab. C.1 Currents in each photodiode to determine the ratio of the fluxes received by the PMT and the UDT photodiode during the efficiency measurement.

The inaccuracies are the same as for the measurement at high gain (see section 6.3). The error on the result is 3.1%. The luminous fluxes ratio is this time:

$$R = 3.6 \pm 0.1$$

## Efficiency measurement

The assembly is represented on figure C.6. The Ophir 1 photodiode has simply been replaced by the PMT.

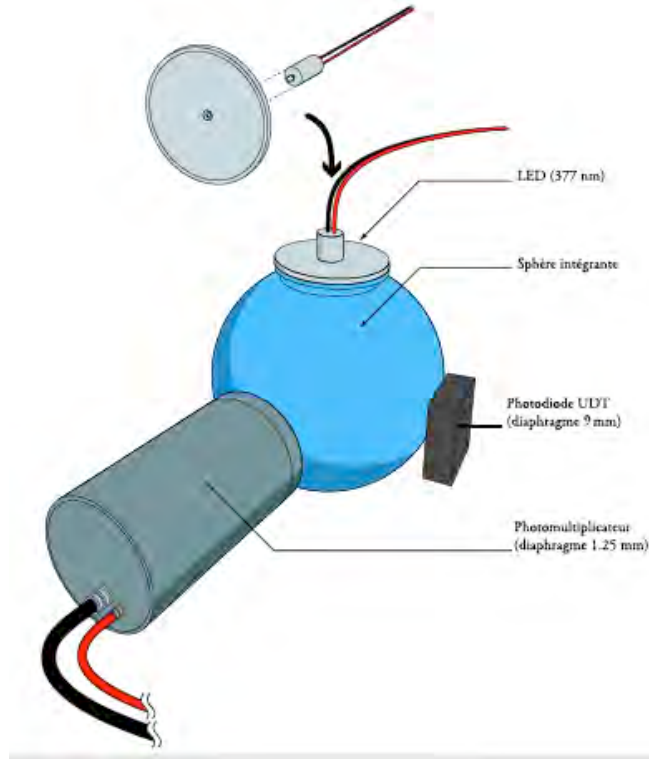
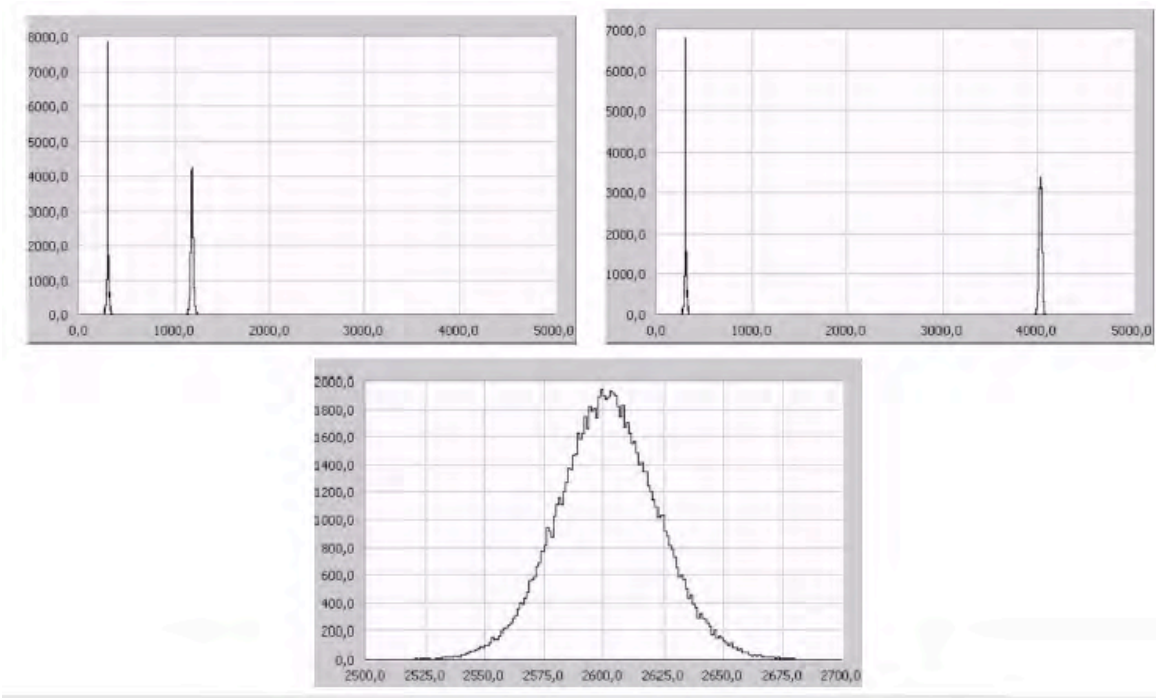


Fig. C.6 Assembly for the efficiency measurement at low gain.

This measurement required some minor modifications of the acquisition electronics relatively to that used at high gain. Let us recall that at low gain, it is the ADC spectra that are studied. In order for the signal to be correctly integrated, the ADC gate width had to be increased. The new positive voltage dividers have a slight effect on the signal shape (due probably to the large condenser put in series with the anode) who joined the base line a little later that with the negative bases.

For this measurement, the integration gate was 500 ns instead of 100 ns. The pedestal width is then 41 channels. It is too large a width for our measurement, because this width occurs in the error analysis (see further). We thus have removed the gain 10 amplifier at the entry of the acquisition chain. It is anyway useless at low gain. The width of the pedestal then went naturally to 3 channels only when adjusting the high voltage so that the peak  $p$  is at the same channel as it was with the amplifier.

The measurement itself consists in computing the efficiency for different gains, all in the range of the low gains. For that, one sets the high voltage, records the spectra corresponding to the signal and to the pedestal. An example of the recorded spectra is given on figure C.7. The LED emits pulses at a rate of 10 kHz.



C.7 Examples of spectra recorded to measure absolute yield of PMT-filter. The peak located around channel 300 is the pedestal: it is obtained when the GBF sends signals only to the gate, but not to the LED. The other peak (bottom) is the signal. Its position and its width (both de-convoluted from the pedestal) allow to deduct the average number of photoelectrons and the gain. When the high voltage is increased, and thus the PMT gain, the signal integrated charge is more important: the peak moves towards the right (top).

The position of the pedestal must be withdrawn of that of the signal to obtain the gain. Like one needs the width ( $\sigma$ ) of the signal peak to evaluate the PMT efficiency, one must de-convolute the intrinsic system contribution, taken equal to the pedestal width. If one calls “measurement” the values directly obtained on the graphs, and “true” the same values from which one withdrew the pedestal, then:

$$P_{\text{vrai}} = P_{\text{mesure}} - P_{\text{zero}}$$

$$\sigma_{\text{vrai}} = \sqrt{\sigma_{\text{mesure}}^2 - \sigma_{\text{zero}}^2}$$

The associated errors are:

$$\Delta P_{\text{vrai}} = \Delta P_{\text{mesure}} + \Delta P_{\text{zero}}$$

$$\Delta \sigma_{\text{vrai}} = \frac{\Delta \sigma_{\text{mesure}} \sigma_{\text{mesure}} + \Delta \sigma_{\text{zero}} \sigma_{\text{zero}}}{\sigma_{\text{vrai}}}$$

The error on  $p_{vrai}$  is negligible: the statistics are so important that the error on determination of the positions of the peaks is much smaller than 1%. The error on  $\sigma_{zero}$  and  $\sigma_{measure}$  varies between 0.4 and 1 channel.

The following law is used

$$\sigma_{vrai}/p_{vrai} = 1/\sqrt{N_{pe}}$$

to deduct the average number of photoelectrons.

The error on the number of photoelectrons is then:

$$\frac{\Delta N_{pe}}{N_{pe}} = 2 \frac{\Delta \sigma_{vrai}}{\sigma_{vrai}}$$

It is thus proportional to the error on the peak width. But  $\sigma_{vrai}$  itself shows already an uncertainty, therefore  $\Delta \sigma_{vrai} / \sigma_{vrai}$  can be rather large. That will degrade the measurement precision, which will be about 5% starting from 1200 V, instead of the 1.7% obtained at high gain. At high gain, there was no error on the number of photoelectrons since there could be only 1.

The current received by the photodiode,  $I_{udt}$ , and the ratio of the fluxes measured with a sphere,  $R$ , provides  $N_{ph}$ , the number of photons falling on the PMT per pulse:

$$N_{ph} = \frac{1}{f} \frac{\lambda}{hc} \frac{I_{udt}}{R \alpha_{udt}}$$

where  $f$  is the frequency of the pulses sent to the LED. The error related to the UDT photodiode cancel out, since the concerned systematic error is the same one for the measurement of the flux ratio and for the efficiency measurement.

$$\frac{\Delta N_{ph}}{N_{ph}} = \frac{\Delta f}{f} + \frac{\Delta \lambda}{\lambda} + \frac{\Delta R}{R} - \frac{\Delta I_{udt}}{I_{udt}} - \frac{\Delta \alpha_{udt}}{\alpha_{udt}}$$

The statistical errors are, here also, negligible. It thus remains:

$$\frac{\Delta N_{ph}}{N_{ph}} = \frac{\Delta \alpha_{ophir1}}{\alpha_{ophir1}} + \frac{\Delta I_{ophir1}}{I_{ophir1}}$$

One thus deduces the absolute efficiency from it:

$$\varepsilon = \frac{N_{pe}}{N_{ph}}$$

and its own uncertainty:

$$\frac{\Delta \varepsilon}{\varepsilon} = \frac{\Delta N_{ph}}{N_{ph}} + \frac{\Delta N_{pe}}{N_{pe}}$$

that is an error of about 5%. One sees on figure C.9 that this error is all the more lower that the high voltage is high, i.e. the gain is large.

The gain is directly related to the distance between the pedestal and the signal peak: an ADC channel is worth 0.1 pC (ADC VME V792N of 12 bits), that is to say exactly  $6.25 \cdot 10^5$  electrons:  $G = 6.25 \cdot 10^5 \cdot p_{vrai} / N_{pe}$  and:  $\Delta G / G = \Delta N_{pe} / N_{pe}$

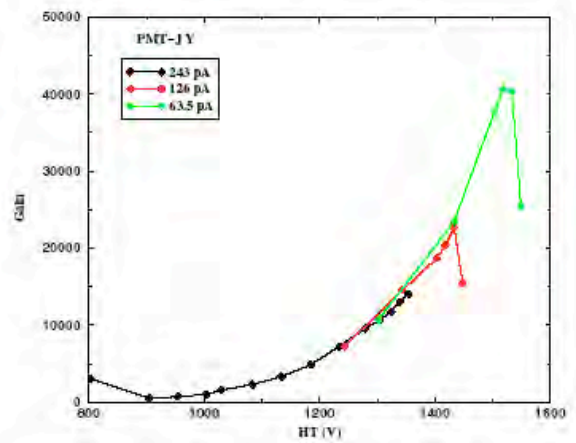
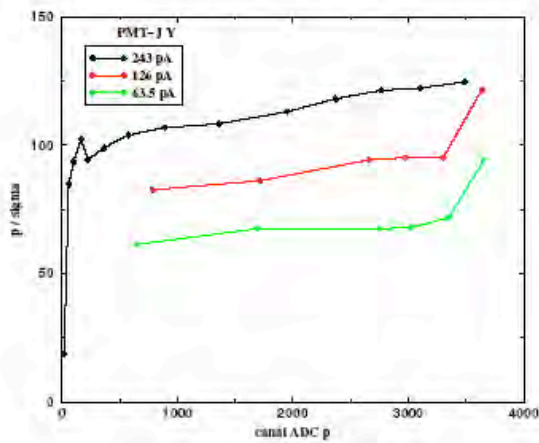
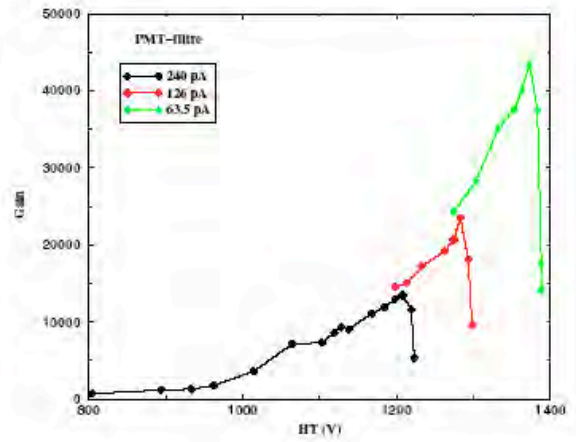
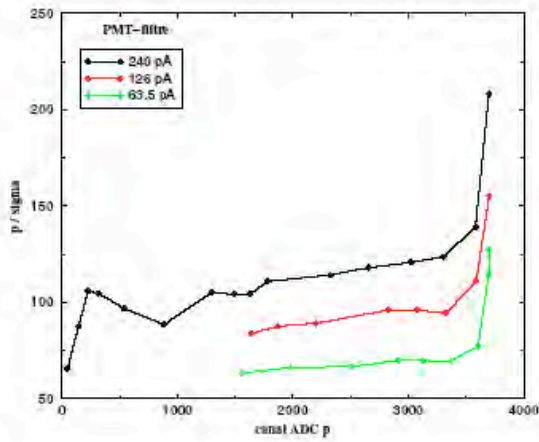
The results of measurements of the two PMT are represented on figure C.8. By definition,  $p / \sigma$  is a measurement of the number of photoelectrons. One notices immediately the brutal change of operation mode which takes place for the highest voltage values. For each illumination: the gain falls, while the number of photoelectrons increases. This is a effect of the photomultiplier non-linearity. The maximum anode current accepted to preserve a mode linear to 2 % is 280 mA. This value is given for a voltage of 2155 V. Moreover, the maximum current of anode is proportional to the power 3 (approximately) of the high voltage. This means that, for example, when the voltage is divided by 2, the maximum anode current of is divided by 8! At low gain, the PMT is thus quickly beyond limiting conditions.

This phenomenon could be checked for the two PMT by decreasing the quantity of light emitted in the sphere. The correspondence between the current measured by the photodiode and the number of photons reaching the photocathode per pulse is given in table C.9. The voltage is then increased to measure the yield, in order to continue on the curves shown on the four graphs of figure C.8: each color corresponds to a different illumination. The limit of linearity is clearly recognizable on the three curves of each graph with the PMT gain falling down after a given high voltage. One cannot deduce an efficiency for these nonlinear modes.

Courant Iu (pA)	Nombre de photons
63	21 212
126	42 425
240	80 809

Tab. C.2 Numbers of photons received by the photocathode in each LED pulse, for different intensities.

Once the results outside the linear mode removed, one can plot the efficiency variation versus the high voltage for each PMT, like the curves of figure C.9 show.



C.8 Results of the low gain measurements with. On the left, the  $p/\sigma$  ratio, related to the number of photoelectrons (see text). On the right, the evolution of the gain with the high voltage applied to the PMT. The brutal changes of modes which one can observe on the two types of graphs show the loss of linearity of the PMT: the anode current is too big. The three curves of each graph correspond to different illuminations: the less important this illumination is, the more it is necessary to increase the gain to preserve an equivalent resolution.

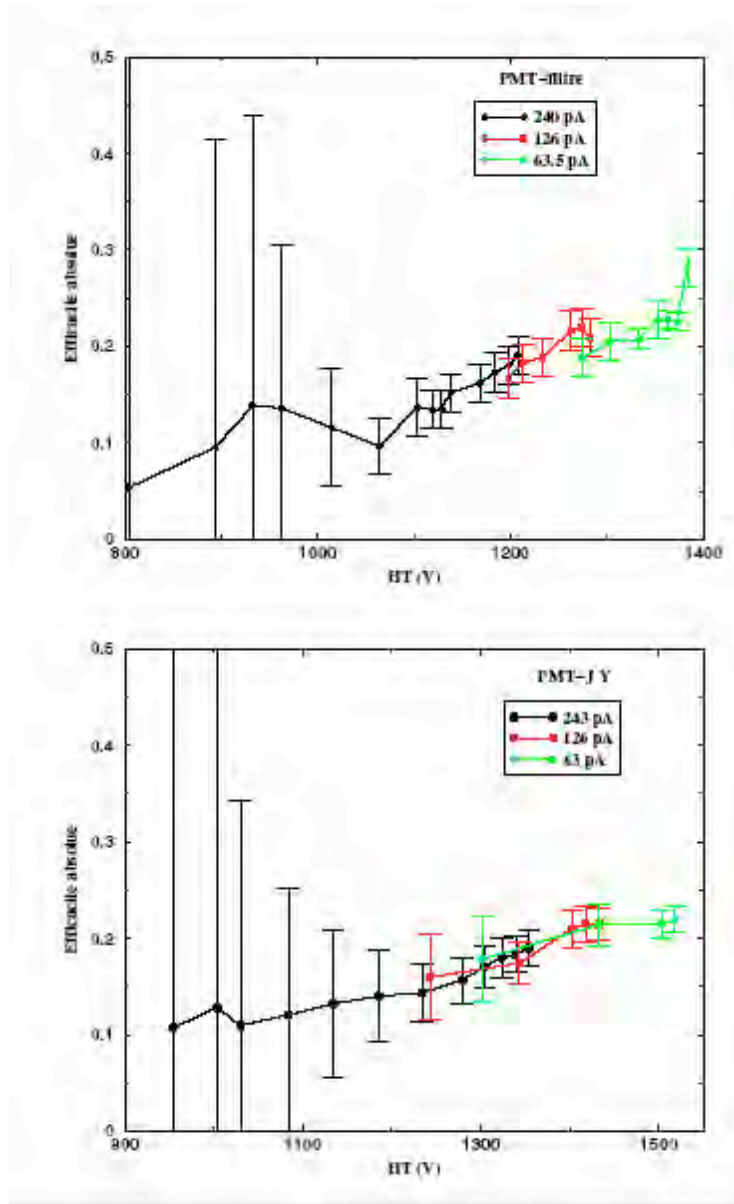


Fig. C.9 Variation of the efficiency of each PMT versus the applied high voltage.

One notices that it can take values higher than that measured at high gain. One would rather expect that the voltage applied to the dynodes be so large at high gain that the collection is always better than it would be at low gain. However, it is not the case for the PMT XP2020Q, which were optimized for “high” gains, but anyway lower than those necessary to work in single photoelectron mode[Lavoute].

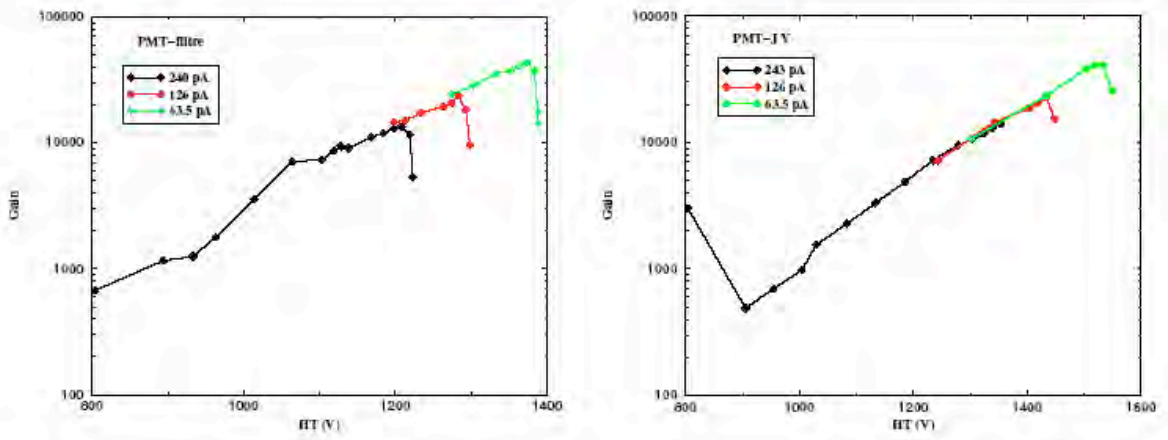


Fig. C.10 Logarithmic representation of the variation of the gain with the high voltage. Left: the measurements made for the PMT-filter. Right: those made for the PMT-JY.

By plotting the gain variation versus the high voltage on a logarithmic scale, and not linear anymore, our results can be compared with the typical curves provided by Photonis. Figures C.10 and C.11 show these variations for each of our PMT, as well as the curve provided by Photonis. Voltage dividers used here are of the C type. The variation is well reproduced by our measurements. This is another proof of the validity of our methods.

The conditions of illumination are more varied for this measurement than for the cartography. One can thus give the values of the PMT absolute efficiency over the surface of the lighted photocathode only for the high voltage used for cartography (see figure C.12).

### C.3 Conclusion

For a given PMT, the efficiency on the photocathode surface is not at all the same at high and low gain: one can compare the maps obtained in this annex and in chapter 6.2.

For each measurement made at low gain, one can compute the efficiency variation of the in over the useful detection surface. The figure C.12 show these curves for high and low gain for both PMT. The low gain measurement used to plot the PMT-filter curve is done at a voltage of 1373 V and an absolute efficiency (measured in the pixel (0, 3)) of 22.58%. That of the PMT-JY, done at a voltage of 1503 V, gives an efficiency of 21.49%.

One can see on figure C.12 that the photocathode efficiency is much more uniform at high gain than at low gain. However, for a given gain, the efficiency variation, i.e. the curve slope, is almost identical from one PMT to another (one must naturally limit oneself to a maximum surface of approximately 1000 mm<sup>2</sup>, for the PMT-filter filter does not cover the full photocathode surface).

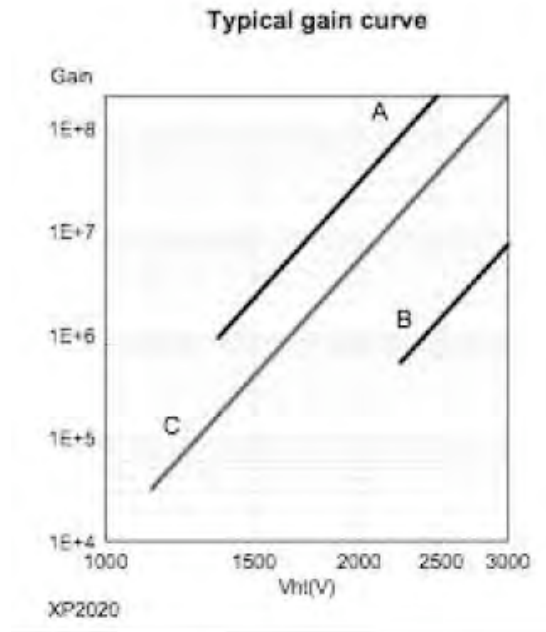


Fig. C.11 Reference curves for the variation of the gain with the voltage. The voltage divider used in the experiment is of type C [Pho02]

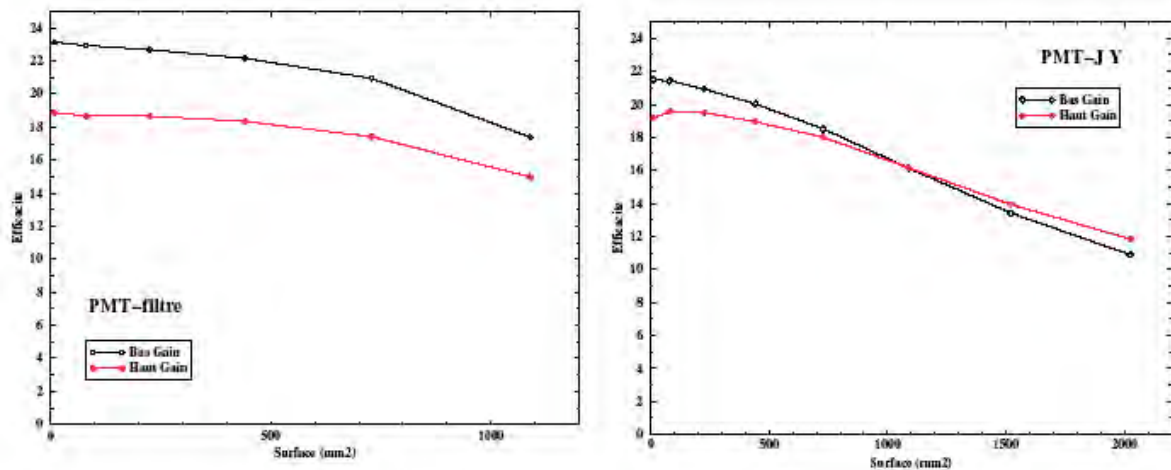


Fig. C.12 Variation of the PMT-filter efficiency (right) and of the PMT-JY (left), versus the effective detecting surface.

Whatever the gain, this method of absolute calibration is valid and precise (5% for the calibration at low gain). The use of integrating spheres allows a precise and stable adjustment the quantity of light to be divided between several exits. If, at high gain, the measurement of single photoelectrons is made by counting, thus of an extremely precise way, here at low gain, it is based on the laws of the statistics. Maybe the law is not really purely Gaussian. The precision is thus worse. The measurements made at low gain show the limits of the PMT XP2020Q, because their structure is designed for a high gain use: the non-linear modes are very quickly reached.

## Annex D

### Photographs of the assemblies

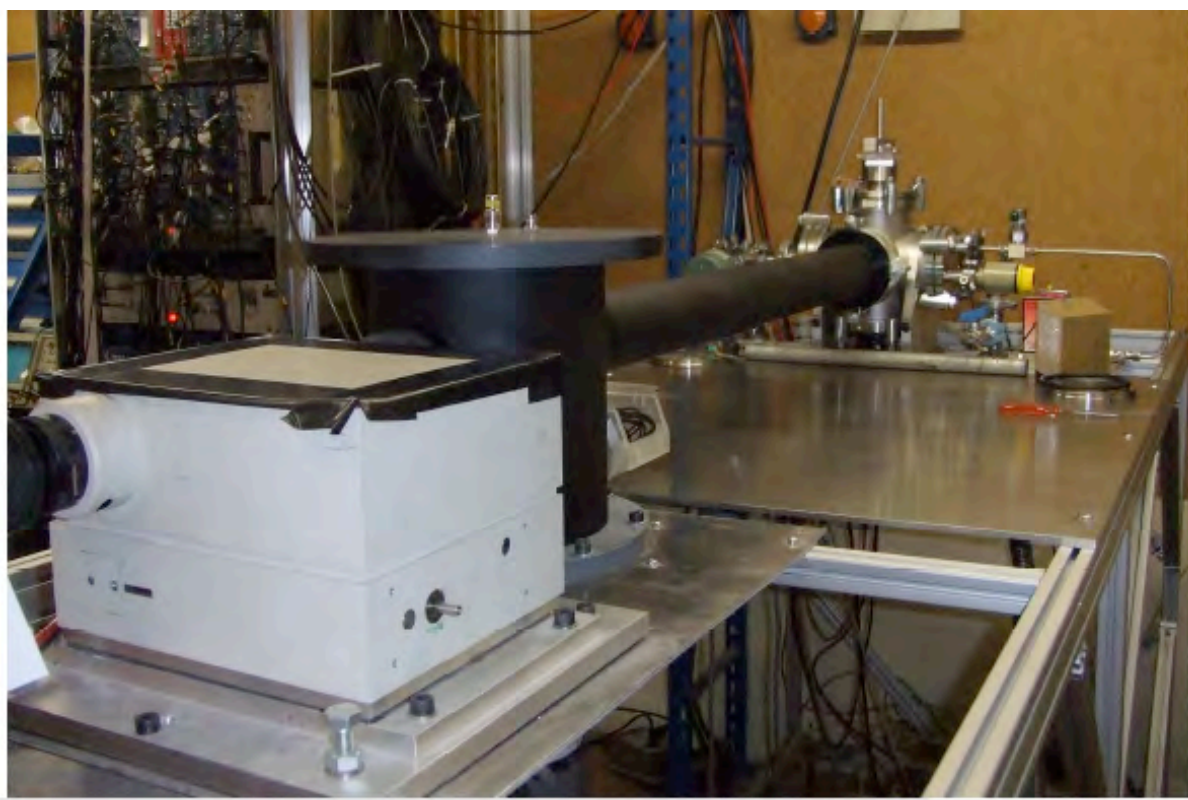


Fig. D.1 Bench to measure fluorescence. The spectrometer is in the foreground and the stainless steel cross at the other end of the assembly. Inside of the cross where the gas circulates are the source, the lead shielding and the scintillator.



Fig. D.2 Fluorescence vessel. In the foreground, one distinguishes the arrival gas line. The yellow valve allows either to connect the cross to a pump and of make vacuum, or to make an air intake. Against the wall is the PMT-filter.



Fig. D.3 Optical assembly: the lens is in the foreground, and the spectrometer with the back. Naturally, the lens and the optical rays are in the black during measurements. The spectrometer entry slit is opened to 2 mm. One can distinguish the PMT-JY (covered with a sheet of paper on this photo) at the spectrometer exit in the back.

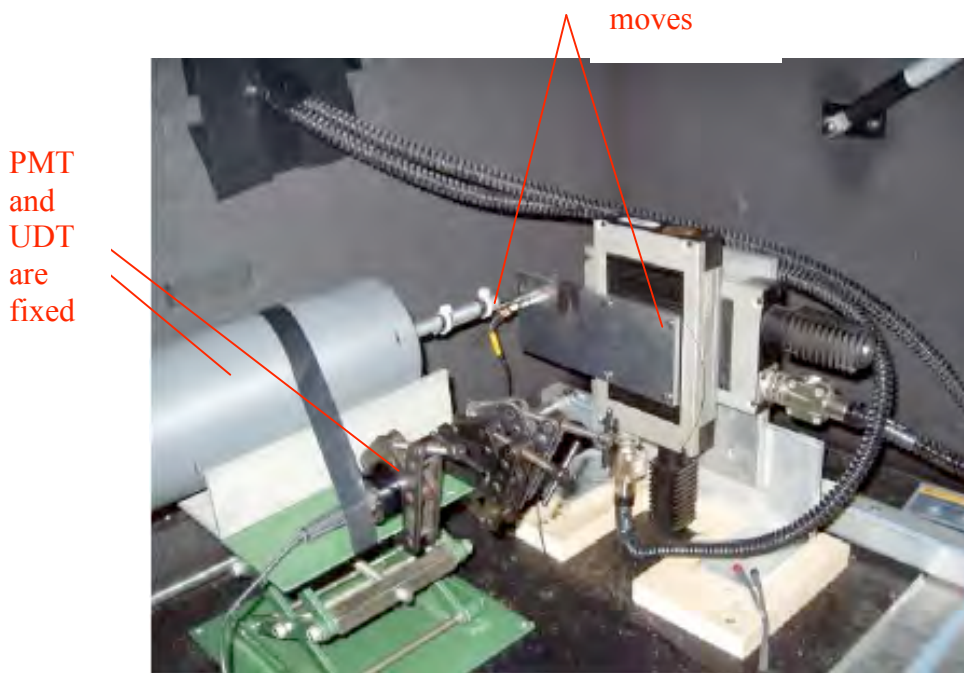


Fig. D.4 Interior of the black box. The optical fiber directed towards the PMT photocathode is fixed to the XY movement, and placed in a light attenuator. The other is fixed in front of a calibrated UDT photodiode (on the right of the PMT).



Fig. D.5 Absolute PMT calibration. The light source of (matrix of 19 LED at 400 nm) is fixed above the first sphere (in the back). One of the exits of this sphere sends a luminous flux on a calibrated UDT photodiode (in black). Between the two spheres, a diaphragm limits the emission at the second exit, so that a little amount of light arrives in the second sphere and then, to the PMT.

# Figures list

1.1 Spectrum of the cosmic rays	9
1.2 Schematic presentation of the Auger experiments and EUSO	11
1.3 Development of an atmospheric shower	12
1.4 Light yield of an atmospheric shower	14
2.1 Diagram of the energy levels of molecular nitrogen	20
2.2 Spectrum of fluorescence	20
2.3 Variation of the fluorescence yield in nitrogen at high energy in (AIRFLY).	25
2.4 Results of measurements of fluorescence yield in air in versus electron energy loss	26
2.5 Variation of the pressure, temperature and density with altitude (US Standard)	27
2.6 Variation of the production rate of fluorescence versus altitude (different models)	28
4.1 Complete diagram of the bench	35
4.2 Spectra of strontium and yttrium	36
4.3 Example of TDC spectrum	37
4.4 Behavior of collimated beam with pressure	38
4.5 Behavior of non collimated beam	39
4.6 Interior of the cross	41
4.7 Curves of transmission of current photomultipliers windows	42
4.8 Curve of transmission of BG3 filter	43
4.9 Diagrammatic representation of the bench optics.	43
4.10 Detection of photons of fluorescence emitted far from the optical axis	45
4.11 Production of secondary electrons by the source electrons	47
4.12 Maximum deviation of an electron after having produced a $\delta$	48
4.13 Energy loss spectrum of diffused electrons	49
4.14 Simulation of the electrons energy spectra arriving at the scintillator	50
4.15 Energy spectra in of the detected electrons after diffusion in the lead shielding.	51
4.16 Gas system	53
4.17 Simplified diagram of the data acquisition electronics	53
4.18 Single photoelectron spectra (PMT-filter PMT-JY) and cut by the discriminators	55
5.1 Calibration of the internal pressure	56
5.2 Horizontal and vertical alignments of the lens	57
5.3 LED and spectrometer widths	58
5.4 Spectrometer calibration set-up	60
5.5 Determination of the luminous flux ratio in the calibration set-up	60
5.6 Laser response of the spectrometer for 3 different slit widths	61
5.7 Absolute spectrometer efficiency	62
6.1 Diagram of a photomultiplier tube	64
6.2 Set-up to make a controlled source to calibrate a PMT	69
6.3 Cartography of the PMT in the black box	73

6.4 LED spectrum at 377 nm	74
6.5 Absolute efficiency curves of the UDT S370 photodiode	75
6.6 Response of PMT-filter at low gain.	76
6.7 Response of PMT-JY at low gain.	77
6.8 Single photoelectron acquisition for PMT cartography	77
6.9 Local increase in the photocathode efficiency	78
6.10 Map of PMT-filter at high gain	79
6.11 3D map of the response of the PMT-filter at high gain	79
6.12 Map of PMT-JY at high gain	80
6.13 3D map of the response of the PMT-JY at high gain	80
6.14 Measurement of the luminous flux ratio between the detectors with two spheres.	85
6.15 Absolute efficiency curves of the Ophir photodiodes	85
6.16 LED matrix	86
6.17 LED ETG-3UV400-30 spectrum around 400 nm	86
6.18 Measurement of the PMT efficiency at high gain	88
6.19 Absolute efficiency of PMT-filter detecting the fluorescence spectrum	91
6.20 Absolute efficiency of the PMT-JY versus wavelength	92
6.21 Total absolute efficiency of the PMTs versus the detecting surface	93
7.1 TDC spectrum of the PMT-filter at low energy	96
7.2 Variations of integral measurements at 1.1 MeV and 1.5 MeV.	99
7.3 Energy loss of an electron in air and average energy of each measurement.	100
7.4 Comparison of the fluorescence yields measurements	102
7.5 Comparison of measurements and models of fluorescence yields	103
7.6 Spectral width of the spectrometer	104
7.7 Absolute spectrometer efficiency	105
7.8 Spectrum of measured fluorescence at atmospheric pressure. Ulrich spectrum	106
7.9 The spectra of fluorescence measured by Ulrich (convoluted) and in this work	108
A.1 Complete diagram of the data acquisition	115
A.2 Dead time due to the two electron discriminators measurements	118
A.3 LabVIEW interface: start of a measurement.	119
A.4 LabVIEW interface: spectra acquisition	120
A.5 LabVIEW program: reading and recording spectra	121
A.6 Flow-chart of the course of a measurement	122
B.1 Detection of individual photons by a photomultiplier	124
B.2 Electronic set-up for a PMT in single photoelectron mode	125
B.3 Single photoelectron spectra superimposed with the cut due to the discriminators	126
C.1 Map of the PMT-filter at low gain	129
C.2 3D map of the PMT-filter at low gain	129
C.3 Map of the PMT-JY at low gain	130
C.4 3D map of the PMT-JY at low gain	130
C.5 Determination of the luminous flux ratio at low gain.	131
C.6 Assembly for the efficiency measurement of the at low gain.	132
C.7 Examples of PMT spectra recorded during measurements with low gain	133

C.8 Results of the low gain measurements	136
C.9 Variation of the PMTs efficiency versus high voltage	137
C.10 Logarithmic representation of the variation of the gain with the high voltage.	138
C.11 Reference curves of the variation of the gain with the high voltage	139
C.12 Absolute efficiency at high and low gain versus the detection effective surface	139
D.1 Bench to measure fluorescence	140
D.2 Fluorescence vessel	141
D.3 Optical assembly	141
D.4 Cartography of a PMT in the black box	142
D.5 Absolute PMT calibration with two spheres and a calibrated photodiode	142

## Tables list

2.1 Summary of the results of [NaganoWatson00], in air, at 1013 hPa and 20° C.	26
2.2 Pressure, temperature and density at sea level in the 1976US standard model.	29
4.1 Summary of the discriminator thresholds of each, and average energies	50
4.2 Composition of the reconstituted dry air used in the measurements	52
4.3 Gain and applied voltages	54
4.4 Proportion of single photoelectrons lost because of the discriminators	55
5.1 Spectrometer efficiencies	59
6.1 Characteristics of the PMT “photons”	65
6.2 Surfaces used to compute flux ratios	83
6.3 Currents measured by each photodiode	87
6.4 Results of measurements of absolute efficiencies	90
6.5 Absolute efficiencies of the two PMT at high gain	92
6.6 Errors on the efficiency calculation	93
7.1 Numerical values used in the analysis of the PMT-filter spectra	98
7.2 Systematic uncertainties of the integrated measurement.	98
7.3 Fluorescence yields, pressure and temperature of each measurement.	99
7.4 Electron energy loss Recall in air used for to normalize the results	99
7.5 Calculated theoretical yields of fluorescence	101
7.6 Numerical values used in the analysis of PMT-JY spectra	105
A.1 Counting rates measured in air at atmospheric pressure	117
C.1 Currents measured by each photodiode for to determine the flux ratio	131
C.2 Numbers of photons versus photodiode currents	135

# Bibliographical references

## Physics of the cosmic rays

- [aug] [www.auger.org](http://www.auger.org).
- [BahcallWaxman03] J.N. Bahcall and E. Waxman. *Phys. Lett. B*, 556 :1 6, 2003.
- [BoratavSigl04] M. Boratav and G. Sigl. *Compte-rendus de l'académie des sciences*, 2004. 5.
- [Crawford] H. Crawford. private communication in EUSO.
- [eus] [www.euso-mission.org](http://www.euso-mission.org).
- [Gaisser90] T.K. Gaisser. *Cosmic rays and particle physics*. Cambridge, 1990.
- [Gorodetzky04] P. Gorodetzky. In ISVHECRI, 2004.
- [Greisen64] K. Greisen. *Phys. Rev. Lett.*, 16 :748, 1964.
- [Leprince-Ringuet45] L. Leprince-Ringuet. *Les rayons cosmiques*. Albin-Michel 1945.
- [NaganoWatson00] M. Nagano and A. Watson. *Rev. Mod. Phys.*, 72(3) :689 732 2000.
- [Nerling05] F. Nerling. *Description of Cherenkov light production in extensive air shower*. PhD thesis, Université de Karlsruhe, 2005.
- [Playez04] N. Playez. *Détection hybride des rayons cosmiques d'ultra-hautes énergies avec l'observatoire Pierre Auger*. PhD thesis, Université Joseph Fourier, Grenoble I, 2004.
- [Sokolsky04] P. Sokolsky. *Introduction to ultra-high energy cosmic ray physics (updated)*. Frontiers in physics, 2004.
- [Sommers04] P. Sommers. In *Compte-rendus de l'Académie des Sciences*, volume 5 of IV, 2004.
- [Watson05] A. Watson. In *TAUP2005*, 2005.
- [Yoshida04] S. Yoshida. In *Compte-rendus de l'Académie des Sciences*, volume 5 of IV, 2004.
- [ZatsepinKuzmin66] G.T. Zatsepin and V.A. Kuzmin. *JETP Lett. (Engl. Transl.)*, 4 :78, 1966.

## Physics of the fluorescence

- [air] <http://www.auger.de/events/air-light-03/>.
- [Arciprete+05] F. Arciprete et al. 17055-cze-bohacova-m-abs1-he14-poster. In *ICRC 2005*, 2005.
- [Belz+06] J.W. Belz et al. *Astropart. Phys.*, 25 :129 139, 2006.
- [Bunner64] A. Bunner. *The atmosphere as a cosmic ray scintillator*. Master's thesis, Cornell university, 1964.
- [Bunner67] A. Bunner. *Cosmic ray detection by atmospheric fluorescence*. PhD thesis, Cornell university, 1967.
- [Colin05] P. Colin. *Reconstruction des gerbes atmosphériques et mesure de la fluorescence de l'air pour l'étude des rayons cosmiques ultra énergétiques au sein du projet EUSO*. PhD thesis, Université Joseph Fourier, Grenoble, 2005.
- [DavidsonO'Neil64] G. Davidson and R. O'Neil. *J. Chem. Phys.*, 41(12) :3946 3955, 1964.
- [Hansen+83] H.H. Hansen et al. *Int.J.Appl.Radiat.Isot.*, 34 :1241 1247, 1983.
- [Herzberg50] G. Herzberg. *Molecular spectra and molecular structure I. Spectra of diatomic molecules*. D. van Nostrand Company Inc., New York, 1950.
- [icr] <http://icrc2005.tifr.res.in/>.
- [iwf] <http://lappweb.in2p3.fr/iwfm05/index.html>.
- [Kakimoto+96] F. Kakimoto et al. *NIM A*, 372 :527 533, 1996.
- [Keilhauer04] B. Keilhauer. *Investigation of atmospheric effects on the development of extensive air showers and their detection with the Pierre Auger Observatory*. PhD thesis, Karlsruhe University, 2004.
- [Keilhauer+05] B. Keilhauer et al. *Astropart. Phys.*, 25 :259 268, 2005.
- [Millet70] P. Millet. *Mécanismes de la post-luminescence de l'azote irradié par des particules alpha*. PhD thesis, Université de Toulouse, 1970.
- [Nagano+03] M. Nagano et al. *Astropart. Phys.*, 20 :293 309, 2003.
- [Nagano+04] M. Nagano et al. *astro-ph/0406474*, 2004.

## Set-up operations

- [Besson+94] P. Besson et al. *NIM A*, 344 :435 437, 1994.
- [Biller+99] S.D. Biller et al. *NIM A*, 432 :364 373, 1999.
- [BirenbaumScarl73] L. Birenbaum and D.B. Scarl. *Appl. Opt.*, 12(3) :519 521, 1973.
- [BlumRolandi94] W. Blum and L. Rolandi. *Particle detection with drift chambers*. Springer-Verlag, 1994.
- [Dolbeau] J. Dolbeau. private communication.
- [Dorenbos+93] P. Dorenbos et al. *NIM A*, 325 :367 369, 1993.
- [est] <http://physics.nist.gov/physrefdata/star/text/contents.html>.
- [Foord+69] R. Foord et al. *Appl. Opt.*, 8(10) :1975 1989, 1969.
- [Hocrelle] D. Hocrelle. Jobin-Yvon. private communication.
- [Lab] Labsphere. *A Guide to integrating sphere - Theory and applications*.
- [LakesPoultney71] R.S. Lakes and S.K. Poultney. *Appl. Opt.*, 10(4) :797 800, 1971.
- [Laser2000] Laser2000. private communication.
- [Lavoute] P. Lavoute. private communication.
- [Lefièvre] B. Lefièvre. private communication.
- [Pho99] Hamamatsu Photonics. *Photomultiplier tubes - Basics and applications (2d edition)*, 1999.
- [Pho02] Photonis. *Photomultiplier tubes, principles and applications*, 2002.
- [Siegbahn] K. Siegbahn. *Alpha-Beta-and Gamma Ray Spectroscopy*, volume 1. North Holland publishing.
- [Tub] Electron Tubes. *Absolute calibration of photomultiplier based detectors, difficulties and uncertainties*. Technical reprint R/P091.
- [uss] <http://www.pdas.com/atmos.htm>.